



# **NAVAL POSTGRADUATE SCHOOL**

**MONTEREY, CALIFORNIA**

## **THESIS**

**PASSIVE COHERENT DETECTION AND TARGET  
LOCATION WITH MULTIPLE NON-COOPERATIVE  
TRANSMITTERS**

by

Qinling Jeanette Olivia Tan

June 2015

Thesis Advisor:  
Co-Advisor:

David C. Jenn  
Edward Fisher

**Approved for public release; distribution is unlimited**

THIS PAGE INTENTIONALLY LEFT BLANK

<b>REPORT DOCUMENTATION PAGE</b>			Form Approved OMB No. 0704-0188	
Public reporting burden for this collection of information is estimated to average 1 hour per response, including the time for reviewing instruction, searching existing data sources, gathering and maintaining the data needed, and completing and reviewing the collection of information. Send comments regarding this burden estimate or any other aspect of this collection of information, including suggestions for reducing this burden, to Washington headquarters Services, Directorate for Information Operations and Reports, 1215 Jefferson Davis Highway, Suite 1204, Arlington, VA 22202-4302, and to the Office of Management and Budget, Paperwork Reduction Project (0704-0188) Washington, DC 20503.				
<b>1. AGENCY USE ONLY (Leave blank)</b>		<b>2. REPORT DATE</b> June 2015	<b>3. REPORT TYPE AND DATES COVERED</b> Master's Thesis	
<b>4. TITLE AND SUBTITLE</b> PASSIVE COHERENT DETECTION AND TARGET LOCATION WITH MULTIPLE NON-COOPERATIVE TRANSMITTERS			<b>5. FUNDING NUMBERS</b>	
<b>6. AUTHOR(S)</b> Qinling Jeanette Olivia Tan				
<b>7. PERFORMING ORGANIZATION NAME(S) AND ADDRESS(ES)</b> Naval Postgraduate School Monterey, CA 93943-5000			<b>8. PERFORMING ORGANIZATION REPORT NUMBER</b>	
<b>9. SPONSORING /MONITORING AGENCY NAME(S) AND ADDRESS(ES)</b> N/A			<b>10. SPONSORING/MONITORING AGENCY REPORT NUMBER</b>	
<b>11. SUPPLEMENTARY NOTES</b> The views expressed in this thesis are those of the author and do not reflect the official policy or position of the Department of Defense or the U.S. Government. IRB Protocol number ____N/A____.				
<b>12a. DISTRIBUTION / AVAILABILITY STATEMENT</b> Approved for public release; distribution is unlimited			<b>12b. DISTRIBUTION CODE</b>	
<b>13. ABSTRACT (maximum 200 words)</b>  Passive bistatic radars (PBR) and passive multistatic radars (PMR) use opportunistic transmitters to detect and locate targets. In this thesis, a maritime scenario was modeled with merchant vessels serving as multiple non-cooperative opportunistic transmitters while a frigate warship equipped with Electronic Warfare (EW) and Direction Finding (DF) receivers takes on the role of the receiver in a PBR/PMR configuration. The targets are assumed to be the generic Formidable-class frigate. A MATLAB model is developed to simulate the operating environment and passive detection and location process. Detection coverage is investigated to propose optimal PBR/PMR configurations and geometry, while elliptical and hyperbolic target location methods are explored to quantify the effects of PBR/PMR parameters and geometry on target estimated location uncertainty.				
<b>14. SUBJECT TERMS</b> bistatic, multistatic, target detection, target location, passive coherent detection, non-cooperative transmitters, opportunistic transmitters, hitchhiker radar, forward-scattering, back-scattering, error ellipse, uncertainty ellipse			<b>15. NUMBER OF PAGES</b> 169	
			<b>16. PRICE CODE</b>	
<b>17. SECURITY CLASSIFICATION OF REPORT</b> Unclassified	<b>18. SECURITY CLASSIFICATION OF THIS PAGE</b> Unclassified	<b>19. SECURITY CLASSIFICATION OF ABSTRACT</b> Unclassified	<b>20. LIMITATION OF ABSTRACT</b> UU	

THIS PAGE INTENTIONALLY LEFT BLANK

**Approved for public release; distribution is unlimited**

**PASSIVE COHERENT DETECTION AND TARGET LOCATION WITH  
MULTIPLE NON-COOPERATIVE TRANSMITTERS**

Qinling Jeanette Olivia Tan  
Civilian, DSO National Laboratories, Singapore  
B.Eng, National University of Singapore, 2010

Submitted in partial fulfillment of the  
requirements for the degree of

**MASTER OF SCIENCE IN INFORMATION WARFARE SYSTEMS  
ENGINEERING**

from the

**NAVAL POSTGRADUATE SCHOOL  
June 2015**

Author: Qinling Jeanette Olivia Tan

Approved by: David C. Jenn  
Thesis Advisor

Edward Fisher  
Co-Advisor

Dan Boger  
Chair, Department of Information Sciences Department

THIS PAGE INTENTIONALLY LEFT BLANK

## **ABSTRACT**

Passive bistatic radar (PBR) and passive multistatic radar (PMR) use opportunistic transmitters to detect and locate targets. In this thesis, a maritime scenario was modeled with merchant vessels serving as multiple non-cooperative opportunistic transmitters, while a frigate warship equipped with Electronic Warfare (EW) and Direction Finding (DF) receivers takes on the role of the receiver in a PBR/PMR configuration. The targets are assumed to be the generic Formidable-class frigate.

A MATLAB model is developed to simulate the operating environment and passive detection and location process. Detection coverage is investigated to propose optimal PBR/PMR configurations and geometry, while elliptical and hyperbolic target location methods are explored to quantify the effects of PBR/PMR parameters and geometry on target estimated location uncertainty.

THIS PAGE INTENTIONALLY LEFT BLANK



# TABLE OF CONTENTS

<b>I.</b>	<b>INTRODUCTION.....</b>	<b>1</b>
<b>A.</b>	<b>OVERVIEW .....</b>	<b>1</b>
<b>B.</b>	<b>HISTORY .....</b>	<b>3</b>
1.	First Resurgence.....	3
2.	Second Resurgence.....	4
3.	Third Resurgence.....	4
<b>C.</b>	<b>RECENT DEVELOPMENTS IN BISTATIC AND MULTISTATIC RADAR .....</b>	<b>6</b>
<b>D.</b>	<b>THESIS OBJECTIVE .....</b>	<b>8</b>
<b>E.</b>	<b>THESIS CHAPTER OUTLINE .....</b>	<b>10</b>
<b>II.</b>	<b>BISTATIC RADAR THEORY.....</b>	<b>11</b>
<b>A.</b>	<b>DEFINITION .....</b>	<b>11</b>
<b>B.</b>	<b>RANGE EQUATION .....</b>	<b>11</b>
<b>C.</b>	<b>TARGET LOCATION EQUATIONS.....</b>	<b>16</b>
1.	Bistatic Radar Trigonometry.....	16
2.	Least-Squares Intersection of Lines.....	19
3.	Hyperbolic Target Location.....	22
<b>D.</b>	<b>MEASUREMENT AND LOCATION ERRORS .....</b>	<b>25</b>
1.	Time Delay (Range) Measurements .....	26
2.	Angle Measurements .....	26
3.	Transmitter and Receiver Position Accuracy .....	27
4.	Receiver-to-Target Range Error .....	27
<b>E.</b>	<b>ERROR ELLIPSE PARAMETERS .....</b>	<b>28</b>
<b>III.</b>	<b>MATLAB AND FEKO MODELING .....</b>	<b>33</b>
<b>A.</b>	<b>PROBLEM SETUP .....</b>	<b>33</b>
<b>B.</b>	<b>FEKO MODEL .....</b>	<b>34</b>
<b>C.</b>	<b>MATLAB MODEL.....</b>	<b>37</b>
1.	Detection Coverage Model 1 .....	38
2.	Detection Coverage Model 2 .....	39
3.	Simulation Duration and Accuracy Trade-off .....	41
4.	Target Location Model .....	44
<b>D.</b>	<b>MODEL VERIFICATION .....</b>	<b>44</b>
<b>IV.</b>	<b>SIMULATION RESULTS.....</b>	<b>49</b>
<b>A.</b>	<b>DETECTION COVERAGE .....</b>	<b>49</b>
1.	Bistatic RCS.....	49
2.	General Observations .....	50
3.	Vary Number of Transmitters .....	52
4.	Vary Transmitter Range .....	54
5.	Vary Transmitter-Target-Receiver Geometry .....	56
6.	Target Path Detection.....	60
<b>B.</b>	<b>TARGET LOCATION ESTIMATION.....</b>	<b>62</b>

1.	General Observations .....	62
2.	Error Ellipse of Target Position Estimate .....	64
V.	CONCLUSION .....	73
A.	SUMMARY OF FINDINGS .....	73
1.	Findings for Detection Coverage .....	73
2.	Findings for Target Location .....	74
B.	FUTURE WORK .....	75
	APPENDIX A. DERIVATION OF ERROR ELLIPSE PARAMETERS FROM BIVARIATE NORMAL DISTRIBUTION .....	77
	APPENDIX B. SPECIFICATION SHEET FOR MANTADIGITAL RADAR BY KELVIN HUGHES.....	87
	APPENDIX C. SPECIFICATION SHEET FOR TELEDYNE DEFENCE QR026 EW RECEIVER.....	89
	APPENDIX D. SPECIFICATION SHEET FOR POYNTING DEFENCE DF-A0062 DF RECEIVER.....	91
	APPENDIX E. DETECTION COVERAGE PLOTS FOR TARGET PLANE IN S- BAND .....	93
	APPENDIX F. DETECTION COVERAGE RESULTS .....	99
	F.1 VARY NUMBER OF TRANSMITTERS .....	99
	F.2 VARY TRANSMITTER RANGE .....	109
	F.3 VARY TRANSMITTER-TARGET-RECEIVER GEOMETRY .....	113
	F.4 RANDOMLY DISTRIBUTED TRANSMITTERS .....	117
	APPENDIX G. TARGET PATH DETECTION RESULTS.....	123
	APPENDIX H. TARGET LOCATION RESULTS.....	127
	LIST OF REFERENCES.....	141
	INITIAL DISTRIBUTION LIST .....	145

## LIST OF FIGURES

Figure 1.	Bistatic radar geometry.....	3
Figure 2.	Pictorial representation of the PBR setup. After [4]. .....	9
Figure 3.	Cassini oval for $c < b$ where $b = r_1 r_2$ .....	13
Figure 4.	Bistatic radar geometry for converting North-referenced coordinates into polar coordinates. After [2]. .....	13
Figure 5.	Ovals of Cassini, contours of constant SNR (dB), with $K = 30L^4$ . After [2]. .....	14
Figure 6.	Timing sequence diagram for direct and indirect method for calculating range sum $(R_T + R_R)$ . From [2]. .....	17
Figure 7.	Reception of direct and reflected pulses. ....	18
Figure 8.	Least-squares intersection of lines solution to three PBR case.....	20
Figure 9.	Perpendicular distance from a point to a line. From [32]. ....	21
Figure 10.	Single PBR in multi-bistatic radar scenario.....	23
Figure 11.	Error ellipse parameters. ....	28
Figure 12.	Chi-square probability density function with 2 degrees of freedom. The area to the right of $\chi^2$ critical value is $\alpha$ . ....	30
Figure 13.	Error ellipse rotation to achieve statistical independence. From [38]. ....	31
Figure 14.	Frigate FEKO model (top) and actual RSN Formidable-class frigate (bottom; from [39]). Side-profile.....	35
Figure 15.	Frigate FEKO model and coordinate system.....	36
Figure 16.	Frigate's monostatic RCS (dBsm) (left) and bistatic RCS (dBsm) with incident angle of $10^\circ$ (right) at 3.05 GHz. ....	36
Figure 17.	Frigate bistatic RCS (dBsm) with incident angle of $10^\circ$ at 3.05 GHz. RCS at $1^\circ$ resolution (left) and $0.1^\circ$ resolution (right). ....	37
Figure 18.	MATLAB Detection Coverage Model 1 flowchart. ....	39
Figure 19.	MATLAB Detection Coverage Model 2 flowchart.....	40
Figure 20.	Detection coverage of a $40 \text{ km} \times 40 \text{ km}$ area of interest grid points at 1 km resolution.....	42
Figure 21.	Simulation duration and accuracy trade space for detection coverage models. ....	43
Figure 22.	Detection coverage contours for constant RCS target. ....	45
Figure 23.	Target plate FEKO model.....	46
Figure 24.	Target plate S-Band azimuth RCS (dBsm) at $\phi=90^\circ$ incidence. ....	46
Figure 25.	Target bistatic RCS (dBsm) with incident angle $10^\circ$ at 3.0 GHz (left) and 9.41 GHz. ....	50
Figure 26.	Target positions in forward-scattering and back-scattering configuration on detection coverage plot. ....	51
Figure 27.	Detection gaps and bearings extending from Tx-Rx baseline in detection coverage plot.....	52
Figure 28.	Detection coverage plots at S-Band for with target plate at $0^\circ$ orientation as the number of transmitters varies. ....	53

Figure 29.	Detection coverage plots at S-Band with target plate at $0^\circ$ orientation as the transmitter range to receiver increases. ....	55
Figure 30.	Detection coverage at S-Band for 4 Tx in receiver-centered geometry and target plate at $30^\circ$ orientation. ....	57
Figure 31.	Detection coverage at S-Band for 4 Tx in transmitter-clustered geometry and target plate at $30^\circ$ orientation. ....	57
Figure 32.	Detection coverage at S-Band for 20 Tx randomly positioned around Rx at 5–30 km range and target plate at $0^\circ$ orientation. ....	58
Figure 33.	Detection coverage at S-Band for 20 Tx randomly positioned around Rx at 5–30 km range and target plate at $-90^\circ$ orientation. ....	59
Figure 34.	Detection coverage at S-Band for 20 Tx randomly positioned around Rx at 5–30 km range and target plate at $45^\circ$ orientation. ....	60
Figure 35.	Five target paths used to generate target path detection performance results. ....	61
Figure 36.	Detection coverage along target's path at S-Band for 4 Tx (left) and 20 Tx (right). RCS extracted from pre-computed RCS table. ....	61
Figure 37.	Dilution of precision comparison between elliptical and hyperbolic methods using SNR-independent measurement errors. ....	63
Figure 38.	Target location errors using hyperbolic method (S-Band) with SNR-dependent measurement errors. ....	64
Figure 39.	Target position estimate scatter plot from elliptical method for target in Tx-Rx cluster. ....	65
Figure 40.	Target position estimate scatter plot from hyperbolic method for target in Tx-Rx cluster. ....	66
Figure 41.	Target position estimate scatter plot from elliptical method for target outside Tx-Rx cluster. ....	66
Figure 42.	Target position estimate scatter plot from hyperbolic method for target outside Tx-Rx cluster. ....	67
Figure 43.	Uncertainty area associated with position estimates from elliptical method for target in Tx-Rx cluster. ....	68
Figure 44.	Uncertainty area associated with position estimates from elliptical method for target outside Tx-Rx cluster. ....	68
Figure 45.	Elliptical iso-contours of constant time delay measurements with transmitter and receiver at ellipse foci. ....	69
Figure 46.	Uncertainty area associated with position estimates from hyperbolic method for target in Tx-Rx cluster. ....	70
Figure 47.	Uncertainty area associated with position estimates from hyperbolic method for target outside Tx-Rx cluster. ....	70
Figure 48.	Hyperbolic target location estimate's error ellipse at 50%, 70%, 90%, and 99% confidence levels. ....	72
Figure 49.	Joint Gaussian pdf surface and contours for various $\sigma_x$ , $\sigma_y$ , and $\rho_{xy}$ values. After [38]. ....	79
Figure 50.	Eigenvectors ( $\lambda_1, \lambda_2$ ) of a covariance matrix on an error ellipse. ....	80
Figure 51.	Chi-square pdf for $p$ degrees of freedom. ....	82

Figure 52.	Chi-square pdf where the area to the right of the critical value is $\alpha$ .....	83
Figure 53.	Rotation of error ellipse principle axis. From [38]. .....	84
Figure 54.	Technical Specifications for MantaDigital Radar by Kelvin Hughes. From [43]. .....	88
Figure 55.	Technical Specifications for Teledyne Defence QR026 EW Receiver. From [44]. .....	90
Figure 56.	Technical Specifications for Poynting Defence DF A0062 DF Receiver. From [45]. .....	91
Figure 57.	Detection coverage (left) for Tx at [-5000, 0] and target plate at 0° orientation with corresponding S-band bistatic RCS (right).....	93
Figure 58.	Detection coverage (left) for Tx at [-5000, 0] and target plate at 0° orientation with corresponding S-band bistatic RCS (right).....	94
Figure 59.	Detection coverage (left) for Tx at [-5000, 0] and target plate at 90° orientation with corresponding S-band bistatic RCS (right).....	94
Figure 60.	Detection coverage (left) for Tx at [-5000, 0] and target plate at -90° orientation with corresponding S-band bistatic RCS (right).....	95
Figure 61.	Detection coverage (left) for Tx at [-5000, 0] and target plate at 45° orientation with corresponding S-band bistatic RCS (right).....	95
Figure 62.	Detection coverage (left) for Tx at [0, 5000] and target plate at 45° orientation with corresponding S-band bistatic RCS (right).....	96
Figure 63.	Detection coverage (left) for Tx at [-5000,0] and target plate at -45° orientation with corresponding S-band bistatic RCS (right).....	96
Figure 64.	Detection coverage (left) for Tx at [0, 5000] and target plane at -45° orientation with corresponding S-band bistatic RCS (right).....	97
Figure 65.	Detection coverage at S-Band for 1 Tx at 5 km range and target at 0° orientation. ....	99
Figure 66.	Detection coverage at S-Band for 1 Tx at 5 km range and target at -90° orientation. ....	99
Figure 67.	Detection coverage at X-Band for 1 Tx at 5 km range and target at 0° orientation. ....	100
Figure 68.	Detection coverage at X-Band for 1 Tx at 5 km range and target at -90° orientation. ....	100
Figure 69.	Detection coverage at S-Band for 2 Tx at 5 km range and target at 0° orientation. ....	101
Figure 70.	Detection coverage at S-Band for 2 Tx at 5 km range and target at -90° orientation. ....	101
Figure 71.	Detection coverage at X-Band for 2 Tx at 5 km range and target at 0° orientation. ....	102
Figure 72.	Detection coverage at X-Band for 2 Tx at 5 km range and target at -90° orientation. ....	102
Figure 73.	Detection coverage at S-Band for 3 Tx at 5 km range and target at 0° orientation. ....	103
Figure 74.	Detection coverage at S-Band for 3 Tx at 5 km range and target at -90° orientation. ....	103

Figure 75.	Detection coverage at X-Band for 3 Tx at 5 km range and target at $0^\circ$ orientation. ....	104
Figure 76.	Detection coverage at X-Band for 3 Tx at 5 km range and target at $-90^\circ$ orientation. ....	104
Figure 77.	Detection coverage at S-Band for 4 Tx at 5 km range and target at $0^\circ$ orientation. ....	105
Figure 78.	Detection coverage at S-Band for 4 Tx at 5 km range and target at $-90^\circ$ orientation. ....	105
Figure 79.	Detection coverage at X-Band for 4 Tx at 5 km range and target at $0^\circ$ orientation. ....	106
Figure 80.	Detection coverage at X-Band for 4 Tx at 5 km range and target at $-90^\circ$ orientation. ....	106
Figure 81.	Detection coverage at S-Band for 8 Tx at 5 km range and target at $0^\circ$ orientation. ....	107
Figure 82.	Detection coverage at S-Band for 8 Tx at 5 km range and target at $-90^\circ$ orientation. ....	107
Figure 83.	Detection coverage at X-Band for 8 Tx at 5 km range and target at $0^\circ$ orientation. ....	108
Figure 84.	Detection coverage at X-Band for 8 Tx at 5 km range and target at $-90^\circ$ orientation. ....	108
Figure 85.	Detection coverage at S-Band for 1 Tx at 5 km range and target at $0^\circ$ orientation. ....	109
Figure 86.	Detection coverage at S-Band for 1 Tx at 15 km range and target at $0^\circ$ orientation. ....	109
Figure 87.	Detection coverage at S-Band for 2 Tx at 5 km range and target at $0^\circ$ orientation. ....	110
Figure 88.	Detection coverage at S-Band for 2 Tx at 15 km range and target at $0^\circ$ orientation. ....	110
Figure 89.	Detection coverage at S-Band for 4 Tx at 5 km range and target at $0^\circ$ orientation. ....	111
Figure 90.	Detection coverage at S-Band for 4 Tx at 15 km range and target at $0^\circ$ orientation. ....	111
Figure 91.	Detection coverage at S-Band for 8 Tx at 5 km range and target at $0^\circ$ orientation. ....	112
Figure 92.	Detection coverage at S-Band for 8 Tx at 15 km range and target at $0^\circ$ orientation. ....	112
Figure 93.	Detection coverage at S-Band for 4 Tx in receiver-centered geometry and target at $0^\circ$ orientation. ....	113
Figure 94.	Detection coverage at S-Band for 4 Tx in receiver-centered geometry and target at $-90^\circ$ orientation. ....	113
Figure 95.	Detection coverage at S-Band for 4 Tx in receiver-centered geometry and target at $45^\circ$ orientation. ....	114
Figure 96.	Detection coverage at S-Band for 4 Tx in receiver-centered geometry and target at $30^\circ$ orientation. ....	114

Figure 97.	Detection coverage at S-Band for 4 Tx in transmitter-clustered geometry and target at $0^\circ$ orientation. ....	115
Figure 98.	Detection coverage at S-Band for 4 Tx in transmitter-clustered geometry and target at $-90^\circ$ orientation. ....	115
Figure 99.	Detection coverage at S-Band for 4 Tx in transmitter-clustered geometry and target at $45^\circ$ orientation. ....	116
Figure 100.	Detection coverage at S-Band for 4 Tx in transmitter-clustered geometry and target at $30^\circ$ orientation. ....	116
Figure 101.	Detection coverage at S-Band for 8 Tx randomly positioned around Rx at 5–20 km range and target at $0^\circ$ orientation. ....	117
Figure 102.	Detection coverage at S-Band for 8 Tx randomly positioned around Rx at 5–30 km range and target at $0^\circ$ orientation. ....	117
Figure 103.	Detection coverage at S-Band for 20 Tx randomly positioned around Rx at 5–20 km range and target at $0^\circ$ orientation. ....	118
Figure 104.	Detection coverage at S-Band for 20 Tx randomly positioned around Rx at 5–30 km range and target at $0^\circ$ orientation. ....	118
Figure 105.	Detection coverage at S-Band for 8 Tx randomly positioned around Rx at 5–20 km range and target at $-90^\circ$ orientation. ....	119
Figure 106.	Detection coverage at S-Band for 8 Tx randomly positioned around Rx at 5–30 km range and target at $-90^\circ$ orientation. ....	119
Figure 107.	Detection coverage at S-Band for 20 Tx randomly positioned around Rx at 5–20 km range and target at $-90^\circ$ orientation. ....	120
Figure 108.	Detection coverage at S-Band for 20 Tx randomly positioned around Rx at 5–30 km range and target at $-90^\circ$ orientation. ....	120
Figure 109.	Detection coverage at S-Band for 8 Tx randomly positioned around Rx at 5–20 km range and target at $45^\circ$ orientation. ....	121
Figure 110.	Detection coverage at S-Band for 8 Tx randomly positioned around Rx at 5–30 km range and target at $45^\circ$ orientation. ....	121
Figure 111.	Detection coverage at S-Band for 20 Tx randomly positioned around Rx at 5–20 km range and target at $45^\circ$ orientation. ....	122
Figure 112.	Detection coverage at S-Band for 20 Tx randomly positioned around Rx at 5–30 km range and target at $45^\circ$ orientation. ....	122
Figure 113.	Detection coverage along target's path (2 km resolution) at S-Band for 4 Tx. RCS computed by calling FEKO. ....	123
Figure 114.	SNR at receiver along target's path (2 km resolution) at S-Band for 4 Tx. RCS computed by calling FEKO. ....	123
Figure 115.	Detection coverage along target's path (100 m resolution) at S-Band for 4 Tx. RCS extracted from pre-computed RCS table. ....	124
Figure 116.	SNR at receiver along target's path (100 m resolution) at S-Band for 4 Tx. RCS extracted from pre-computed RCS table. ....	124
Figure 117.	Detection coverage along target's path (100 m resolution) at S-Band for 8 Tx randomly position. RCS extracted from pre-computed RCS table. ....	125
Figure 118.	SNR at receiver along target's path (100 m resolution) at S-Band for 8 Tx randomly position. RCS extracted from pre-computed RCS table. ....	125

Figure 119.	Target location errors using elliptical method (S-Band, 4 Tx at 5 km range) and SNR-independent measurement errors. ....	127
Figure 120.	Target location errors using hyperbolic method (S-Band, 4 Tx at 5 km range) and SNR-independent measurement errors. ....	127
Figure 121.	Target location errors using elliptical method (S-Band, 8 Tx at 5 km range) and SNR-independent measurement errors. ....	128
Figure 122.	Target location errors using hyperbolic method (S-Band, 8 Tx at 5 km range) and SNR-independent measurement errors. ....	128
Figure 123.	Target location errors using elliptical method (S-Band, 4 Tx at 15 km range) and SNR-independent measurement errors. ....	129
Figure 124.	Target location errors using hyperbolic method (S-Band, 4 Tx at 15 km range) and SNR-independent measurement errors. ....	129
Figure 125.	Target location errors using elliptical method (S-Band, 8 Tx at 15 km range) and SNR-independent measurement errors. ....	130
Figure 126.	Target location errors using hyperbolic method (S-Band, 8 Tx at 15 km range) and SNR-independent measurement errors. ....	130
Figure 127.	Target location errors using elliptical method (S-Band, 4 Tx clustered) and SNR-independent measurement errors. ....	131
Figure 128.	Target location errors using hyperbolic method (S-Band, 4 Tx clustered) and SNR-independent measurement errors. ....	131
Figure 129.	Target location errors using elliptical method (S-Band, 8 Tx clustered) and SNR-independent measurement errors. ....	132
Figure 130.	Target location errors using hyperbolic method (S-Band, 8 Tx clustered) and SNR-independent measurement errors. ....	132
Figure 131.	Target location errors using elliptical method (S-Band, 4 Tx at 5 km range) and SNR-dependent measurement errors. ....	133
Figure 132.	Target location errors using hyperbolic method (S-Band, 4 Tx at 5 km range) and SNR-dependent measurement errors. ....	133
Figure 133.	Target location errors using elliptical method (S-Band, 8 Tx at 5 km range) and SNR-dependent measurement errors. ....	134
Figure 134.	Target location errors using hyperbolic method (S-Band, 8 Tx at 5 km range) and SNR-dependent measurement errors. ....	134
Figure 135.	Target location errors using elliptical method (S-Band, 4 Tx at 15 km range) and SNR-dependent measurement errors. ....	135
Figure 136.	Target location errors using hyperbolic method (S-Band, 4 Tx at 15 km range) and SNR-dependent measurement errors. ....	135
Figure 137.	Target location errors using elliptical method (S-Band, 8 Tx at 15 km range) and SNR-dependent measurement errors. ....	136
Figure 138.	Target location errors using hyperbolic method (S-Band, 8 Tx at 15 km range) and SNR-dependent measurement errors. ....	136
Figure 139.	Target location errors using elliptical method (S-Band, 8 Tx at random positions) and SNR-dependent measurement errors. ....	137
Figure 140.	Target location errors using hyperbolic method (S-Band, 8 Tx at random positions) and SNR-dependent measurement errors. ....	137



Figure 141.	Target location errors using elliptical method (S-Band, 4 Tx clustered) and SNR-dependent measurement errors. ....	138
Figure 142.	Target location errors using hyperbolic method (S-Band, 4 Tx clustered) and SNR-dependent measurement errors.....	138
Figure 143.	Target location errors using elliptical method (S-Band, 8 Tx clustered) and SNR-dependent measurement errors. ....	139
Figure 144.	Target location errors using hyperbolic method (S-Band, 8 Tx clustered) and SNR-dependent measurement errors.....	139

THIS PAGE INTENTIONALLY LEFT BLANK

## LIST OF TABLES

Table 1.	Parameters of significant passive bistatic radar programs designed and tested for air surveillance. After [5].	5
Table 2.	Signal parameters for typical passive radar illumination sources. From [23].	7
Table 3.	Target path information format in Excelsheet.	38
Table 4.	RCS table format in Excelsheet.	41
Table 5.	Percentage of grid points with SNR greater than 10 dB within a 10 km radius centered at the receiver. Target orientation at $0^\circ$ .	54
Table 6.	Percentage of grid points with SNR greater than 10 dB within a 10 km radius centered at the receiver. Target orientation at $-90^\circ$ .	54
Table 7.	Percentage of grid points with SNR greater than 10 dB within a 20 km radius centered at the receiver. Target orientation at $0^\circ$ .	56
Table 8.	Chi-square distribution table.	83

THIS PAGE INTENTIONALLY LEFT BLANK

## LIST OF ACRONYMS AND ABBREVIATIONS

AIS	automatic identification system
AOA	angle of arrival
ARM	anti-radiation missile
BRRE	bistatic radar range equation
CFAR	constant false alarm rate
CMR	civil marine radar
CST	Computer Simulation Technology
DAB	digital audio broadcasting
DF	direction finding
DGPS	Differential Global Positioning System
DOP	dilution of precision
drms	distance root mean square
DVB-T	digital video broadcasting terrestrial
EA	electronic attack
ESM	electronic support measures
EW	electronic warfare
FEKO	field calculations for bodies with arbitrary surface (Feldberechnung für Körper mit beliebiger Oberfläche)
FFI	The Norwegian Defence Research Establishment (Forsvarets forskningsintitutt)
FM	frequency modulation
FSR	forward-scattering radar
GPS	Global Positioning System
HF	high frequency
ISAR	inverse synthetic aperture radar
LOS	line-of-sight
LPI	low probability of intercept
MIMO	multiple-input multiple-output
MTI	moving target indicator
MWS	Microwave Studio

OODA	observe–orient–decide–act
PBR	passive bistatic radar
pdf	probability density function
PMR	passive multistatic radar
RAM	radar-absorbent material
RCS	radar cross section
rms	root mean square
rss	root-sum-squared
SAR	synthetic aperture radar
SNR	signal-to-noise ratio
STAP	space time adaptive processing
TDOA	time difference of arrival
UHF	ultra-high frequency
USCG	U.S. Coast Guard
UWB	ultra-wideband
VHF	very high frequency

## **ACKNOWLEDGMENTS**

I would like to extend my deepest appreciation and gratitude to the following people who have contributed one way or another in making this study possible.

Dr. David C. Jenn, thesis advisor, for his valuable support, advice, and guidance leading to the completion of this thesis. His knowledge and experience helped me better understand the issues at hand and overcome difficulties during the duration of this study.

Mr. Edward Fisher, thesis co-advisor, for his support and provisions rendered during my course of study at NPS whilst allowing me the freedom to explore this thesis topic.

DSO National Laboratories, for supporting my decision to pursue my master's education at NPS.

ME5 Chong Sze Sing, Republic of Singapore Navy (RSN), for the discussions that led to a better understanding of the topic of using opportunistic transmitters for the detection of maritime targets.

Lastly, I would like to express my immeasurable appreciation to my family and friends for their understanding and unwavering support as I seek to further my studies.

THIS PAGE INTENTIONALLY LEFT BLANK



# I. INTRODUCTION

## A. OVERVIEW

Since the concept of radar engineering was first demonstrated in 1904, progress in radar technology has been driven by growing requirements for radar performance and rapidly changing operating environment. A long detection range and wide coverage, measurement accuracy, greater system capacity, and an ability to operate with the presence of interference are some of the fundamental radar requirements that have been established over the past few decades [1]. These radar performance characteristics—together with the need to detect, separate, classify, locate, and track sources of emissions in multi-target environments—triggered the development of passive radar detection and location techniques.

The vast majority of today's deployed radar systems are monostatic, that is, the transmitting and receiving antennas are collocated. Despite the advancements in antennas, transmitters, receivers, and processing technology, as well as passive radar systems, conventional monostatic radar remains a double-edged sword—whereby it detects targets, but radar transmission makes it vulnerable to detection—and may not be the best option to address certain operational scenarios. A promising solution is to use multiple radar transmitting and receiving sites to exploit spatial advantage for coordinated target detection. Multi-site radars can be broadly classified into bistatic radar and multistatic radar. *Bistatic radar* is a radar system where the transmitter and receiver are located at different sites [2]. Similarly, a *multistatic radar* system utilizes multiple spatially separated transmitter and receiver sites where the target information from all receivers is fused [1]. Passive bistatic or multistatic radar capitalizes on transmitters of opportunity to detect and locate sources of transmission or targets without deliberate emissions. The illuminators are not limited to radar signals and include (but are not limited to) analog TV, FM radio, digital video broadcasting terrestrial (DVB-T), digital audio broadcasting (DAB), cellular network, WiFi, and Global Positioning System (GPS) satellite signals [3].

In naval operations, targets employing low radar cross section (RCS) and radar-absorbent material (RAM) design methods, coupled with the use of highly sensitive electronic warfare (EW) receivers on warships, have changed the nature of the game. Military ships are pressured to limit transmissions to avoid detection by highly sensitive EW receivers. Furthermore, the use of low probability of intercept (LPI) radar in a monostatic configuration results in weak returns from low-RCS targets, restricting detection capability and compromising situational awareness. This thesis explores the use of multiple pairs of passive bistatic radar (PBR) to detect low-RCS targets using opportunistic transmissions as a possible solution and to validate the findings in [4]. Figure 1 shows the bistatic radar geometry for a PBR pair. The direct line-of-sight (LOS) distance between the transmitter (Tx) and receiver (Rx) is known as the baseline and is denoted by  $L$ . The distance between the transmitter and target is denoted as  $R_T$  while the distance between the receiver and the target is denoted as  $R_R$ . The bistatic angle  $\beta$  is the angle subtended between transmitter, target, and receiver.

The proposed PBR approach offers potential advantage in the detection of stealthy, low-RCS targets which are designed to minimize monostatic radar echoes. RCS returns of stealthy ships vary with bistatic angle  $\beta$  and can be sufficiently large at certain return directions. PBR capitalizes on this characteristic using opportunistic transmissions to detect low-RCS targets. Being a passive system, PBR allows the receiver to remain covert, making it more resilient to detection and electronic attack (EA)—in the form of jamming and anti-radiation missiles (ARMs). The ability to leverage available transmission and to detect targets passively also serves to enhance situational awareness, thereby advancing one's position in the observe–orient–decide–act (OODA) loop during an operation [4]. It is also advantageous to use multiple transmitters at separate locations for detection as it adds spatial diversity, which enhances detection accuracy and aids in removing clutter, interference, and potential system errors. Lastly, the PBR system proposed requires no additional equipment as all necessary hardware is currently available on most naval ships.

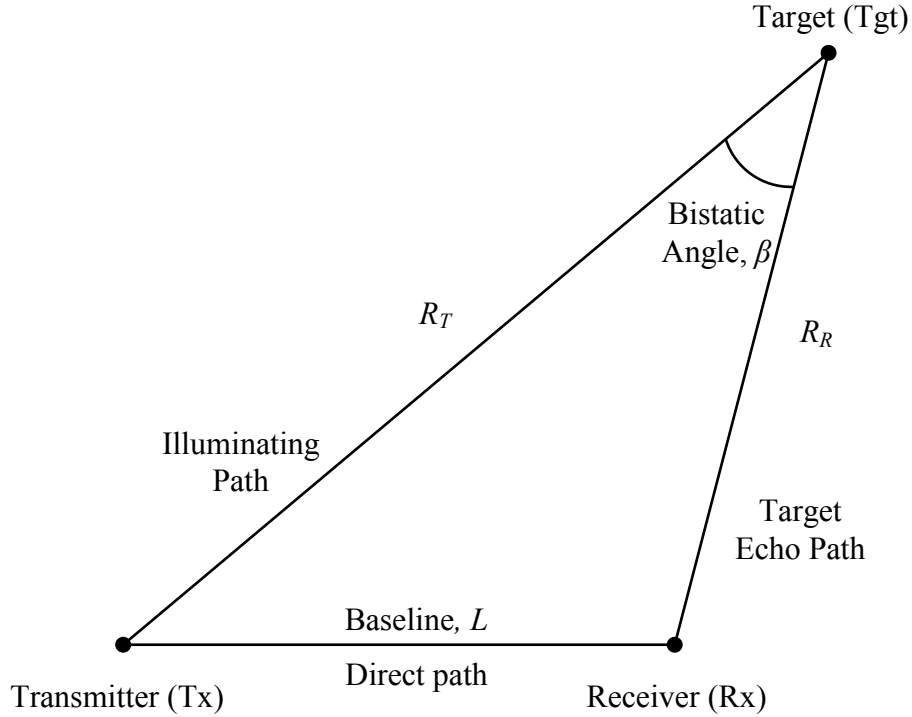


Figure 1. Bistatic radar geometry.

## B. HISTORY

The concept of Radio Detection and Ranging (RADAR) was first demonstrated in 1904 by German inventor Christian Hülsmeyer in a monostatic setup [5]. Following this, radar experiments in the United States, the United Kingdom, France, Italy, Russia, and Japan were carried out predominantly with bistatic radar operating in the forward-scattering configuration [6]. However, the invention of the radar duplexer in 1936 addressed the issue of transmitter-receiver isolation and broadened the application of single-site radar on aircraft, ships, and mobile ground units. By the end of World War II, bistatic radar was displaced by monostatic radar, with the former experiencing periodic resurgences [5].

### 1. First Resurgence

The 1950s saw renewed interest in bistatic radar with developments in missile and satellite detection, location and tracking, semi-active homing missiles, hitchhiking, and second-generation forward-scattering fences [2]. During this period, advancement in

radar theory led to a better appreciation of concepts on match filtering, ambiguity functions, statistical theories on detection, moving target indicator (MTI) radar, and synthetic aperture radar (SAR) [7–9]. The term *bistatic radar* originated with K. M. Siegel and R. E. Machol in 1952 [10].

## **2. Second Resurgence**

The development of counter-measures to anti-radiation missiles (ARMs) and emitter location-directed artillery in the 1970s resulted in the second resurgence in bistatic radar. With a dual or multiple site configuration, the effectiveness of electronic support measures (ESM) directed attacks can be reduced by locating the transmitter away from the receiver or into a less vulnerable sanctuary [5]. The advent of digital processing techniques during this period increased the processing capability in MTI operation modes and allowed real-time airborne SAR mapping [7].

## **3. Third Resurgence**

Research on bistatic space–time adaptive processing (STAP) to address moving clutter and concepts to improve bistatic SAR images signaled the start of the third resurgence. It was also during this period that passive bistatic radar surfaced as a possible counter stealth technique. The idea for PBR is to utilize commercial broadcast signals in bistatic or multistatic configurations to detect low-RCS targets [5]. Since then, several PBR systems have been developed and evaluated for air surveillance. Some notable PBR air surveillance systems are listed in Table 1.

Table 1. Parameters of significant passive bistatic radar programs designed and tested for air surveillance.\* After [5].

System	Silent Sentry™	TV-Based Bistatic Radar (I)	TV-Based Bistatic Radar (II)	FM Radio – Based Bistatic Radar	Multistatic HDTV-Based Radar
Developer	IBM, now Lockheed Martin	Univ College London	DERA, United Kingdom	NATO	SAIC, U.S. Army
Decade configuration	1980 – 2000	1980	1990	2000	2000
Transmitter operation	Multistatic: Rx: 1 Tx: up to 6	Bistatic	Bistatic Near-forward scatter	Bistatic	Multistatic: Rx: 4 Tx: 1
Baseline	100 km typical	12 km	150 km	50 km	10 km typical
Target	Aircraft Missile launches	Aircraft	Aircraft	Aircraft	Aircraft below ~ 5000 ft
Target data	Range Doppler Bearing	Range Bearing	Doppler Bearing	Range Doppler Bearing	Range Doppler
Measured performance	$R_M = 100$ km – 150 km 2-D tracks on A/C 3-D tracks on missile launches	$R_M \sim 25$ km Occasional A/C detections, but mostly negative	$R_M \sim 160$ km Detections on high and medium altitude A/C but only 1/3 tracked	$R_M \sim 175$ km Achieved with innovative direct path excision	$R_M \sim 30$ km Target location via multi-lateration Ghost excision via Doppler association
Status	Version 3 for sale to U.S. Government for < 1 million dollars Work continues	Program ended	Program ended	Program continuing possible in a multistatic mode	Test phase complete Awaiting evaluation/funding

\*  $R_M$  is the equivalent maximum monostatic range defined as  $(R_R R_T)_{\max}^{1/2} = R_M$ , where  $R_R$  is the receiver-to-target range and  $R_T$  is the transmitter-to-target range.

### C. RECENT DEVELOPMENTS IN BISTATIC AND MULTISTATIC RADAR

Despite research progress on improving the detection, classification, and location performance of passive bistatic radar systems, their reliance on transmissions of opportunity and the restricted geometry has limited their application. This fundamental requirement continues to stimulate research and experimentation on opportunistic illuminating sources, their optimum configuration, applicability, and performance in various operational scenarios. As with all radar systems, improvement in interference and clutter rejection, target detection, classification, and location and tracking accuracy are current areas of interest in the field of passive bistatic radar and passive multistatic radar (PMR). The recent research topics in bistatic and multistatic radar can be classified as bistatic and multistatic system configuration, forward-scattering radar, and multiple-input multiple-output (MIMO) radar.

When the concept of bistatic and multistatic radar was first introduced, dedicated radar transmitters were used as transmission sources [11] before transmitters of opportunity were employed as illuminating sources. Transmitters of opportunity in the very high frequency (VHF) and ultra-high frequency (UHF) band, such as FM broadcast, TV broadcast, DAB, DVB-T, and cellular network signals continue to be common illuminating sources used in detecting airborne, land, and maritime targets [11–19]. Conversely, studies on the use of high frequency (HF) band signals as opportunistic transmitters only started recently. HF signals present advantages of long range detection and coverage, propagation beyond the radar horizon, and improved detection of stealth targets, which enhances the PBR/PMR’s early warning capability [20, 21]. A list of common transmission sources and their typical parameters are given in Table 2.

Apart from terrestrial sources of transmission, there has been recent interest in using satellite transmissions to detect airborne targets. The SABER-DEMO platform recently demonstrated its ability to detect aircraft passively using signal processing techniques to process weak satellite sources of transmission [22].

Table 2. Signal parameters for typical passive radar illumination sources.  
From [23].

Transmission	Frequency	Modulation, Bandwidth	$P_t G_t$	Power Density ( $\text{Wm}^{-2}$ ) $\Phi = \frac{P_t G_t}{4\pi r_1^2}$
<b>HF broadcast</b>	10-30 MHz*	DSB AM, 9 kHz	50 MW	-67 to -53 dBW $\text{m}^{-2}$ at $r_1$ = 1000 km
<b>VHF FM (analogue)</b>	~100 MHz	FM, 50 kHz	250 kW	-57 dBW $\text{m}^{-2}$ at $r_1$ = 100 km
<b>UHF TV (analogue)</b>	~550 MHz	Vestigial-Sideband AM (vision); FM(sound), 5.5 MHz	1 MW	-51 dBW $\text{m}^{-2}$ at $r_1$ = 100 km
<b>Digital audio broadcast</b>	~220 MHz	digital, OFDM 220 kHz	10 kW	-71 dBW $\text{m}^{-2}$ at $r_1$ = 100 km
<b>Digital TV</b>	~750 MHz	digital, 6 MHz	8 kW	-72 dBW $\text{m}^{-2}$ at $r_1$ = 100 km
<b>Cellphone base station (GSM)</b>	900 MHz, 1.8 GHz	GMSK, FDM/TDMA/FDD 200 kHz	100 W	-81 dBW $\text{m}^{-2}$ at $r_1$ = 10 km
<b>Cellphone base station (3G)</b>	2 GHz	CDMA 5 MHz	100 W	-81 dBW $\text{m}^{-2}$ at $r_1$ = 100 km

\*Appropriate frequency will depend on time of day.

Another topic of interest is the use of inverse synthetic aperture radar (ISAR) processing techniques with forward-scattering radar (FSR) for target detection and parameter extraction. FSR is the earliest form of bistatic radar where target detection occurs at the transmitter to receiver baseline. The target's radar cross section is enhanced in the forward-scattering configuration due to Babinet's principle [2]. Using the constant false alarm rate (CFAR) approach, target detection and parameter extraction can be accomplished in real time [24]. An experiment conducted at Forsvarets forskningsintitut (FFI) explores the difference in ISAR ship signatures in the forward and back-scattering configurations. The results from the study show that forward-scattering returns produce more accurate ISAR signatures than back-scattering returns as the RCS for forward-scattering is usually stronger than back-scattering. The difference between forward and back-scattering ISAR signatures can be fused to improve ship identification and

classification [25]. Apart from studies on FSR processing techniques to improve target detection and extraction, considerable research has been conducted on ultra-wideband (UWB) FSR for its ability to reduce sea clutter in maritime applications [26, 27].

Recent advances and interest in MIMO radar systems can be attributed to its potential for detection and location of targets in bistatic or multistatic configurations. Spatial diversity in MIMO radar systems exploits the differences in target cross section in detecting and extracting target parameters such as angle of arrival (AOA) and Doppler frequencies [28]. Furthermore, coherent processing in MIMO systems improves target location accuracy [28, 29].

As with all studies in the radar domain, current bistatic and multistatic research areas are motivated by the need to improve detection capability and measurement accuracy while reducing or mitigating the effects of unwanted interference.

#### **D. THESIS OBJECTIVE**

The primary objectives of this thesis are as follows:

1. Generate a MATLAB model that computes a system's detection performance given the target's path.
2. Examine low-RCS maritime target detection coverage and performance using multiple pairs of bistatic radar.
3. Investigate low-RCS maritime target location accuracy using elliptical and hyperbolic target location methods.

The EM simulation software FEKO will be employed to model and analyze the RCS scattering properties of the maritime target while MATLAB will be used to model and simulate the operating environment and PBR target detection and location. The MATLAB model is validated against open source literature by using simple targets with known RCS return characteristics prior to using the models to generate simulation results.

The MATLAB model generated for objective (1) requires the user to provide an Excel file with the target's position and velocity vector components at each time step, after which detection performance parameters will be computed. This model will be a fully automated MATLAB model that calls FEKO to compute precise RCS returns given the exact incident and receive angles. Detection coverage results from objective (2) will



be compared against findings in [4] and used to propose the optimal PBR configuration and geometry for maximum detection coverage. Target location estimation results from objective (3) will be used to examine the effects of PBR geometry on location error distribution.

The maritime scenario with a single receiver and multiple transmitters depicted in Figure 2 applies to all models. The problem setup assumes a warship (receiver) equipped with broadband EW receiver and direction finding (DF) capability deployed to monitor maritime traffic flow in the Straits of Singapore. The targets are assumed to be low-RCS targets with infrequent transmissions and/or operating with LPI radars, while civil marine radars (CMR) on merchant ships will serve as opportunistic illuminators in a PBR configuration [4]. Regulation 19 of SOLAS Chapter V requires all merchant and warships to carry automatic identification systems (AISs), which share information on the ship's identity, position, course, speed, navigation status, and safety-related information [30].

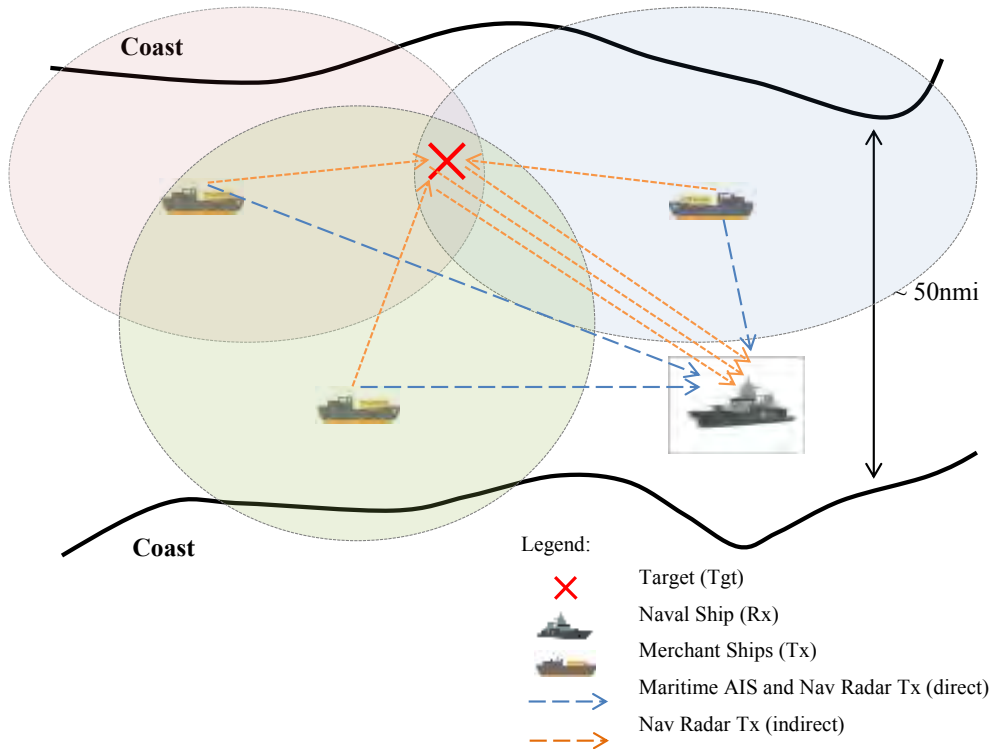


Figure 2. Pictorial representation of the PBR setup. After [4].

## **E. THESIS CHAPTER OUTLINE**

Chapter I introduced the concept, history, and recent developments in passive bistatic radar. The goals and end products of the thesis are also detailed here.

Chapter II provides the theoretical background on PBR. The corresponding parameters employed to develop the necessary MATLAB model are introduced. The bistatic range equations, detection contours, and mathematical concepts related to target location and uncertainty are covered.

Chapter III presents the design approach in modeling the scenario and the problem setup using FEKO and MATLAB. The results from verifying the detection coverage models using simple targets and PBR geometry against known results are covered in detail. The methodology used to verify target location model is also discussed.

Chapter IV uses the model generated to examine detection coverage for different PBR transmitter-target-receiver geometries. Simulation results are compared against findings in [4] and used to propose PBR configurations and geometry for optimal detection coverage. The results for elliptical and hyperbolic target location methods and their corresponding uncertainty ellipse are presented. The effects of transmitter-target-receiver geometry target location accuracy are also explored.

Chapter V summarizes the research findings and suggests further work to improve the models and multiple PBR detection, parametric extraction, and location capability and accuracy.

## II. BISTATIC RADAR THEORY

### A. DEFINITION

*Bistatic radar* refers to a radar system where the transmitter and receiver are at sufficiently different locations such that the angles or ranges from those locations to the target are significantly different [31]. The basic bistatic configuration and parameters are defined in Figure 1.

### B. RANGE EQUATION

The bistatic radar range equation (BRRE) gives the received power at Rx as a function of the system parameter, target scattering properties, and engagement geometry. Solving the BRRE for the range product gives [2]

$$\kappa = (R_T R_R)_{\max} = \left[ \frac{P_T G_T G_R \lambda^2 \sigma_B F_T^2 F_R^2 G_p}{(4\pi)^3 k T_s B_n (S / N)_{\min} L_T L_R} \right]^{1/2} \quad (1)$$

where

$R_T$  = transmitter-to-target range,

$R_R$  = receiver-to-target range,

$P_T$  = transmitter power output,

$G_T$  = transmitting antenna power gain,

$G_R$  = receiving antenna power gain,

$\lambda$  = wavelength,

$\sigma_B$  = bistatic target cross section,

$F_T$  = pattern propagation factor for transmitter-to-target path,

$F_R$  = pattern propagation factor for target-to-receiver path,

$G_p$  = processing gain,

$k$  = Boltzmann's constant ( $1.38 \times 10^{-23}$  J/K ),

$T_s$  = receiving system noise temperature,

$B_n$  = noise bandwidth of receiver's pre-detection filter, sufficient to pass all spectral components of the transmitted signal,

$(S/N)_{\min}$  = signal-to-noise power ratio required for detection,

$L_T$  = transmitting system losses ( $>1$ ) not included in other parameters,

$L_R$  = receiving system losses ( $>1$ ) not included in other parameters,

$\kappa$  = bistatic maximum range product.

In the bistatic range equation, the maximum range product  $R_T R_R$  replaces  $R^2$  in the monostatic range equation where  $R = R_T = R_R$  is the monostatic transmitter-to-target and target-to-receiver range. The difference between the transmission path and receiving path results in significant differences between monostatic and bistatic radar operation.

One of the differences is that monostatic contours of equal signal strength are constant range circles, while detection contours for bistatic radar are defined by ovals of Cassini. An oval of Cassini is defined as a locus of points where the product of the distance from two fixed points is constant. Figure 3 shows the Cassini oval for two fixed points ( $F_1$  and  $F_2$ ) separated by a distance of  $2c$ .

Applying the concept of Cassini ovals to the bistatic triangle in Figure 4 with baseline  $L$  and range product  $R_T R_R$ , an expression for constant signal-to-noise (SNR) power ratio can be derived by writing Eq. 1 as [2]

$$S/N = \frac{K}{R_T^2 R_R^2} \quad (2)$$

where  $S/N$  is the signal-to-noise power ratio at  $R_T$  and  $R_R$ , and  $K$  is the bistatic radar constant

$$K = \frac{P_T G_T G_R \lambda^2 \sigma_B F_T^2 F_R^2}{(4\pi)^3 k T_s B_n L_T L_R}. \quad (3)$$

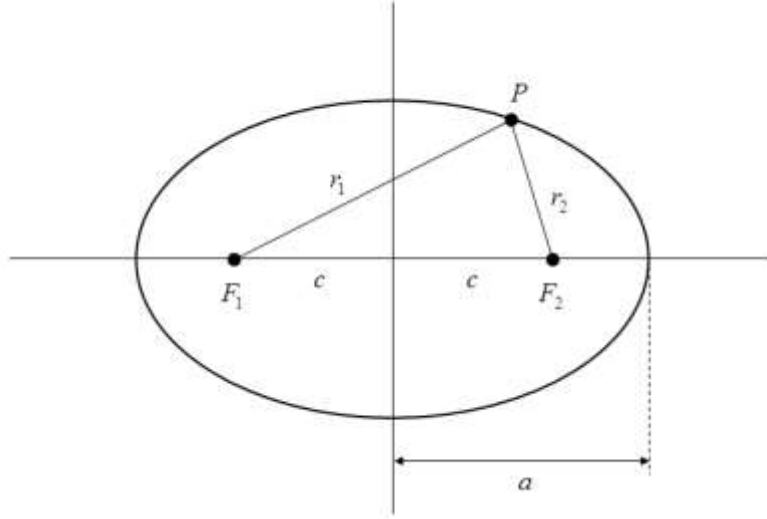


Figure 3. Cassini oval for  $c < b$  where  $b = r_1 r_2$ .

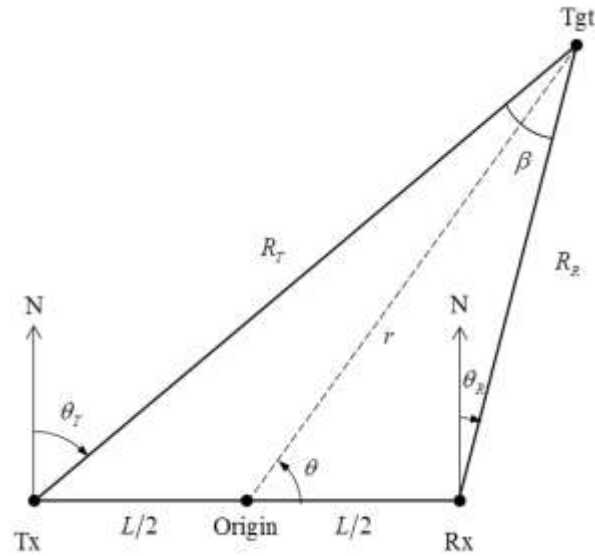


Figure 4. Bistatic radar geometry for converting North-referenced coordinates into polar coordinates. After [2].

From the geometry in Figure 4,  $R_T$  and  $R_R$  are converted to polar coordinates  $(r, \theta)$  using the law of cosines:

$$R_T^2 = (r^2 + L^2/4) + rL \cos \theta, \quad (4)$$

$$R_R^2 = (r^2 + L^2/4) - rL \cos \theta, \quad (5)$$

where the origin is at the midpoint of the baseline. Substituting Eq. 3, Eq.4, and Eq. 5 into Eq. 2 gives an expression that defines constant SNR contours [2]:

$$S/N = \frac{K}{(r^2 + L^2/4)^2 - r^2 L^2 \cos^2 \theta}. \quad (6)$$

Signal-to-noise ratio contours generated using Eq. 6 for  $10 \text{ dB} \leq S/N \leq 30 \text{ dB}$  and  $K = 30L^4$  are given in Figure 5.

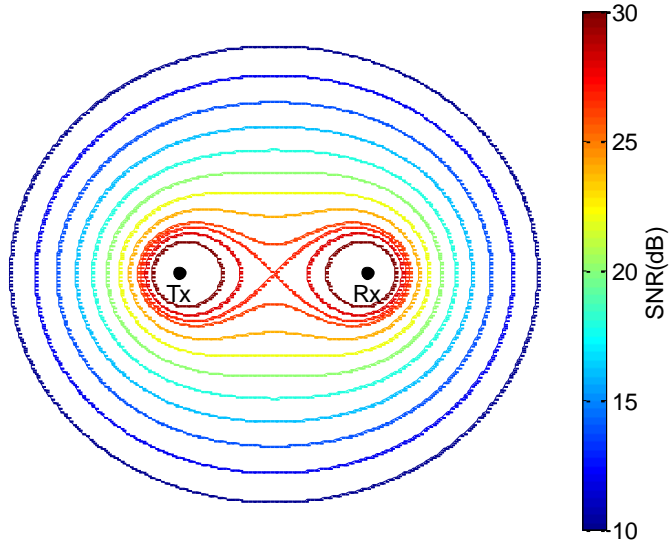


Figure 5. Ovals of Cassini, contours of constant SNR (dB), with  $K = 30L^4$ . After [2].

Given that  $L$ ,  $(R_T + R_R)$  and  $\theta_R$  are obtained and measured from the opportunistic transmitter and receivers,  $R_T$  and  $R_R$  are computed as [2]

$$R_T = (R_R^2 + L^2 + 2R_R L \sin \theta_R)^{1/2}, \quad (7)$$

$$R_R = \frac{(R_T + R_R)^2 - L^2}{2(R_T + R_R + L \sin \theta_R)}. \quad (8)$$

Using the law of cosines on the bistatic triangle in Figure 4 yields

$$\beta = \cos^{-1} \left( \frac{R_T^2 + R_R^2 - L^2}{2R_T R_R} \right). \quad (9)$$

When  $L = 2\sqrt{\kappa}$ , the oval forms a lemniscate with cusp at the origin. The ovals of Cassini in Figure 5 define three operating regions for bistatic radar:

1.  $L > 2\sqrt{\kappa}$  with  $R_T \gg R_R$ . Receiver centered region.
2.  $L > 2\sqrt{\kappa}$  with  $R_R \ll R_T$ . Transmitter centered region.
3.  $L < 2\sqrt{\kappa}$ . Cosite region or receiver-transmitter-centered region.

In cases where the target echo signal strength is weak, non-coherent pulse integration performed after the envelop detector increases SNR by a factor of  $\sqrt{N}$  where  $N$  is the number of pulses integrated. Improvement in SNR by pulse integration is a form of processing gain. The number of pulses integrated over a period of  $t$  seconds is calculated as

$$N = PRF \times TOT \times t \quad (10)$$

$$TOT = \frac{\theta_{3dB}}{360} \frac{60}{\omega_{scan}} \quad (11)$$

where

$$\theta_{3dB} = 3 \text{ dB azimuth beamwidth,}$$

$$\omega_{scan} = \text{scan rate (rpm),}$$

$$TOT = \text{time on target,}$$

$$PRF = \text{pulse repetition frequency,}$$

$$t = \text{integration period.}$$

For the purpose of this thesis, the minimum difference between the noise floor and signal level is assumed to be 10 dB, that is, minimum SNR is 10 dB.

## C. TARGET LOCATION EQUATIONS

### 1. Bistatic Radar Trigonometry

The AOA of the target echo signal  $\theta_R$  and target-to-receiver range  $R_R$  are required to define the target's location with respect to the receiver in a PBR configuration. The AOA of the echo signal can be measured directly; however, the target-to-receiver range cannot be measured directly and needs to be calculated by solving the parameters of the bistatic triangle (Figure 4).

To solve for target-to-receiver range  $R_R$  and the rest of the bistatic triangle parameters requires measuring and knowledge of the following:

- Baseline range from transmitter position(s) and receiver position,  $L$ ,
- AOA of target echo signal at the receiver,  $\theta_R$ ,
- Transmitter-to-target and target-to-receiver range sum,  $(R_T + R_R)$ .

The range sum  $(R_T + R_R)$  can be estimated using the direct and indirect method as illustrated in Figure 6. In the direct method, the receiver measures the time delay  $\Delta T_{rt}$  between the reception of the transmitted pulse and the target echo. The range sum can then be expressed as a function of the time delay  $\Delta T_{rt}$  and the baseline range [2]:

$$(R_T + R_R) = c\Delta T_{rt} + L. \quad (12)$$

In the indirect method, the receiver measures the time delay  $\Delta T_{tt}$  between the transmission of the pulse and the reception of the target echo. The range sum in this case is a function of the time delay  $\Delta T_{tt}$  [2]:

$$(R_T + R_R) = c\Delta T_{tt}. \quad (13)$$

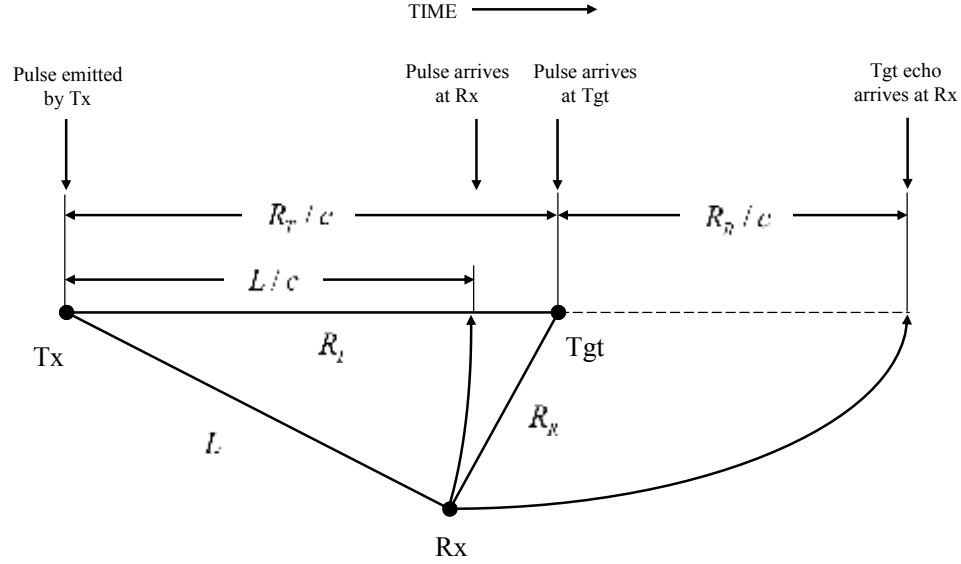
The indirect method requires receiver and transmitter clocks to be synchronized while the direct method can be used with any transmitter configurations given LOS between the transmitter and receiver.



Referring to Figure 7, the direct and reflected pulses received must be resolvable such that

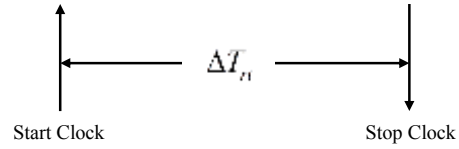
$$t_{\text{reflected}} > t_{\text{direct}} + \tau \quad (14)$$

**a) Timing Sequence**



**b) Direct Method**

$$R_T + R_R = c\Delta T_{dt} + L$$



**c) Indirect Method**

$$R_T + R_R = c\Delta T_{it}$$

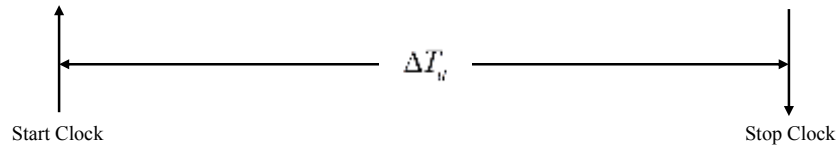


Figure 6. Timing sequence diagram for direct and indirect method for calculating range sum  $(R_T + R_R)$ . From [2].

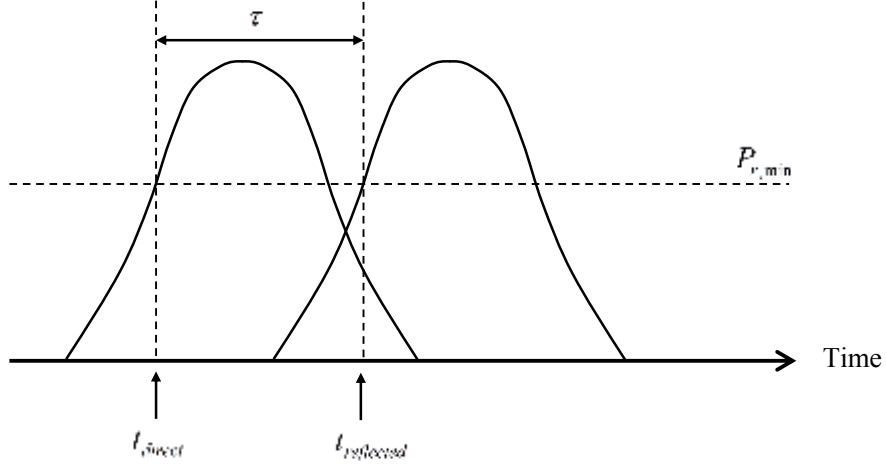


Figure 7. Reception of direct and reflected pulses.

To derive the mathematical relationship between the bistatic triangle parameters, first consider the elliptical iso-range contours on a bistatic plane such that each concentric ellipse is determined by

$$R_T + R_R = 2a, \quad (15)$$

where  $a$  is the semi-major axis length of the ellipse (Figure 3). The eccentricity of the ellipse  $e$  is therefore defined as

$$e = \frac{L}{2a}, \quad (16)$$

$$e = \frac{L}{(R_T + R_R)}. \quad (17)$$

Given the measurement of  $(R_T + R_R)$ ,  $L$ ,  $\theta_R$  and using the law of cosines on the bistatic triangle in Figure 4,

$$R_T^2 = R_R^2 + L^2 - 2R_R L \cos(90^\circ + \theta_R), \quad (18)$$

$$R_R = \frac{(R_T + R_R)^2 - L^2}{2(R_T + R_R + L \sin \theta_R)}, \quad (19)$$

$$R_T = (R_R^2 + L^2 + 2R_R L \sin \theta_R)^{1/2}. \quad (20)$$

Substituting the range sum  $(R_T + R_R)$  in Eqs. 19 and 20 using Eq. 17 yields

$$R_R = \frac{L(1 - e^2)}{2e(1 + e \sin \theta_R)}, \quad (21)$$

$$R_T = \frac{L(e^2 + 1 + 2e \sin \theta_R)}{2e(1 + e \sin \theta_R)}. \quad (22)$$

Using the law of sines on the bistatic triangle defines the relationship between the range and angle values as

$$\frac{R_R}{\sin(90^\circ - \theta_T)} = \frac{R_T}{\sin(90^\circ + \theta_R)} = \frac{L}{\sin \beta}. \quad (23)$$

Hence, the bistatic angle  $\beta$  is expressed as

$$\beta = \sin^{-1} \left( \frac{L \cos \theta_T}{R_R} \right), \quad (24)$$

$$\beta = \sin^{-1} \left( \frac{L \cos \theta_R}{R_T} \right). \quad (25)$$

The direct and indirect method of measuring range sum  $(R_T + R_R)$  applies to all target locations except when the target is in a forward-scattering configuration such that the target lies on the baseline between the transmitter and receiver. In the forward-scattering PBR configuration,  $(R_T + R_R) = L$  and  $\theta_R = -90^\circ$ , making  $R_R$  in Eq. 19 indeterminate [2].

In view of this limitation for PBR in forward-scattering configurations and inaccuracies arising from estimating the target's location using a single PBR with erroneous time delay and AOA measurements, as well as inaccurate transmitter and receiver position information, the following sub-section introduces the least-squares solution for fusing bistatic triangle parameters from all PBR pairs.

## 2. Least-Squares Intersection of Lines

In a realistic scenario, AOA and range information for each PBR pair derived from measurements and solving trigonometric equations do not result in bearings intersecting at a single point (Figure 8). The least-squares solution derived in [32] finds a point that minimizes the sum of perpendicular distances from this point to all the lines.

This method (i.e., the one that solves the bistatic triangle parameters and estimates the target location by least squares bearing intersection) is referred to as the elliptical target location method.

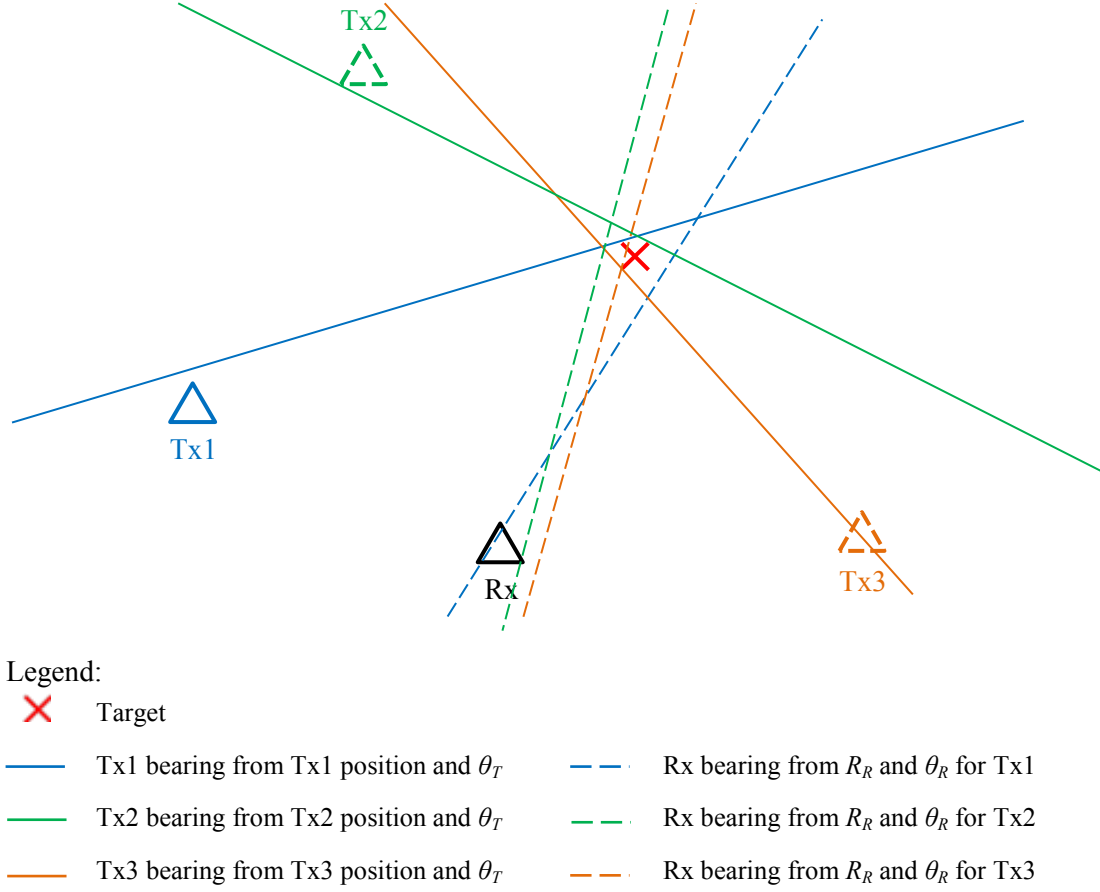


Figure 8. Least-squares intersection of lines solution to three PBR case.

A two-dimensional line is described by a point on the line

$$\mathbf{a} = \begin{bmatrix} a_1 \\ a_2 \end{bmatrix}, \quad (26)$$

and its corresponding unit direction vector

$$\mathbf{b} = \begin{bmatrix} b_1 \\ b_2 \end{bmatrix}, \quad \mathbf{b}^T \mathbf{b} = 1. \quad (27)$$

The squared perpendicular distance from a point  $\mathbf{p}$  to a line as illustrated in Figure 9 is expressed as

$$\begin{aligned} D(\mathbf{p}; \mathbf{a}, \mathbf{b}) &= \left\| (\mathbf{a} - \mathbf{p}) - ((\mathbf{a} - \mathbf{p})^T \mathbf{b}) \mathbf{b} \right\|_2^2 \\ &= (\mathbf{a} - \mathbf{p})^T (\mathbf{I} - \mathbf{b} \mathbf{b}^T) (\mathbf{a} - \mathbf{p}), \end{aligned} \quad (28)$$

and the sum of squared distance for  $K$  lines is

$$\begin{aligned} D(\mathbf{p}; \mathbf{a}, \mathbf{b}) &= \sum_{j=1}^K D(\mathbf{p}; \mathbf{a}_j, \mathbf{b}_j) \\ &= \sum_{j=1}^K (\mathbf{a}_j - \mathbf{p})^T (\mathbf{I} - \mathbf{b}_j \mathbf{b}_j^T) (\mathbf{a}_j - \mathbf{p}). \end{aligned} \quad (29)$$

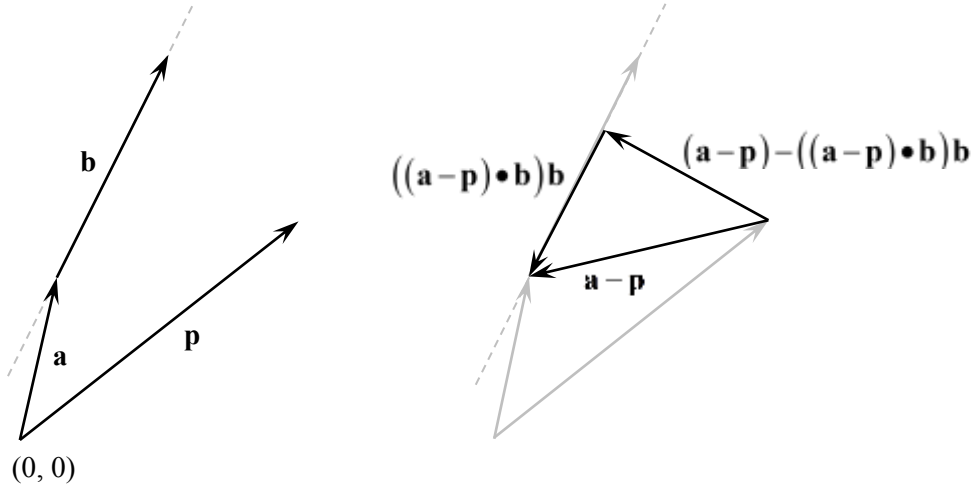


Figure 9. Perpendicular distance from a point to a line. From [32].

The corresponding objective function that finds the “best-fit” intersection point by minimizing the sum of squared distances for all lines is

$$\mathbf{p} = \arg \min_{\mathbf{p}} D(\mathbf{p}; \mathbf{A}, \mathbf{B}). \quad (30)$$

Taking the derivative of the cost function with respect to  $\mathbf{p}$

$$\frac{\partial D}{\partial \mathbf{p}} = \sum_{j=1}^K -2(\mathbf{I} - \mathbf{b}_j \mathbf{b}_j^T) (\mathbf{a}_j - \mathbf{p}) = 0, \quad (31)$$

$$\mathbf{S} \mathbf{p} = \mathbf{q}, \quad (32)$$

where

$$\mathbf{S} = \sum_{j=1}^K (\mathbf{I} - \mathbf{b}_j \mathbf{b}_j^T), \quad \mathbf{q} = \sum_{j=1}^K (\mathbf{I} - \mathbf{b}_j \mathbf{b}_j^T) \mathbf{a}_j. \quad (33)$$

Solving for  $\mathbf{p}$  in Eq. 32 gives the “best-fit” point of intersection

$$\mathbf{p} = \mathbf{S}^{-1} \mathbf{q}. \quad (34)$$

For each PBR pair, two lines are defined after solving for their bistatic triangle parameters: the transmitter-to-target bearing and the target-to-receiver bearing. The transmitter-to-target bearing is defined by the transmitter position and bistatic triangle parameter  $\theta_T$  while the target-to-receiver bearing is defined by the point determined by  $(\theta_R, R_R)$  and  $\theta_R$ . In a forward-scattering configuration, where  $R_R$  is indeterminate, the target-to-receiver bearing is defined by the receiver position and the bistatic triangle parameter  $\theta_R$ .

### 3. Hyperbolic Target Location

Apart from the elliptical target location method covered in Section II.C.1 and its extension in Section II.C.2, a target’s position can also be estimated using a hyperbolic location technique. To derive an iterative least-squares method of estimating the target’s location given time delay measurement from the direct method illustrated in Figure 6, consider a two-dimensional PBR pair in a multi-bistatic radar scenario (Figure 10).

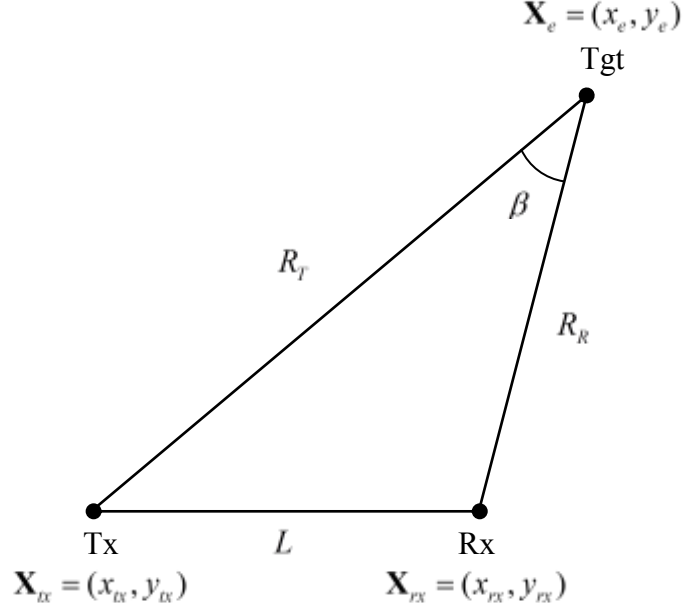


Figure 10. Single PBR in multi-bistatic radar scenario.

Given the coordinates of the target  $(x_e, y_e)$ , receiver position  $(x_{rx}, y_{rx})$  and transmitter positions  $(x_{tx,i}, y_{tx,i})$ , the noiseless time delay measurement in Eq. 12 can be rewritten as

$$c\Delta T_i = R_{T,i} + R_R - L_i \quad (35)$$

$$h_i(\mathbf{X}_e, \mathbf{X}_{tx,i}, \mathbf{X}_{rx}) = \sqrt{(x_e - x_{tx,i})^2 + (y_e - y_{tx,i})^2} + \sqrt{(x_e - x_{rx})^2 + (y_e - y_{rx})^2} - \sqrt{(x_{rx} - x_{tx,i})^2 + (y_{rx} - y_{tx,i})^2} \quad (36)$$

where

- $i$  = transmitter number  $i = 1, 2, \dots, K$ ,
- $K$  = number of transmitters,
- $R_{T,i}$  =  $i^{\text{th}}$  transmitter-to-target range,
- $R_R$  = target-to-receiver range,
- $L$  = baseline range,

$\Delta T_i$  = time delay between  $i^{\text{th}}$  transmitter's direct and indirect signal,

$\mathbf{X}_e$  = target's position vector,  $[x_e \ y_e]^T$ ,

$\mathbf{X}_{tx,i}$  =  $i^{\text{th}}$  transmitter's position vector,  $[x_{tx,i} \ y_{tx,i}]^T$ ,

$\mathbf{X}_{rx}$  = receiver position vector,  $[x_{rx} \ y_{rx}]^T$ .

When noisy time delay measurements are used to estimate the target location, Eq. 35 is written as

$$\begin{aligned} y_i &= c\Delta T_i + n_i \\ &= h_i(\mathbf{X}_e, \mathbf{X}_{tx,i}, \mathbf{X}_{rx}) + n_i \end{aligned} \quad (37)$$

where

$y_i$  =  $i^{\text{th}}$  noisy time delay measurement,

$\Delta T_i$  =  $i^{\text{th}}$  noiseless time delay measurement,

$n_i$  =  $i^{\text{th}}$  time delay measurement error.

Since the function in Eq. 36 is a non-linear function of the target, receiver, and transmitter positions, the function  $h_i(\mathbf{X}_e, \mathbf{X}_{tx,i}, \mathbf{X}_{rx})$  will be linearized by a Taylor series expansion about an initial estimate of the target's location  $(x_{e0}, y_{e0})$ . By retaining the first order terms, Eq. 37 can be written as

$$y_i - h_i(\mathbf{X}_{e0}, \mathbf{X}_{tx,i}, \mathbf{X}_{rx}) = \frac{\partial h_i}{\partial x_e} \Delta x_e + \frac{\partial h_i}{\partial y_e} \Delta y_e + n_i, \quad (38)$$

where

$$\begin{bmatrix} \Delta x_e \\ \Delta y_e \end{bmatrix} = \begin{bmatrix} x_e \\ y_e \end{bmatrix} - \begin{bmatrix} x_{e0} \\ y_{e0} \end{bmatrix}. \quad (39)$$

For  $K$  time delay measurements ( $K$  PBR pairs), Eq. 38 can be represented by a linear model

$$\underset{(K \times 1)}{\mathbf{Y}} = \underset{(K \times 2)}{\mathbf{H}} \underset{(2 \times 1)}{\mathbf{X}} + \underset{(K \times 1)}{\mathbf{N}}, \quad (40)$$



where

$$\mathbf{Y} = \begin{bmatrix} y_1 - h_1(\mathbf{X}_{e0}, \mathbf{X}_{tx,1}, \mathbf{X}_{rx}) \\ y_2 - h_2(\mathbf{X}_{e0}, \mathbf{X}_{tx,2}, \mathbf{X}_{rx}) \\ \vdots \\ y_K - h_K(\mathbf{X}_{e0}, \mathbf{X}_{tx,K}, \mathbf{X}_{rx}) \end{bmatrix}, \quad \mathbf{H} = \begin{bmatrix} \frac{\partial h_1}{\partial x_e} & \frac{\partial h_1}{\partial y_e} \\ \frac{\partial h_2}{\partial x_e} & \frac{\partial h_2}{\partial y_e} \\ \vdots & \vdots \\ \frac{\partial h_K}{\partial x_e} & \frac{\partial h_K}{\partial y_e} \end{bmatrix}, \quad \mathbf{X} = \begin{bmatrix} \Delta x_e \\ \Delta y_e \end{bmatrix}. \quad (41)$$

The least-squares solution  $\mathbf{X}$  that minimizes the sum of squares of difference between the measurements and the estimated function is defined as

$$\mathbf{X} = (\mathbf{H}^T \mathbf{H})^{-1} \mathbf{H}^T \mathbf{Y}, \quad (42)$$

where

$$\mathbf{X} = \begin{bmatrix} \Delta x_e \\ \Delta y_e \end{bmatrix}. \quad (43)$$

The estimated target location in the current iteration is therefore

$$\mathbf{X}_e = \mathbf{X}_{e0} + \mathbf{X}, \quad (44)$$

such that the target location estimate in the current iteration is used as the initial estimate  $\mathbf{X}_{e0}$  in the subsequent iteration.

#### D. MEASUREMENT AND LOCATION ERRORS

The theoretical root mean square (rms) error  $\partial M$  of a radar measurement  $M$  can be expressed as [33]

$$\partial M = \frac{kM}{\sqrt{2E/N_0}} = \frac{kM}{\sqrt{S/N}} \quad (45)$$

where  $k$  is a constant whose value is of the order of one,  $E$  is the received signal energy, and  $N_0$  is the noise power per unit bandwidth.

For time-delay (range) measurements,  $k$  depends on the shape of the frequency spectrum  $S(f)$ , and  $M$  is the rise time of the pulse. For angle measurements,  $k$  depends on the shape of the aperture illumination  $A(x)$ , and  $M$  is the beamwidth.

## 1. Time Delay (Range) Measurements

The theoretical rms error in time delay measurements  $\partial T_R$  for a rectangular pulse with pulsewidth  $\tau$  and limited by bandwidth  $B$  is approximately [34]

$$\partial T_R \approx \left( \frac{\tau}{4BE / N_0} \right)^{1/2}, \quad (46)$$

and can be expressed as a function of SNR:

$$\partial T_R \approx \frac{1}{B\sqrt{S/N}}. \quad (47)$$

This assumes  $B\tau \gg 1$ , which is not always satisfied. A more accurate model is a quasi-rectangular pulse ( $B\tau \approx 1$ ) for which [33]

$$\partial T_R \approx \frac{\tau}{2.1\sqrt{S/N}}. \quad (48)$$

## 2. Angle Measurements

The theoretical rms error of AOA measurements  $\partial \theta_R$  for an antenna with uniform (rectangular) amplitude illumination across the aperture is [33]

$$\partial \theta_R = \frac{\sqrt{3}\lambda}{\pi D (2E / N_0)^{1/2}} = \frac{0.628\theta_B}{(2E / N_0)^{1/2}}, \quad (49)$$

and can be expressed as a function of SNR:

$$\partial \theta_R = \frac{0.628\theta_B}{\sqrt{S/N}}, \quad (50)$$

$$\theta_B = \frac{0.88\lambda}{D} \quad (51)$$

where  $D$  is the antenna dimension and  $\theta_B$  is the half-power beamwidth.

### 3. Transmitter and Receiver Position Accuracy

Transmitter positions on merchant ships are updated by differential GPS (DGPS) systems and made available to surrounding vessels by onboard AIS units. There are two types of AIS transceivers [4]:

1. Class A onboard commercial vessels
2. Class B, used by leisure and smaller crafts

For the purpose of this thesis, merchant ships are assumed to be equipped with Class A AIS that broadcasts the vessel's unique identification, position, course, and speed information every 2 to 10 seconds while underway, and every three minutes while at anchor at a power level of 12.5 W [30].

Receiver positions on warships are also provided by onboard DGPS systems. In this thesis, the U.S. Coast Guard's (USCG's) DGPS service accuracy of 2 distance-root-mean-square (drms) [35] is used to model transmitter and receiver position accuracies.

### 4. Receiver-to-Target Range Error

As explained in Section C.1, the receiver-to-target range  $R_R$  is calculated from the range sum  $(R_T + R_R)$ , receiver look angle  $\theta_R$ , and baseline  $L$  measurements. Assume that the measurement errors associated with range sum  $(R_T + R_R)$ , receiver look angle  $\theta_R$ , and baseline  $L$  are uncorrelated, zero-mean random processes having Gaussian distribution with standard deviation equal to measurement rms error. The geometry dependent root-sum-squared (rss) error of  $R_R$  corresponding to Eq. 19 is expressed as [2]

$$dR_R = \left\{ \left[ \frac{\partial R_R}{\partial (R_T + R_R)} d(R_T + R_R) \right]^2 + \left( \frac{\partial R_R}{\partial L} dL \right)^2 + \left( \frac{\partial R_R}{\partial \theta_R} d\theta_R \right)^2 \right\}, \quad (52)$$

where  $d(R_T + R_R)$ ,  $dL$  and  $d\theta_R$  are the rms errors for  $(R_T + R_R)$ ,  $L$ , and  $\theta_R$ , respectively, and determined by Eq. 45.

From Eq. 52, the components of the rss error estimate of  $R_R$  can be expressed as a function of eccentricity  $e$  and receiver look angle  $\theta_R$  [2]:

$$\frac{\partial R_R}{\partial (R_T + R_R)} = \frac{1 + e^2 + 2e \sin \theta_R}{2(1 + e \sin \theta_R)^2}, \quad (53)$$

$$\frac{\partial R_R}{\partial L} = -\frac{(e^2 + 1) \sin \theta_R + 2e}{2(1 + e \sin \theta_R)^2}, \quad (54)$$

$$\frac{\partial R_R}{\partial \theta_R} = -\frac{L(1 - e^2) \cos \theta_R}{2(1 + e \sin \theta_R)^2}, \quad (55)$$

where the elliptical iso-range contour eccentricity is  $e = L/(R_T + R_R)$  and each partial derivative component defines the slope of the error surface with respect to each measurement variable.

### E. ERROR ELLIPSE PARAMETERS

The error ellipse provides a graphical means of viewing uncertainty associated with position estimates. The error ellipse is described by three parameters: (1) semi-major axis,  $a$ ; (2) semi-minor axis,  $b$ ; and (3) orientation,  $\theta$  (Figure 11).

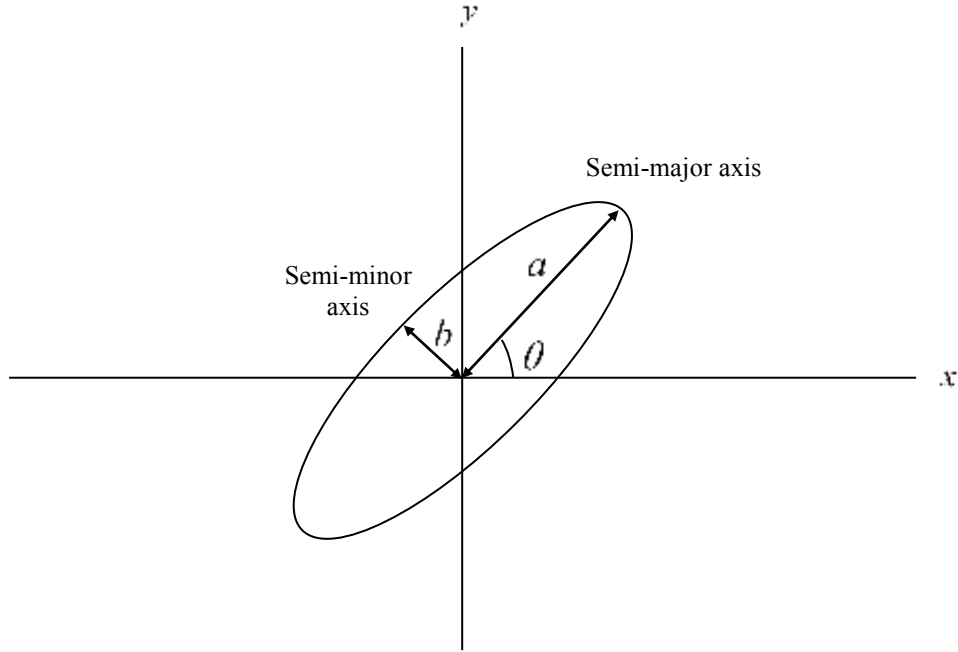


Figure 11. Error ellipse parameters.

The error ellipse parameters are described by the covariance matrix of the target's position estimate,  $\mathbf{C}_{x_e y_e}$ , given by

$$\mathbf{C}_{x_e y_e} = \begin{bmatrix} \sigma_{x_e}^2 & \rho_{x_e y_e} \sigma_{x_e} \sigma_{y_e} \\ \rho_{y_e x_e} \sigma_{y_e} \sigma_{x_e} & \sigma_{y_e}^2 \end{bmatrix}, \quad (56)$$

where  $\sigma_{x_e}^2$ ,  $\sigma_{y_e}^2$  and  $\rho_{y_e x_e}$  are the variance and correlation associated with the target's location estimate.

For the hyperbolic target location method, the target location estimate covariance matrix is expressed as

$$\mathbf{C}_{x_e y_e} = \left[ \mathbf{J}_{x_e y_e}^T \mathbf{C}_n^{-1} \mathbf{J}_{x_e y_e} \right]^{-1}, \quad (57)$$

where  $\mathbf{C}_n$  is the covariance matrix for time delay measurement errors and  $\mathbf{J}_{x_e y_e}$  is the Jacobian matrix of partial derivations in Eq. 57:

$$\mathbf{C}_n = \begin{bmatrix} \sigma_{n_1} & 0 & 0 & 0 \\ 0 & \sigma_{n_2} & 0 & 0 \\ 0 & 0 & \ddots & 0 \\ 0 & 0 & 0 & \sigma_{n_K} \end{bmatrix}, \quad (58)$$

$$\mathbf{J}_{x_e y_e} = \mathbf{H} = \begin{bmatrix} \frac{\partial h_1}{\partial x_e} & \frac{\partial h_1}{\partial y_e} \\ \frac{\partial h_2}{\partial x_e} & \frac{\partial h_2}{\partial y_e} \\ \vdots & \vdots \\ \frac{\partial h_K}{\partial x_e} & \frac{\partial h_K}{\partial y_e} \end{bmatrix}. \quad (59)$$

The semi-major axis  $a$  and semi-minor axis  $b$  are expressed as a function of elements in  $\mathbf{C}_{x_e y_e}$  as [36]

$$a = \sqrt{\frac{1}{2}(\sigma_{x_e}^2 + \sigma_{y_e}^2)} + \sqrt{\frac{1}{4}(\sigma_{x_e}^2 + \sigma_{y_e}^2)^2 + (\rho_{y_e x_e} \sigma_{y_e} \sigma_{x_e})^2}, \quad (60)$$

$$b = \sqrt{\frac{1}{2}(\sigma_{x_e}^2 + \sigma_{y_e}^2)} - \sqrt{\frac{1}{4}(\sigma_{x_e}^2 + \sigma_{y_e}^2)^2 + (\rho_{y_e x_e} \sigma_{y_e} \sigma_{x_e})^2}. \quad (61)$$

which can be further reduced to a general form

$$\left. \begin{aligned} a &= \sqrt{\chi_{2,\alpha}^2 \lambda_1} \\ b &= \sqrt{\chi_{2,\alpha}^2 \lambda_2} \end{aligned} \right\}_{\lambda_1 > \lambda_2} \quad (62)$$

where  $\chi_{2,\alpha}^2$  is the critical value of the chi-square distribution with 2 degrees of freedom and evaluated at  $\alpha$  (Figure 12).

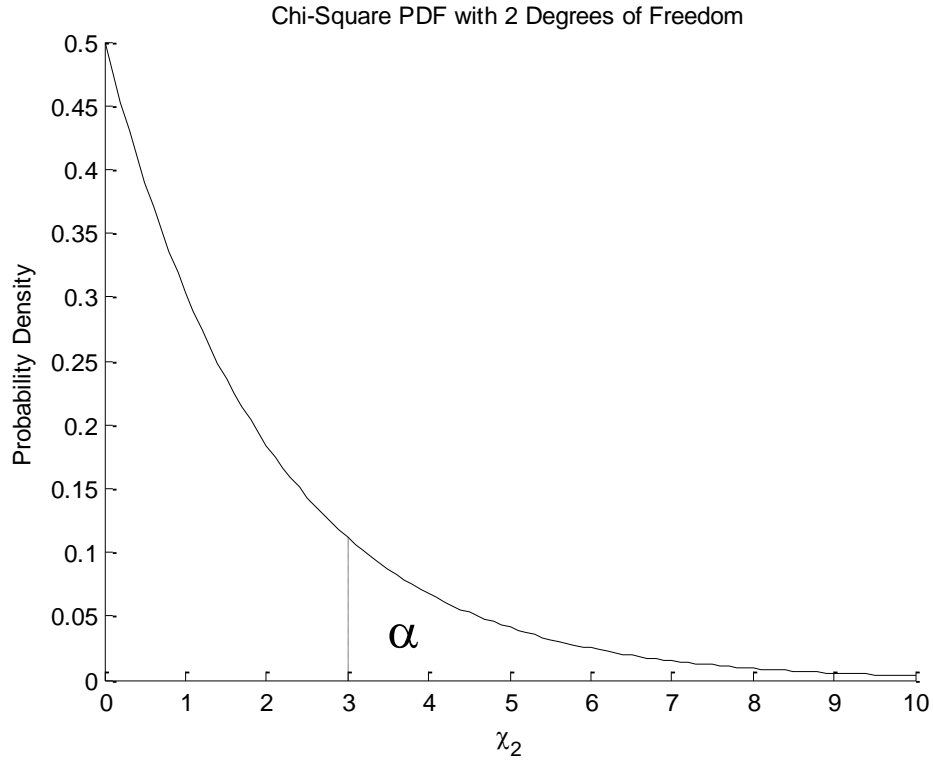


Figure 12. Chi-square probability density function with 2 degrees of freedom.  
The area to the right of  $\chi^2$  critical value is  $\alpha$ .

There are two forms of equations used to compute the orientation of the error ellipse [36, 37]:

$$\theta = \frac{1}{2} \tan^{-1} \left( \frac{2\rho_{x_e y_e} \sigma_{x_e} \sigma_{y_e}}{\sigma_{x_e}^2 - \sigma_{y_e}^2} \right) \quad (63)$$

$$\theta = \frac{1}{2} \tan^{-1} \left( \frac{\sigma_{x_e}^2 - \sigma_{y_e}^2}{2\rho_{x_e y_e} \sigma_{x_e} \sigma_{y_e}} \right), \quad (64)$$

where Eq. 63 and Eq. 64 represent clockwise and anticlockwise rotation of the error ellipse to achieve statistical independence (Figure 13).

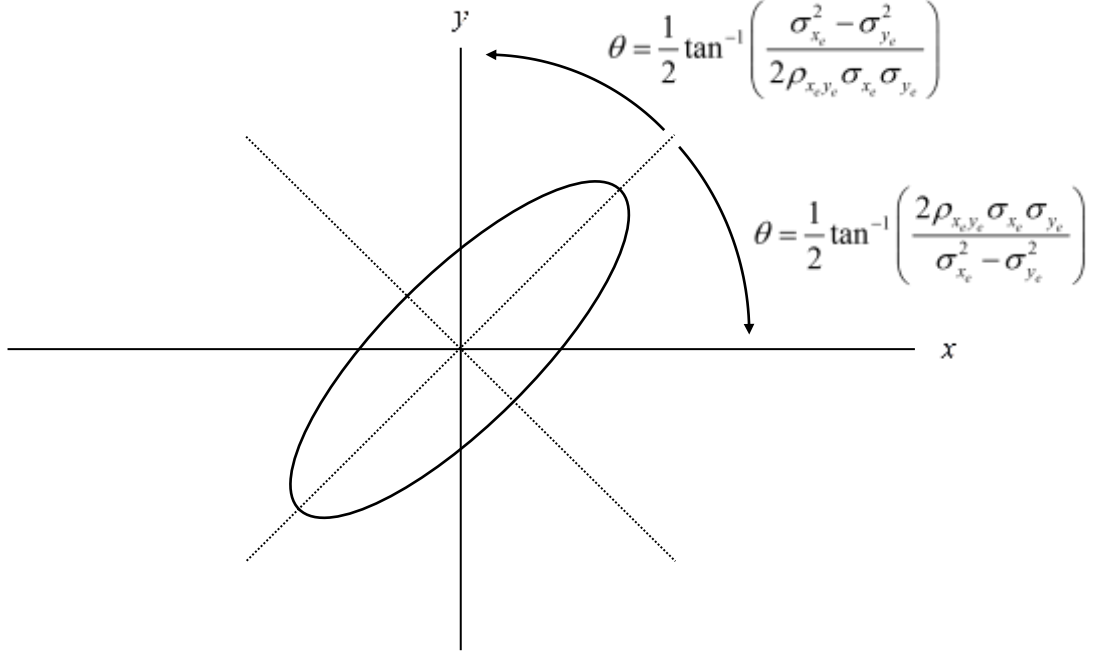


Figure 13. Error ellipse rotation to achieve statistical independence. From [38].

To understand the relationship of Monte Carlo simulations of target locations to their corresponding error ellipses, see the derivation of Eq. 62 and Eq. 63 in Appendix A.

THIS PAGE INTENTIONALLY LEFT BLANK



### III. MATLAB AND FEKO MODELING

#### A. PROBLEM SETUP

The maritime scenario with a single receiver and multiple transmitters depicted in Figure 2 will be employed in all models. The problem setup assumes a warship (receiver) equipped with broadband EW receiver and DF capability deployed to monitor maritime traffic flow at the Straits of Singapore. The targets are assumed to be low-RCS targets with infrequent transmissions and/or operating with LPI radars while civil marine radars (CMRs) on merchant ships will serve as opportunistic illuminators in PBR configuration [4]. Regulation 19 of SOLAS Chapter V requires that all merchant ships and warships carry automatic identification systems (AISs) which share information on the ships' identity, position, course, speed, navigation status, and safety-related information [30].

The target detection process starts with the warship receiving AIS transmissions from surrounding transmitters, allowing the warship to form a tactical picture with knowledge of the transmitter positions and the corresponding baseline ranges. Onboard EW and DF receivers will identify merchant ships, which will allow separation of direct and indirect (target echo) transmissions from the same CMR. The time delay between reception of the direct and indirect transmissions, DF of target echo and baseline range is used to compute the target-to-receiver range in all PBR configurations except in a forward-scattering configuration. An extension to this elliptical target location method is to define transmitter-to-target and target-to-receiver bearings for each PBR and estimate the target location by finding a "best-fit" intersection via least-squares. An alternative to the abovementioned target location method is the hyperbolic target location approach, which uses time delay measurements and knowledge of the transmitters and receiver position to estimate the target's position iteratively.

In this thesis, technical specifications from commercially available systems are used to model transmitters, EW and DF receivers. Technical specifications of UK-based Kelvin Hughes' MantaDigital Radar (see Appendix B) in the S-band and X-band are used to model the opportunistic transmitters.

For the purpose of this thesis, merchant ships are assumed to be equipped with Class A AIS that broadcasts the vessel's unique identification, position, course and speed information every 2 to 10 seconds while underway, and every 3 minutes while at anchor at a power level of 12.5 W [30]. Receiver positions on warships are also provided by onboard DGPS systems. For the simulation, the USCG's DGPS service accuracy of 2 drms [35] is used to model transmitter and receiver position accuracies.

Onboard the warship, the EW receiver would measure and extract transmission parameters, after which emitter classification and identification takes place. Integrated with the EW receiver is the DF receiver which determines the AOA of transmission signals. The EW receiver specifications used in the models are based on UK-based Teledyne Defence Limited's high performance QR026 receiver (see Appendix C). This wideband EW receiver operates from 0.5 GHz to 18 GHz and has a sensitivity of -70 dBm. The DF receiver specifications are based on South Africa's Poynting Innovations (Pty) Ltd's DF-AA0062 antenna (see Appendix D), which has coverage from 20 MHz to 6 GHz.

## **B. FEKO MODEL**

The EM simulation software FEKO was employed to model and analyze the RCS scattering properties of the maritime target. A generic frigate is chosen as the maritime target. A three-dimensional model of the frigate was created in Computer Simulation Technology (CST) Microwave Studio (MWS) in [4] and imported into FEKO where free space monostatic and bistatic RCS returns at S-Band and X-Band can be generated. Figure 14 shows the FEKO mesh model and a picture of the actual frigate on which the model is based, while Figure 15 shows the model's coordinate system. All surfaces are assumed to be perfect conductors.

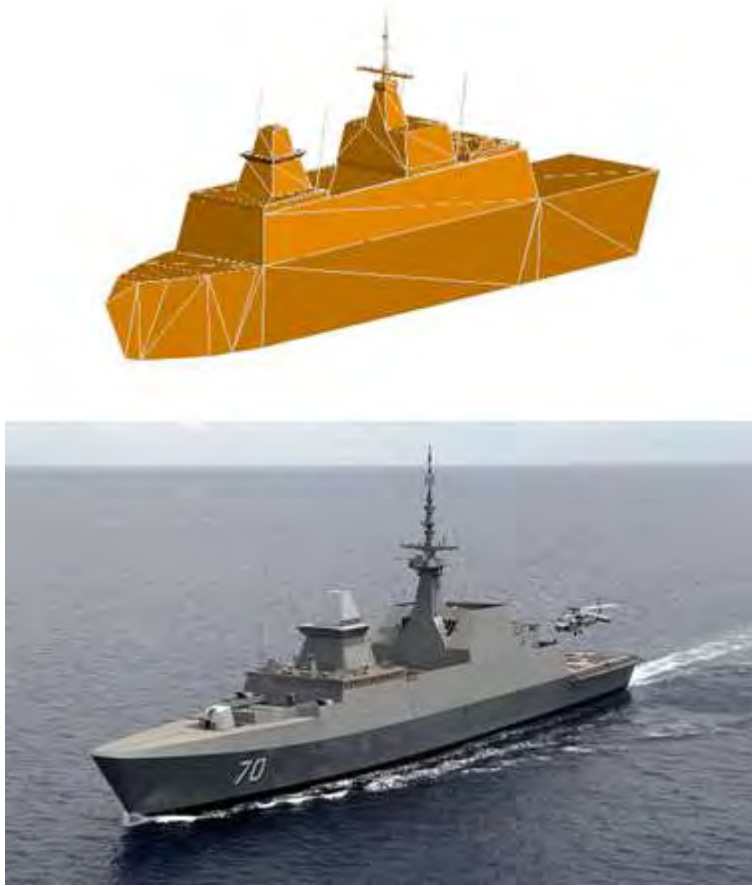


Figure 14. Frigate FEKO model (top) and actual RSN Formidable-class frigate (bottom; from [39]). Side-profile.

Figure 16 shows the frigate monostatic RCS and bistatic RCS at  $10^\circ$  incident angle at 3.05 GHz. The difference in monostatic and bistatic RCS can vary up to 70 dB for different look angles. The frigate's bistatic RCS returns vary with bistatic angle  $\beta$  and is larger than the monostatic RCS in the forward scatter direction. The PBR configuration capitalizes on this characteristic to detect low-RCS targets using opportunistic transmissions.

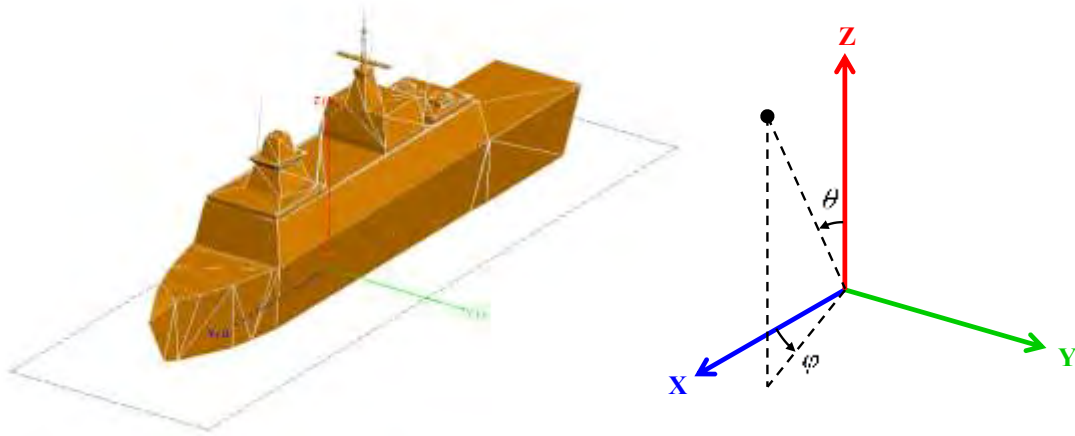


Figure 15. Frigate FEKO model and coordinate system.

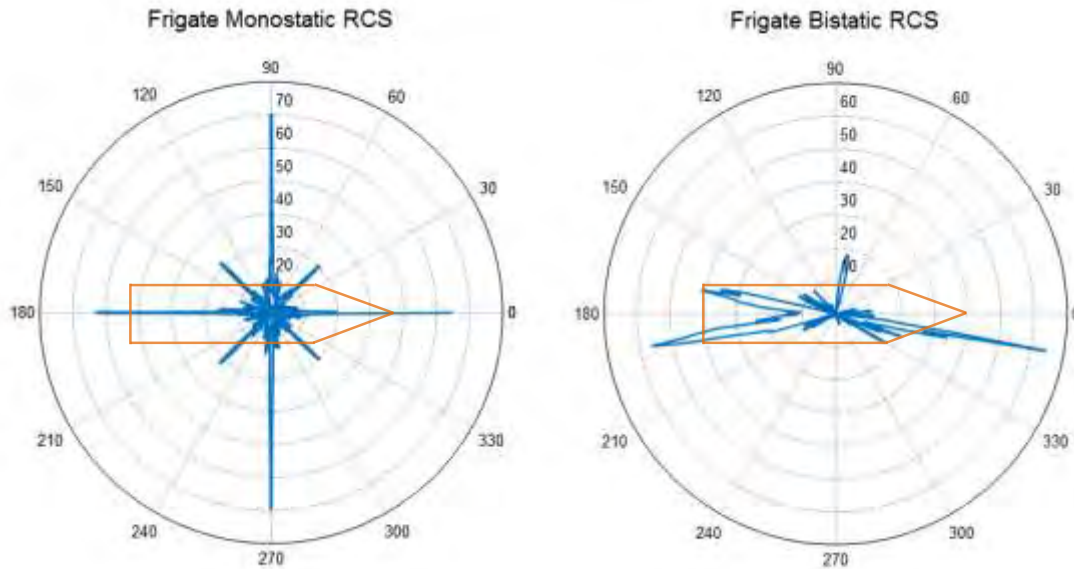


Figure 16. Frigate's monostatic RCS (dBsm) (left) and bistatic RCS (dBsm) with incident angle of  $10^\circ$  (right) at 3.05 GHz.

Figure 17 shows the frigate's bistatic RCS returns at  $1^\circ$  and  $0.1^\circ$  resolution, respectively, against the azimuth return angle. From the plots, it is evident that small variations in azimuth return angles may result in significant difference in RCS returns. Simulations using the same model in FEKO also suggest that small variations in the azimuth incident angle will result in significant variations in RCS returns. Therefore, to

ensure that accuracy of the model is maintained, it would be ideal to call FEKO to compute the exact RCS returns given the required incident and receive angles.

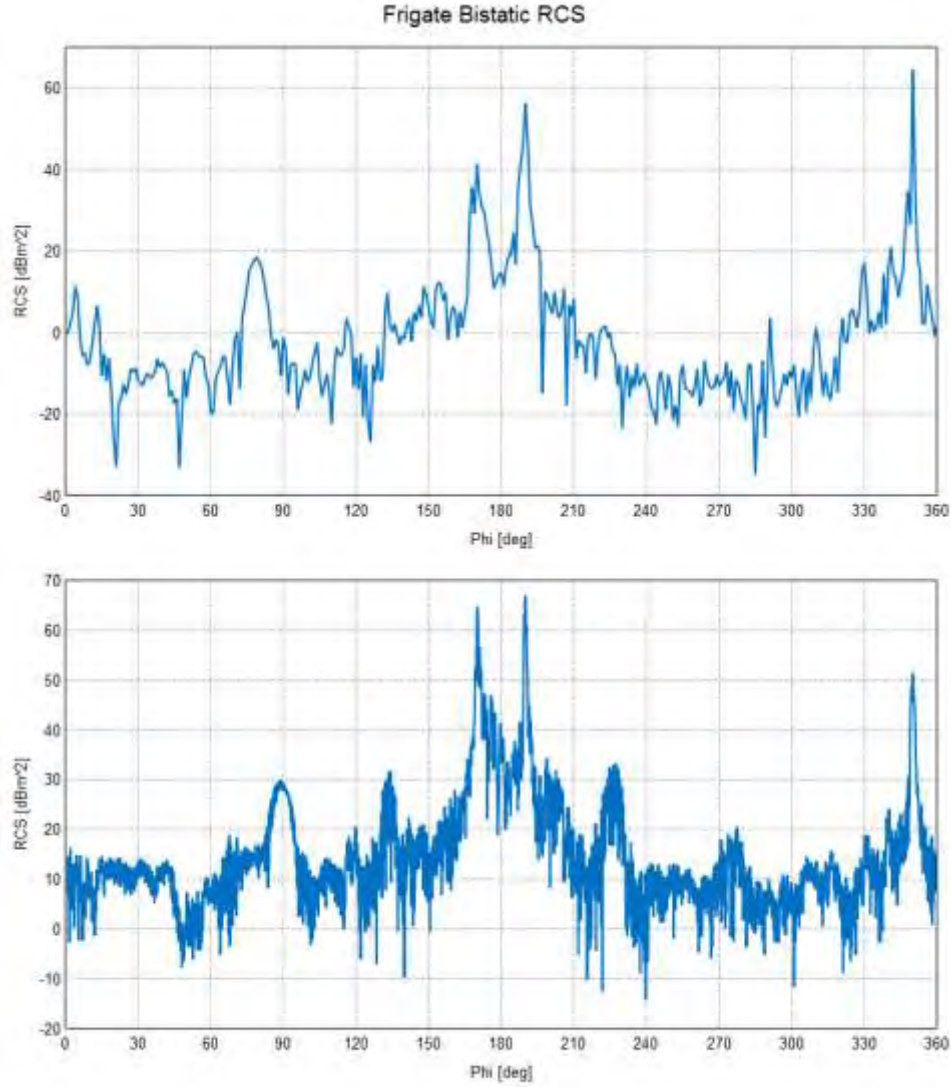


Figure 17. Frigate bistatic RCS (dBsm) with incident angle of  $10^\circ$  at 3.05 GHz.  
RCS at  $1^\circ$  resolution (left) and  $0.1^\circ$  resolution (right).

### C. MATLAB MODEL

The maritime scenario is modeled in MATLAB with the frigate target RCS from FEKO. Detection coverage and target location methods are simulated using the MATLAB models, after which the results are examined to propose optimal PBR

configurations and geometry, as well as to investigate their effects on estimated target location uncertainty.

## 1. Detection Coverage Model 1

The original MATLAB detection coverage model (*Detection Coverage Model 1*) computes the received SNR given the target's position information. This model requires the following input file and parameters to generate a detection coverage summary plot:

- Target path information in an Excel file
- Target CADFEKO model file (.cfx file)
- Target default EDITFEKO file (.pre file)
- Transmitter parameters
- Receiver parameters

The target's path information Excel sheet is of the form given in Table 3, where the model is required to execute a FEKO run for each PBR pair at each time step. The target's position and velocity vector at each time step can represent the actual target's course or it could be a grid of equally spaced arbitrary target positions. The detection coverage model generates the received SNR along the target's path for the former, and a detection coverage plot (receiver SNR are grid points) for the latter.

Table 3. Target path information format in Excel sheet.

Time	Position Vector			Velocity Vector		
$t_1$	$x_1$	$y_1$	$z_1$	$v_{x1}$	$v_{y1}$	$v_{z1}$
$t_2$	$x_2$	$y_2$	$z_2$	$v_{x2}$	$v_{y2}$	$v_{z2}$
$\vdots$	$\vdots$	$\vdots$	$\vdots$	$\vdots$	$\vdots$	$\vdots$
$t_n$	$x_n$	$y_n$	$z_n$	$v_{xn}$	$v_{yn}$	$v_{zn}$

The target's CADFEKO and EDITFEKO files are required for FEKO to model and generate the RCS returns from the target for given incident and receive angles. The CADFEKO file contains the target's mesh model while the EDITFEKO file includes execution parameters such as frequency, incident angle, and receiver angles. For each FEKO run, parameters in the EDITFEKO file are modified prior to running the FEKO

Solver function on the CADFEKO model. The RCS returns are then read from the .out file. The transmitter, EW, and DF receiver S-band and X-band parameters are based on technical specifications of commercially available systems.

Figure 18 gives an overview of Detection Coverage Model 1 for each transmitter-target-receiver pair at each time step. The entire MATLAB model and its interface with Excel and FEKO are automated. The model begins by computing the incident and receive angles at the target given the transmitter's, receiver's, and target's current positions. Given the incident and receive angles, the EDITFEKO file is modified to indicate the required signal incidence and receive angles. The FEKO solver is then executed on the target's CADFEKO model to generate an .out file containing the RCS return for the current transmitter-target-receiver geometry.

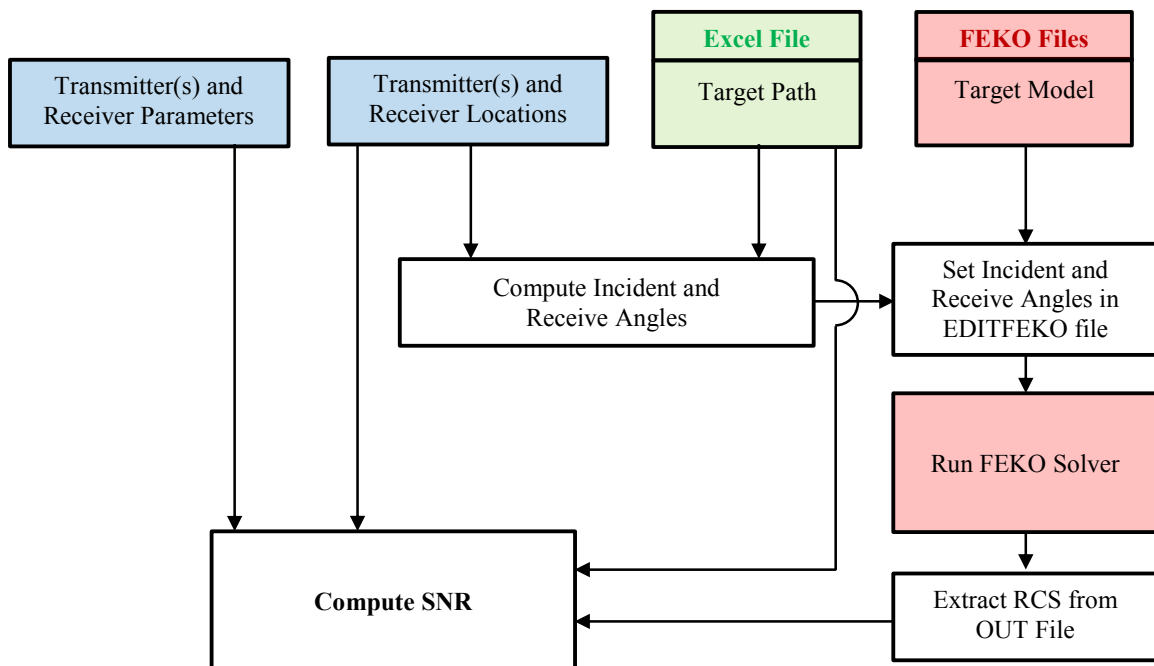


Figure 18. MATLAB Detection Coverage Model 1 flowchart.

## 2. Detection Coverage Model 2

Figure 19 gives an overview of the *Detection Coverage Model 2* for each transmitter-target-receiver pair at each time step. Unlike Model 1, Model 2 extracts RCS returns via interpolation given bistatic incident and receive angle from a pre-computed

RCS table of the form given in Table 4. This reduces the simulation duration greatly as the model does not need to execute FEKO for each angle.

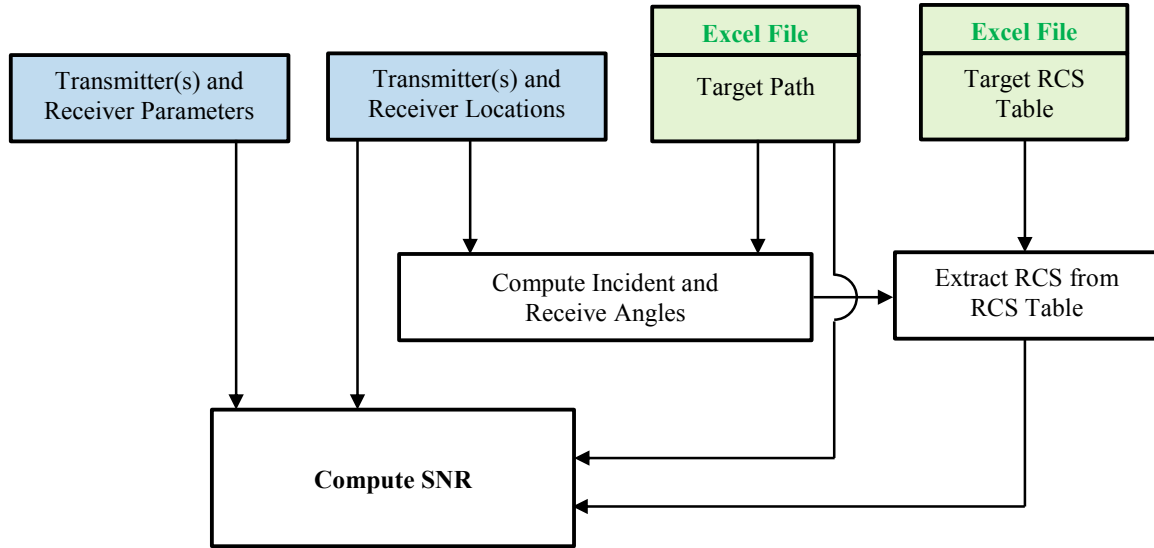


Figure 19. MATLAB Detection Coverage Model 2 flowchart

The Detection Coverage Model 2 also computes the received SNR given the target's position. This model requires the following input file and parameters to generate a detection coverage summary plot:

- Target path information in an Excel file
- Target RCS table in an Excel file
- Transmitter parameters
- Receiver parameters



Table 4. RCS table format in Excelsheet.

Incident Receive	1°	2°	...	360°
1°	RCS Values			
2°				
⋮				
360°				

The target's path information Excelsheet and RCS table would be of the form given in Table 3 and Table 4, respectively. Like Model 1, the target's position and velocity vector at each time step can either represent the actual target's course or it could be a grid of equally spaced arbitrary target positions. The detection coverage model generates the receive SNR along the target's path for the former, and a detection coverage plot (receiver SNR are grid points) for the latter. The table of RCS values for various incident and receiver bistatic angles is pre-computed in FEKO using the target's CADFEKO model. The bistatic angle resolution for the RCS table can be improved by generating a higher resolution RCS table prior to simulating detection coverage. Lastly, transmitter, EW, and DF receiver S-band and X-band parameters are based on technical specifications of commercially available systems.

### 3. Simulation Duration and Accuracy Trade-off

Preliminary simulations using Detection Coverage Model 1 presented the issue of simulation duration and accuracy trade-off. Referring to the flowchart of Model 1 in Figure 18, it takes approximately 4 seconds for FEKO to compute the RCS each time the FEKO Solver is called. The time taken is acceptable if the model is required to execute FEKO via the model only a few times. However, in generating detection coverage plots, the frigate path Excel file contains equally spaced grid points across an area of interest. In

this case, the model calls FEKO at each grid point for each PBR pair. For example, consider a  $40 \text{ km} \times 40 \text{ km}$  area with grid points spaced 1 km apart (Figure 20); there will be  $41 \times 41 = 1681$  grid points. If there is one opportunistic transmitter in the grid area, it will take approximately  $1681 \times 4 \times 1 = 6728$  seconds = 1.9 hours to generate the detection coverage for the grid area. However, if there are 8 opportunistic transmitters in the grid area, it now takes approximately  $1681 \times 4 \times 8 = 53,792$  seconds = 14.9 hours to generate the detection coverage.

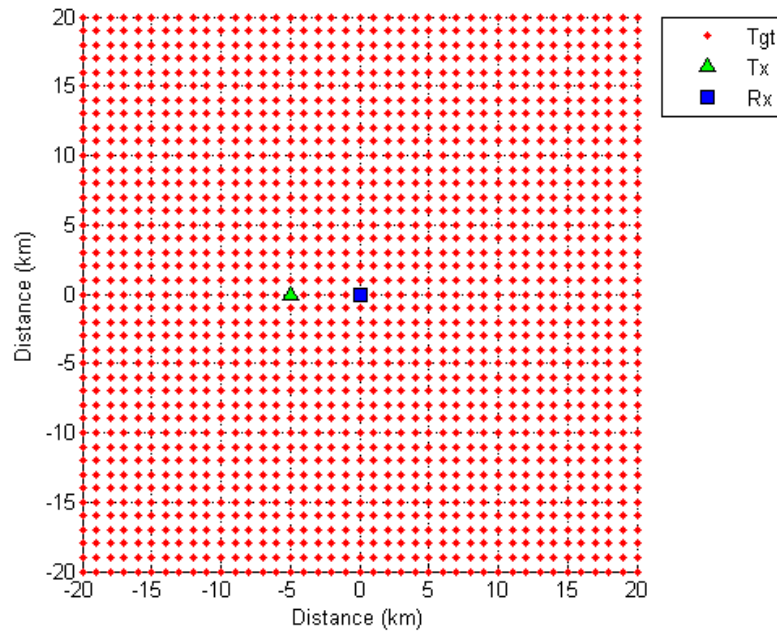


Figure 20. Detection coverage of a  $40 \text{ km} \times 40 \text{ km}$  area of interest grid points at 1 km resolution.

The large number of simulation cases, compounded with the need to simulate various grid sizes/resolutions and number of transmitters, resulted in the alternative detection coverage model (Detection Coverage Model 2).

Referring back to Figure 17, small variations in return angles may result in significant differences in RCS return; therefore, Model 2 reduces detection coverage simulation duration at the expense of accuracy due to low-RCS resolution.

Figure 21 illustrates the simulation duration and accuracy trade space for Model 1 and Model 2. Assume that the RCS table used by Model 2 has bistatic angle resolution of 1 degree and its current position in the simulation trade space is indicated in Figure 21. The accuracy of Model 2 can be improved with minimal increase in simulation duration by pre-computing RCS tables with higher resolution bistatic angles. Generating a high resolution RCS table requires longer computing duration compared to a lower resolution RCS table. However, the additional computing duration occurs one time upfront and greatly reduces the simulation duration of Detection Coverage Model 2.

In view of the constraint on computing speed, Detection Coverage Model 1 and Detection Coverage Model 2 will be generated but Model 2 will be used to simulate target detection coverage and target location performance for the rest of this thesis.

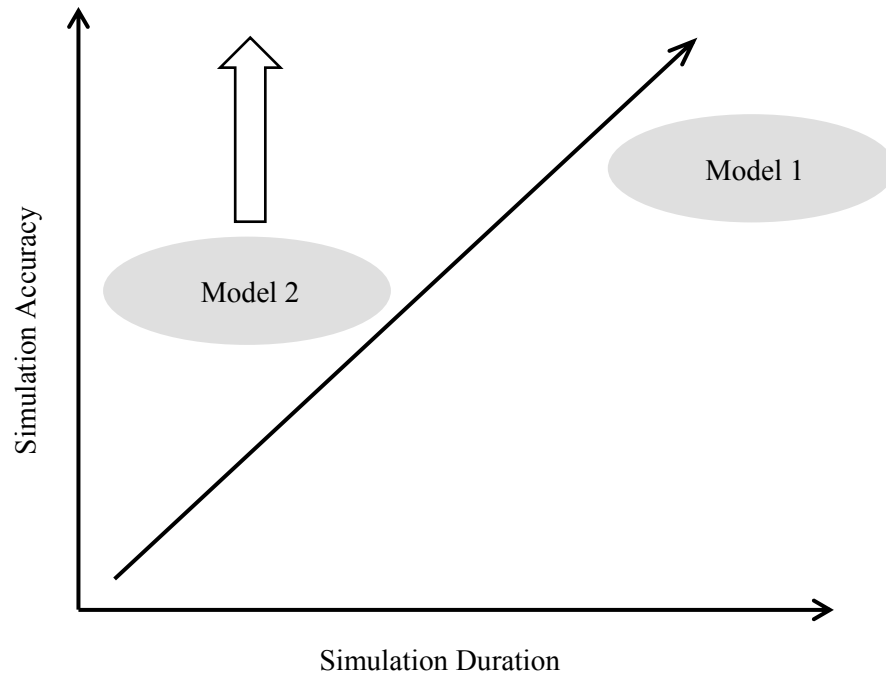


Figure 21. Simulation duration and accuracy trade space for detection coverage models.

#### 4. Target Location Model

The MATLAB target location model estimates the target's location given a set of erroneous measurements and parameters. This model requires the following input file and parameters:

- Target path information in an Excel file
- Erroneous time delay, DF measurements
- Erroneous transmitter and receiver positions

The target's path information Excel sheet would be of the form given in Table 3. The target's position and orientation are used to generate measurements and compute the SNR at the receiver, which in turn is used to model rms errors in the measurements. The theory behind modelling measurement errors is covered in Section II.D. For the hyperbolic target location method, the error ellipse associated with each position estimate is computed.

#### D. MODEL VERIFICATION

Prior to using the Detection Coverage Models to generate simulation results, it is necessary to verify the model against bistatic radar principles and/or using simple targets. Here, the detection coverage models were verified using the following approaches:

- Target with constant RCS
- Target plane at various orientations

According to Eq. 2 and Eq. 3 the SNR of the target echo depends on transmitter parameters, receiver parameters, target RCS  $\sigma_B$ , transmitter-to-target range  $R_T$ , and target-to-receiver range  $R_R$ . When transmitter parameters, receiver parameters, and target RCS are kept constant, the SNR depends solely on  $R_T$  and  $R_R$ . For each pair of constant  $R_T$  and  $R_R$  ranges, the contour of constant SNR traces out an oval of Cassini, as covered in Section II.B.

To verify that the Detection Coverage Models satisfy bistatic radar principles, consider a target whose RCS is constant regardless of aspect angle or range. The resultant detection coverage should exhibit elliptical SNR contours, as depicted in Figure 5. The

detection coverage and contour plot generated from the Detection Coverage Models is shown in Figure 22. The results agree with bistatic radar theory such that the SNR contour values satisfy Eq.2.

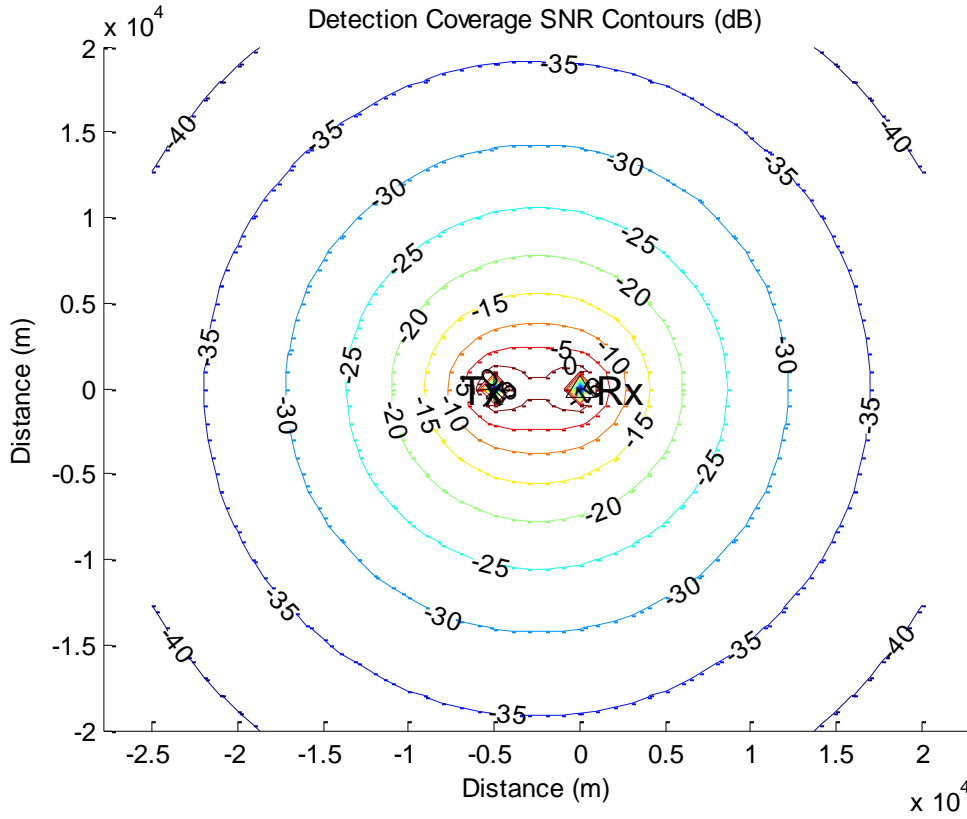


Figure 22. Detection coverage contours for constant RCS target.

Apart from verifying the model against bistatic radar principles, it was tested using a simple plate target at various orientations. The FEKO model of the target plate used is shown in Figure 23. Figure 24 shows the S-band RCS for the target plane where the angle represents the angle  $\phi$  from the  $x$ -axis horizontal in the  $xy$ -plane ( $\theta = 90^\circ$ ) of the FEKO model.

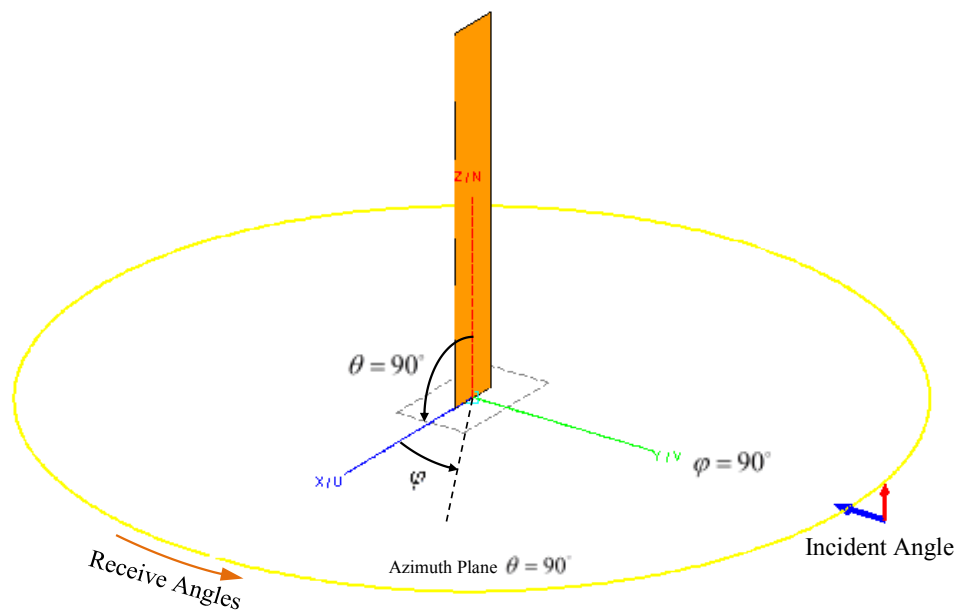


Figure 23. Target plate FEKO model.

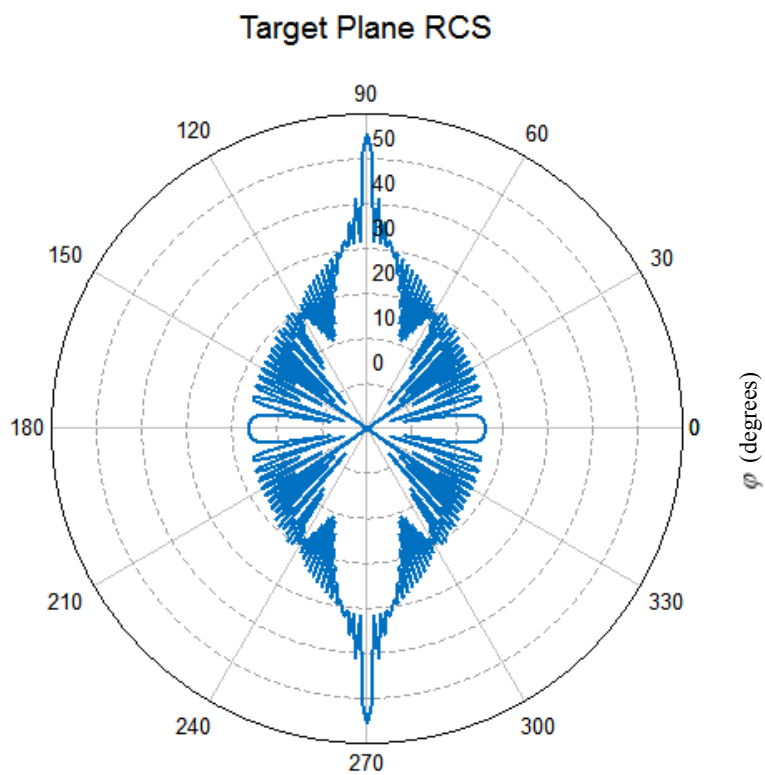


Figure 24. Target plate S-Band azimuth RCS (dBsm) at  $\varphi=90^\circ$  incidence.

To verify that the MATLAB Detection Coverage Model is sound for various target orientations, detection coverage plots for the target plate are generated at several rotations of the plate around the  $z$ -axis. From the plate's RCS in Figure 24, one would expect higher RCS and hence SNR at the faces of the plate, that is, at  $90^\circ$  and  $270^\circ$ . In addition, as the plate's RCS returns exhibit symmetry about a certain axis, the detection coverage plots at selected target orientations demonstrate symmetrical characteristics. See Appendix E for the target plate detection coverage plots and discussion of its RCS.

The elliptical and hyperbolic target location methods outlined in Section II.C were verified using measurements in the absence of errors. Using error-free measurements, estimated target locations have zero errors for both target location methods.

The hyperbolic target location's associated error ellipse semi-major length, semi-minor length, and orientation are verified against Monte Carlo simulations. For example, it was verified that approximately 90% of the Monte Carlo estimates fall within a 90% confidence ellipse.

THIS PAGE INTENTIONALLY LEFT BLANK



## IV. SIMULATION RESULTS

In this chapter, the detection coverage for various PBR transmitter-target-receiver geometries is examined using Detection Coverage Model 2, and PBR configurations and geometry for optimal detection coverage are proposed. The results for elliptical and hyperbolic target location methods and their corresponding uncertainty ellipses are presented. This chapter begins by investigating how the number of opportunistic transmitters, their ranges, and geometry relative to the target and receiver affects detection coverage in an area of interest. Detection results from Detection Coverage Model 1 and Model 2 along the target's arbitrary path are also presented. Target location results from elliptical and hyperbolic target location methods are then presented with their corresponding error ellipse. The effects of transmitter-target-receiver geometry on each target location method's spatial error distribution are explored. All simulation plots and results are included in Appendices F through H.

### A. DETECTION COVERAGE

#### 1. Bistatic RCS

To better understand the detection coverage plots of the PBR scenario presented in this section, consider the bistatic RCS of the target (Figure 14) with incident angle  $10^\circ$  at 3.05 GHz and 9.41 GHz in Figure 25. The frigate's bistatic RCS returns vary with the incident and receive angles with peaks occurring at certain return angles. Overall, they have similar return patterns in S-band and X-band. It is also observed that RCS will have a peak in the forward-scattering look angle.

Detection coverage plot results in this section are obtained using Detection Coverage Model 2 with a RCS table of  $1^\circ$  angle resolution. The RCS values from the pre-computed table are extracted by interpolation if incident and/or receive angles are not integers. Each point  $(x, y)$  on the detection coverage plot represents the total received SNR at the receiver when the target is at position  $(x, y)$ . The colour at each point indicates the value of total SNR at the receiver.

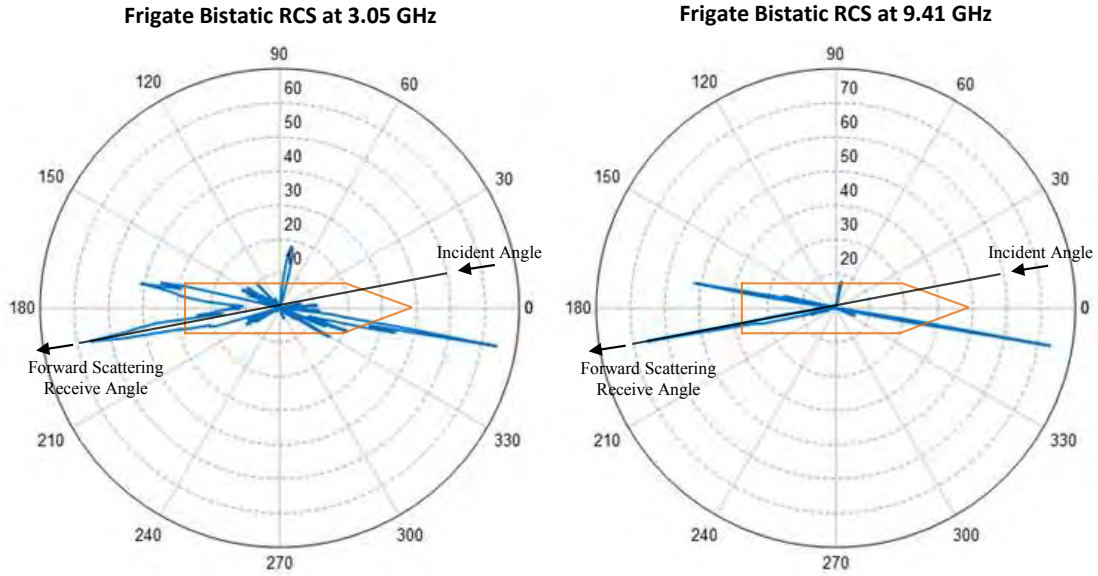


Figure 25. Target bistatic RCS (dBsm) with incident angle  $10^\circ$  at 3.0 GHz (left) and 9.41 GHz.

## 2. General Observations

Referring to the detection coverage results (see Appendix F), the SNR of a target echo at the receiver strongly depends on the bistatic RCS characteristic of the target. Higher SNR will always be observed when the target-to-receiver LOS lays in the peak of the target's bistatic RCS returns. Since the target's bistatic RCS exhibits high RCS returns in the forward-scattering look angle (Figure 25), a PBR with the transmitter-target-receiver in the forward-scattering configuration results in the best detection at the receiver for a fixed range. It is also evident from the detection coverage results that transmitter-target-receiver in the back-scattering configuration would result in good detection with target echo SNR decreasing as the target's range to receiver increases. Figure 26 highlights target positions in the forward and back-scattering configuration on a detection coverage plot where the transmitter is positioned at  $(-5000, 0)$  and receiver at  $(0, 0)$ .

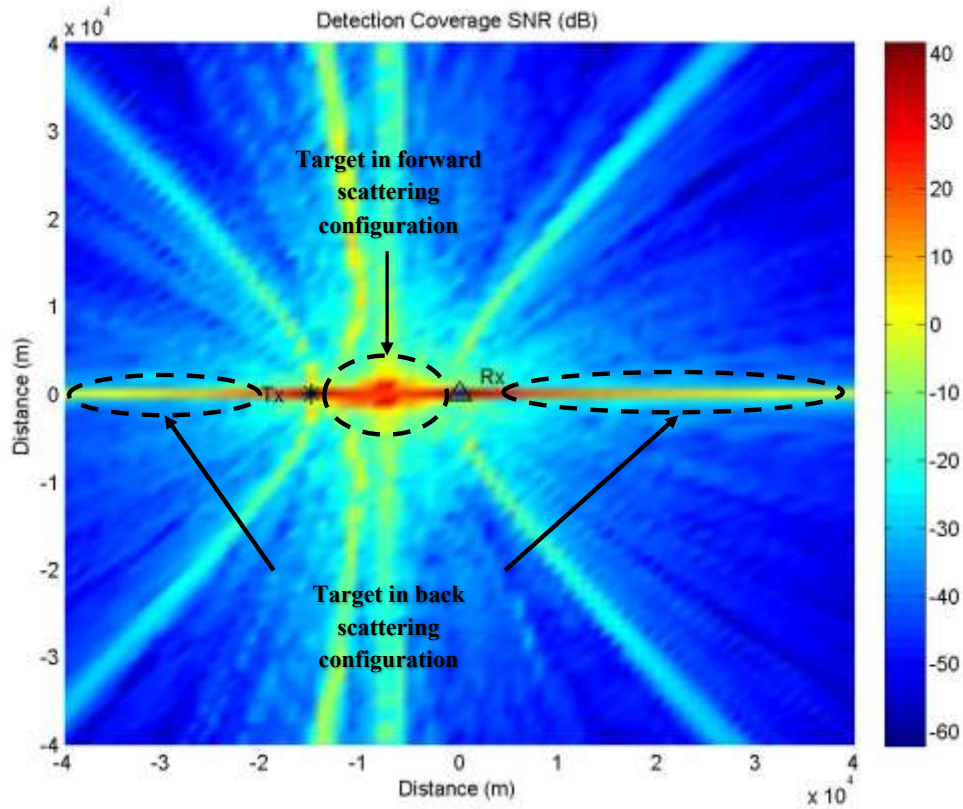


Figure 26. Target positions in forward-scattering and back-scattering configuration on detection coverage plot.

From the detection coverage results (see Appendix E), it was observed that target echo SNR is generally high when the target is within the “net” of transmitters-receiver configuration with the highest SNR occurring when the PBR is in the forward-scattering configuration. This observation agrees with the findings in [4] which state that the optimal transmitters-receiver constellation is to have transmitters at every quadrant with respect to the receiver. Outside the “net” of transmitters-receiver, detection is usually better when the PBR is in the back-scattering configuration. Across all PBR geometries, detection gaps—areas with the low target echo SNR at the receiver—occur when the target is outside the transmitter-receiver cluster or away from bearings extending from the transmitter-receiver baselines (Figure 27).

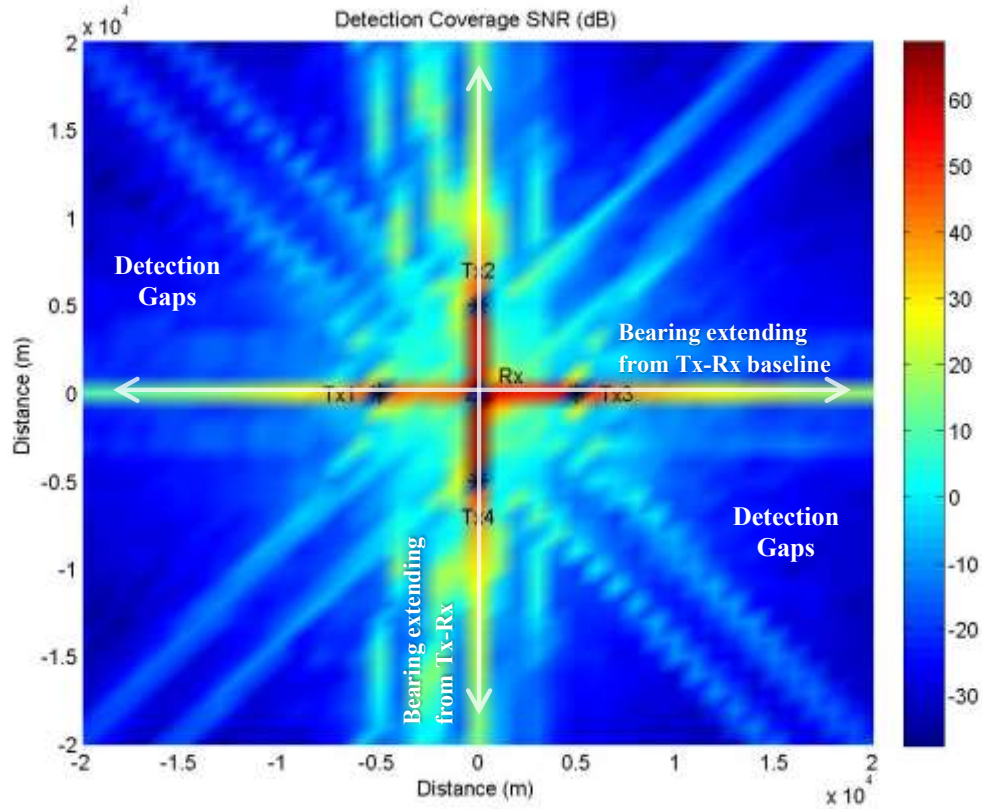


Figure 27. Detection gaps and bearings extending from Tx-Rx baseline in detection coverage plot.

### 3. Vary Number of Transmitters

The number of available opportunistic transmitters affects the detection coverage area and strength of the target echo at the receiver. Figure 28 shows that overall detection coverage improves as the number of opportunistic transmitters increases. The result presented in this thesis assumes that target echo is received from all transmitters shown in the detection coverage plot. The percentage of grid points with received SNR greater than 10 dB within a 10 km radius from the receiver for a different number of transmitters around the receiver is given in Table 5 and 0. For a target orientation of  $0^\circ$ , detection coverage increases from 17.0% to 61.6% as the number of opportunistic transmitters increase from one to eight (Table 5).

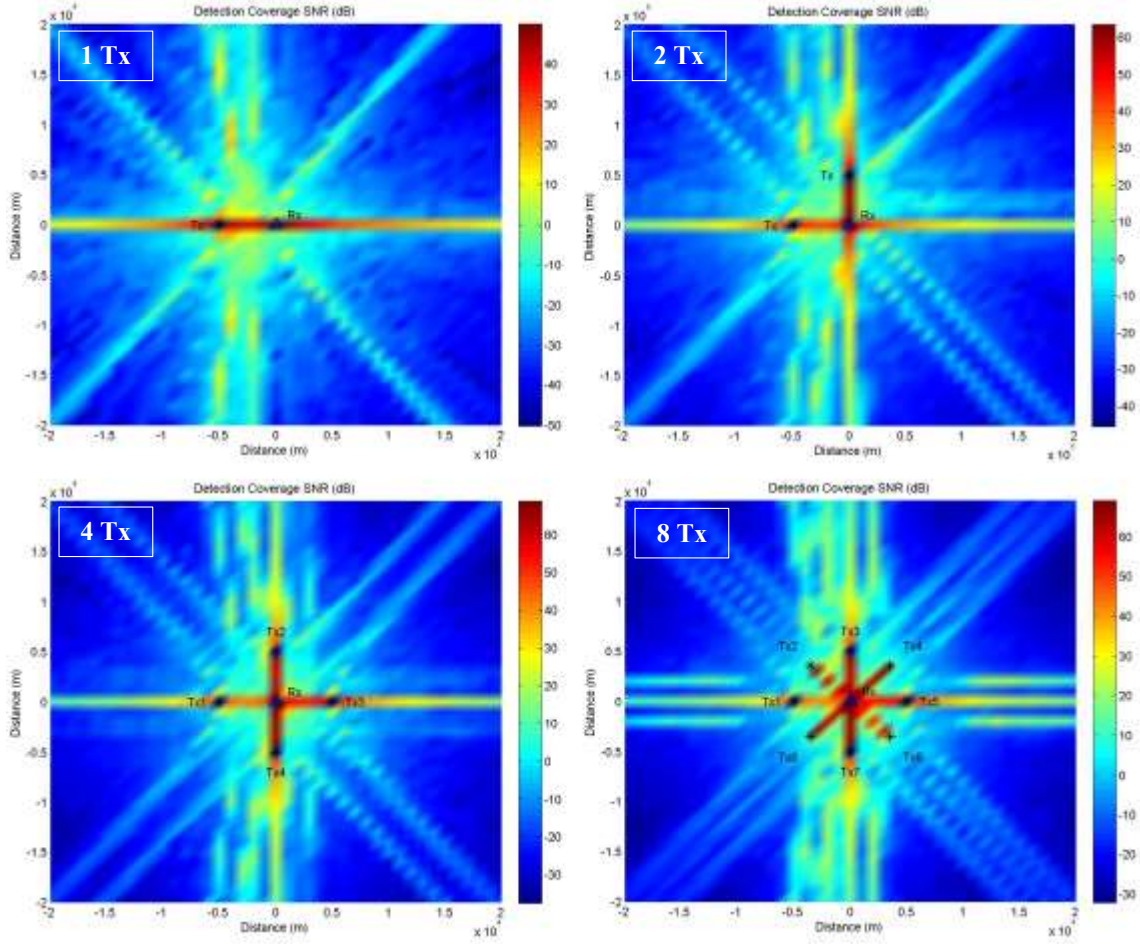


Figure 28. Detection coverage plots at S-Band for with target plate at  $0^\circ$  orientation as the number of transmitters varies.

The detection statistics presented in Table 5 and 0 suggest that S-band opportunistic transmitters result in better detection than X-band opportunistic transmitters. This is attributed to the variation in RCS returns in X-band compared to S-band. Referring to Figure 25, peak RCS at X-Band is higher, but narrow lobes result in low probability of intercepting a lobe. Nevertheless, detection coverage patterns are consistent between S-band and X-band transmissions. As the difference in detection coverage is not significant in detection coverage plots, subsequent sections of this thesis are focused on results from S-band transmissions.

Table 5. Percentage of grid points with SNR greater than 10 dB within a 10 km radius centered at the receiver. Target orientation at 0°.

<b>Target at 0° orientation</b>		
# of Tx	% SNR > 10 dB in 10 km radius	
	<b>S-Band</b>	<b>X-Band</b>
1	17.0%	15.1%
2	33.8%	29.5%
3	42.0%	36.4%
4	47.5%	40.3%
8	61.6%	54.8%

Table 6. Percentage of grid points with SNR greater than 10 dB within a 10 km radius centered at the receiver. Target orientation at -90°.

<b>Target at -90° orientation</b>		
# of Tx	% SNR > 10 dB in 10 km radius	
	<b>S-Band</b>	<b>X-Band</b>
1	16.4%	15.7%
2	33.4%	29.5%
3	40.0%	35.4%
4	47.5%	40.3%
8	61.6%	54.8%

#### 4. Vary Transmitter Range

The transmitter to receiver range determines the size of the transmitter-receiver “net” and forward-scattering area. Detection coverage plots in Figure 29 suggest that the area of detection coverage increases as the transmitter to receiver ranges increase; however, the highest target echo SNR in the grid decreases with increase in range. This observation is consistent with the findings in [40] with regards to sensitivity dependency on transmitter range and transmitter-receiver geometry. The percentage of grid points with received SNR greater than 10 dB within a 20 km radius from the receiver-transmitter range of 5 km, 10 km, and 15 km are listed in Table 7. For target orientation



of  $0^\circ$ , detection coverage increases as the transmitter to receiver range increases from 5 km to 10 km. However, the detection coverage decreases when the range further increases to 15 km unless more than four transmitters are present.

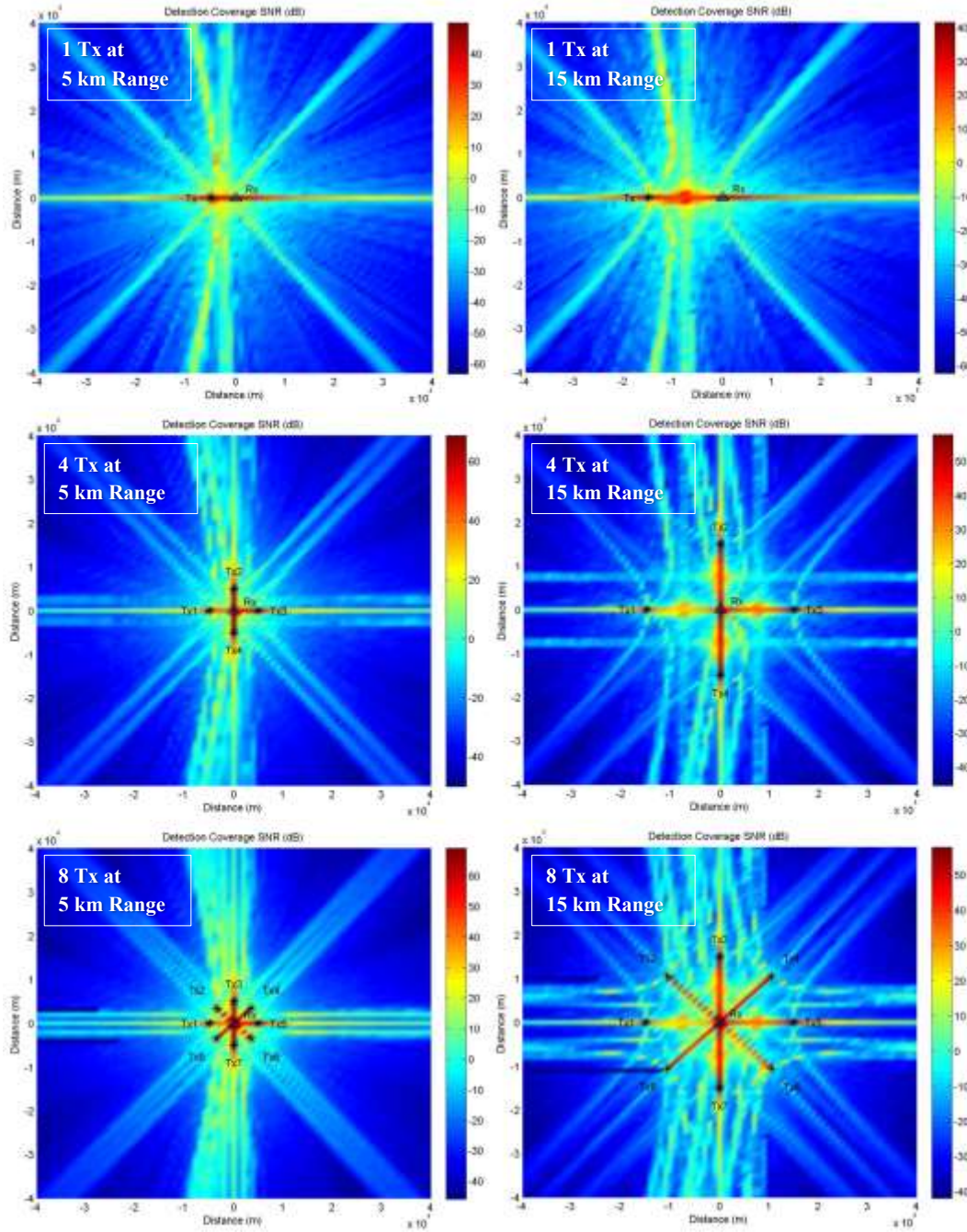


Figure 29. Detection coverage plots at S-Band with target plate at  $0^\circ$  orientation as the transmitter range to receiver increases.

Table 7. Percentage of grid points with SNR greater than 10 dB within a 20 km radius centered at the receiver. Target orientation at 0°.

		% SNR > 10 dB in 20 km radius		
# of Tx	Tx-Rx Range	5 km	10 km	15 km
1		7.3%	8.7%	5.9%
2		14.4%	17.3%	12.7%
4		19.7%	28.8%	19.9%
8		31.2%	37.1%	38.0%

## 5. Vary Transmitter-Target-Receiver Geometry

Two types of transmitter-target-receiver geometries were explored: (1) receiver-centered geometry, as seen in Figure 30, and (2) transmitter-clustered geometry, as seen in Figure 31. In a receiver-centered geometry, all observations made earlier in this chapter hold. High target SNR is received when the target is in the transmitter-receiver “net” with the best detection occurring when the transmitter-target-receiver is in the forward-scattering configuration. Outside the transmitter-receiver “net,” detection is the best when the transmitter-target-receiver is in the back-scattering configuration. Apart from areas that satisfy a back-scattering configuration, it is observed that there are additional areas that exhibit good detection coverage as a result of the target’s bistatic RCS patterns. Multiple PBR capitalizes on this to allow detection of low-RCS targets.

In a transmitter-clustered geometry, good detection is experienced when the target lies in the cluster of transmitters or in the beam extending from the receiver to the cluster of transmitters. Outside the transmitter-receiver cluster, detection is slightly better at areas that satisfy back-scattering configuration and “lines” that are shaped like a hyperbolic curve—hyperbolic contours are typical of time difference of arrival (TDOA) measurements [37]. However, for a four opportunistic transmitter’s scenario, the received target’s echo is still below 10 dB outside the transmitter-receiver cluster.



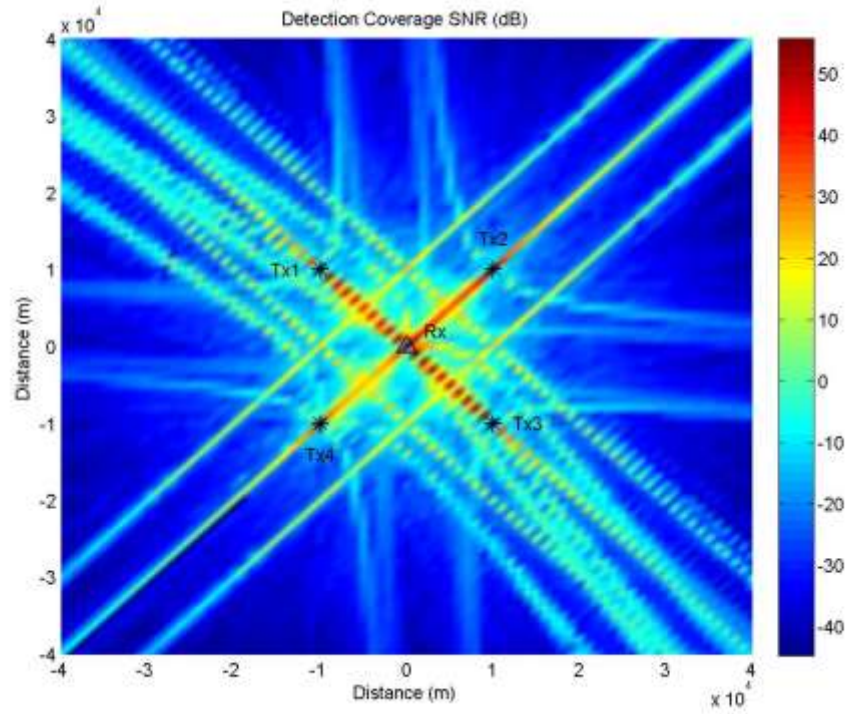


Figure 30. Detection coverage at S-Band for 4 Tx in receiver-centered geometry and target plate at  $30^\circ$  orientation.

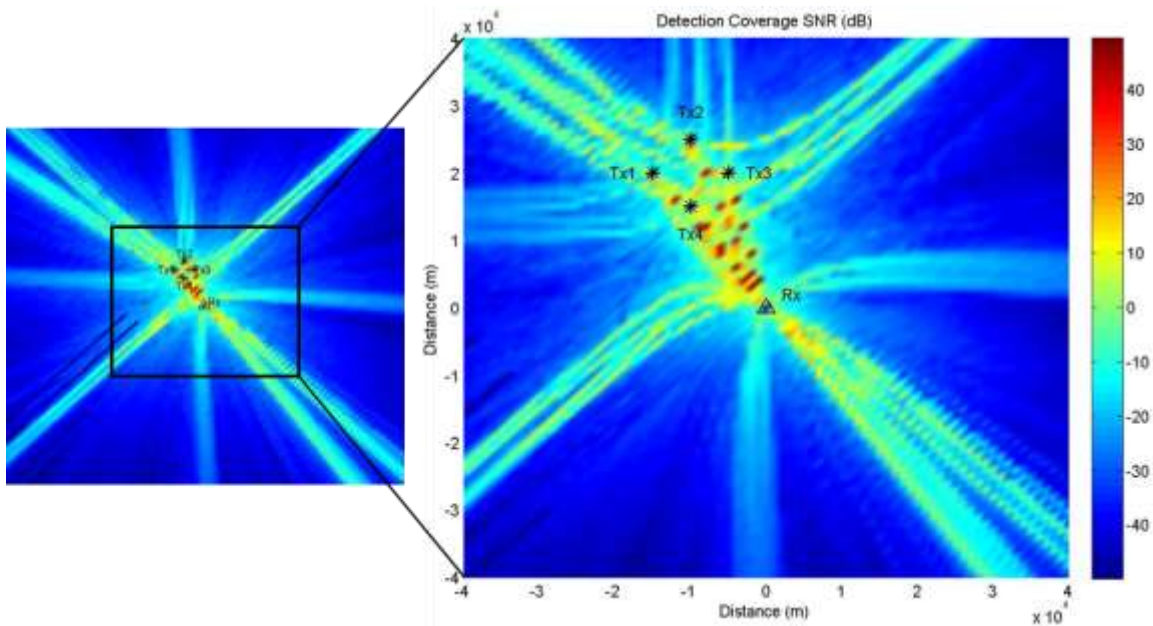


Figure 31. Detection coverage at S-Band for 4 Tx in transmitter-clustered geometry and target plate at  $30^\circ$  orientation.

Up to this point, all transmitters in a scenario were placed in a predictable fashion within an area of interest. The next series of detection coverage plots randomly positions 20 transmitters at a range of 5 to 20 km from the receiver. Earlier observations in regard to areas of good detection coverage are evident in the detection coverage plots. However, strips of detection gaps—positions with the lowest target echo SNR at the receiver—are evident in Figure 32, Figure 33, and Figure 34.

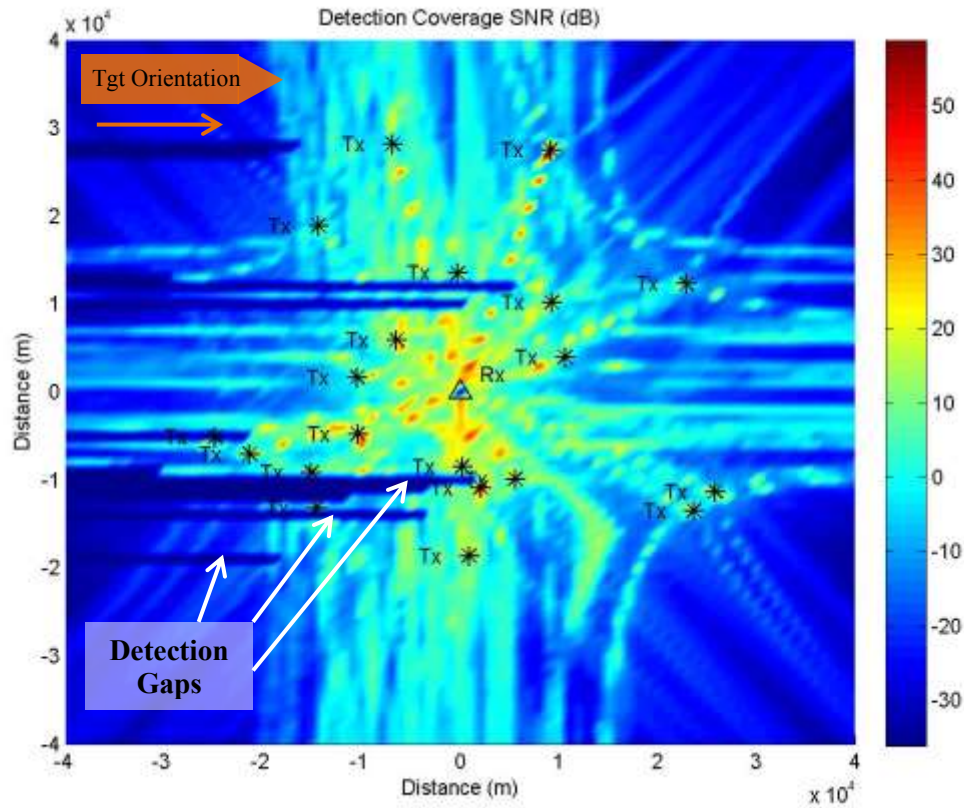


Figure 32. Detection coverage at S-Band for 20 Tx randomly positioned around Rx at 5–30 km range and target plate at 0° orientation.

The direction and location of the detection gaps are determined by the target's velocity vector and hence its orientation. Referring to Figure 32 where the target velocity vector is horizontal and points to the right and, hence, the target orientation is 0° across all grid points, detection gaps will present themselves as horizontal strips. Applying this

explanation for target orientations of  $-90^\circ$  and  $45^\circ$ , detection strips would be vertical and angled at  $45^\circ$ , respectively (Figure 33 and Figure 34). The strips of detection gaps are observed to be present when the target's heading is towards the transmitters-receiver cluster.

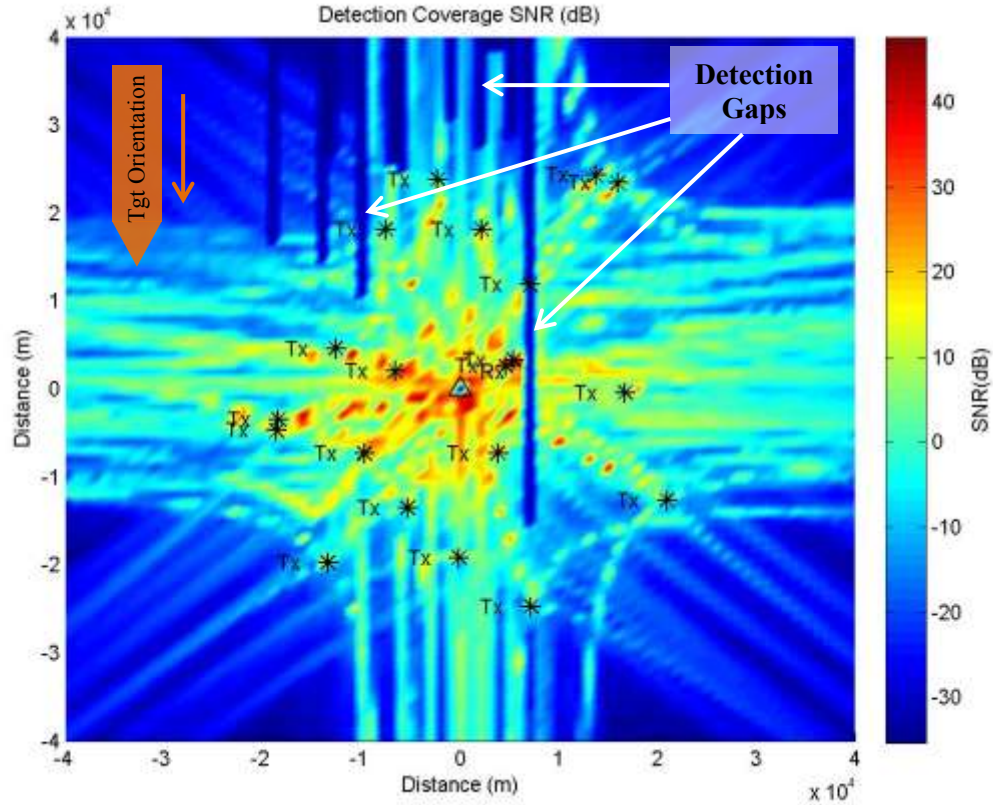


Figure 33. Detection coverage at S-Band for 20 Tx randomly positioned around Rx at 5–30 km range and target plate at  $-90^\circ$  orientation.



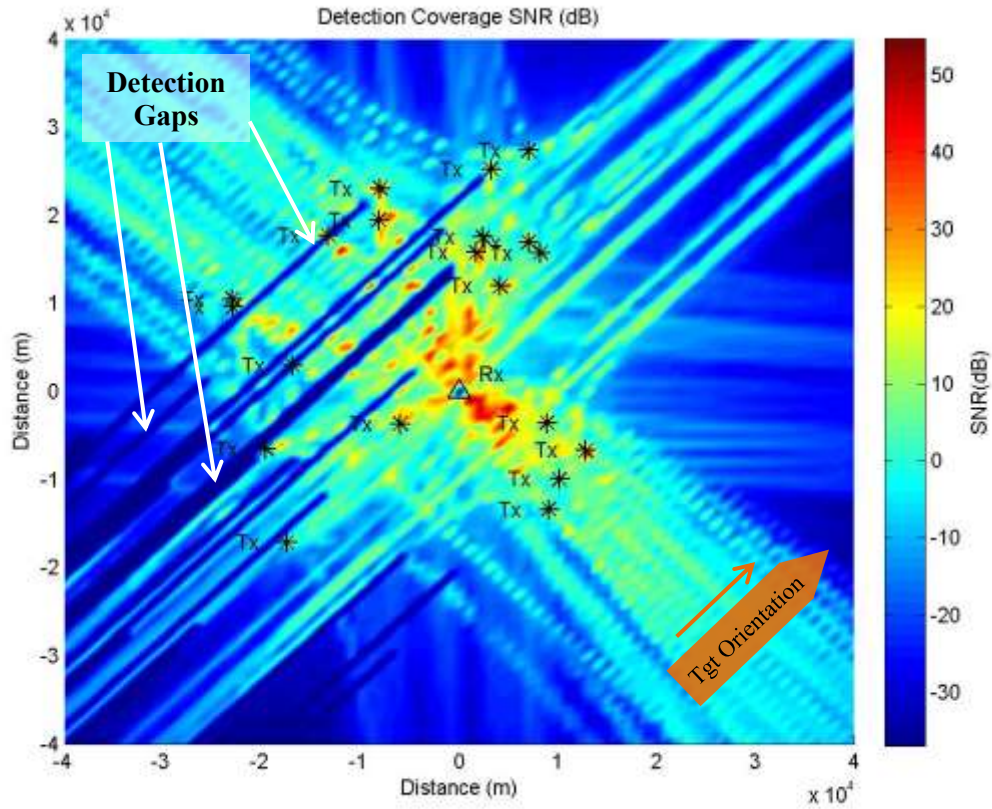


Figure 34. Detection coverage at S-Band for 20 Tx randomly positioned around Rx at 5–30 km range and target plate at 45° orientation.

## 6. Target Path Detection

Detection Coverage Model 1 and Model 2 compute detection performance given the target's path, with Model 1 using more accurate RCS values from FEKO and Model 2 extracting RCS values from a pre-computed table given bistatic incident and receive angles. The trade-off between accuracy and simulation duration illustrated in Section III.C.3 limits the use of Model 1 as a tool to study detection performance. Nevertheless, target path detection performance results from both models are included in Appendix G.

Five arbitrary target paths in Figure 35 are used to generate target path detection performance as the target moves through the area of interest. The received target echo SNR as the target transverses through the area of interest is given in Figure 36. The detection performance results here align with previous observations, where detection

coverage is good within the transmitters-receiver cluster and in the back-scattering configuration outside the transmitter-receiver cluster.

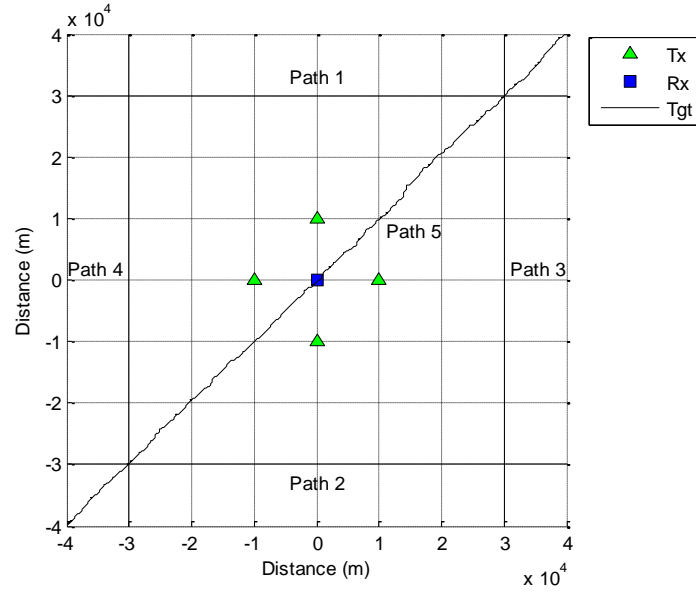


Figure 35. Five target paths used to generate target path detection performance results.

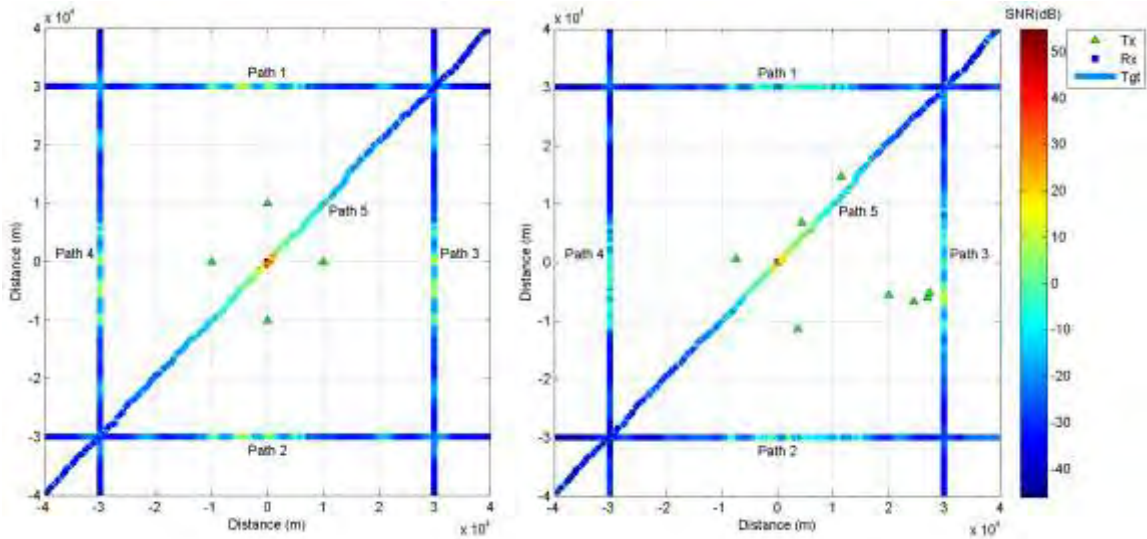


Figure 36. Detection coverage along target's path at S-Band for 4 Tx (left) and 20 Tx (right). RCS extracted from pre-computed RCS table.

## B. TARGET LOCATION ESTIMATION

### 1. General Observations

To examine target location estimation accuracy for elliptical and hyperbolic target location methods, results from both methods are presented in target location error color plots and estimated target location scatter plots. In a target location error plot, the color at each point  $(x, y)$  represents the error in location estimate when the true target is located at  $(x, y)$ . For estimated target location scatter plots, the estimated target location for each round of Monte Carlo simulation is marked such that spatial error distribution for each location method can be investigated.

Referring to the target location error color plots where measurement errors are independent of SNR (see Appendix H), the hyperbolic location method generally estimates target location more accurately compared to the elliptical location method as it uses fewer measurement sources. The hyperbolic method uses time delay measurements and transmitters and receiver position data, while the elliptic method uses DF measurements, time delay measurements and transmitter and receiver position data. When measurements with errors independent of SNR are used, it was observed that the effects of dilution of precision on target location estimates are less pronounced for the hyperbolic method (Figure 37).

To better model errors present in measurements used to estimate the target's location, target location models will include SNR-dependent errors in the DF and time delay measurements, as outlined in Section II.D. Simulating target location accuracy with various combination of erroneous and error-free measurements suggest that DF measurement is the dominant source of error in the elliptical method, while time delay measurement is the dominant source of error in the hyperbolic method. It was also observed that the effect of 2 meters drms error in transmitter and receiver position data are negligible compared to SNR-dependent DF and time delay measurements.

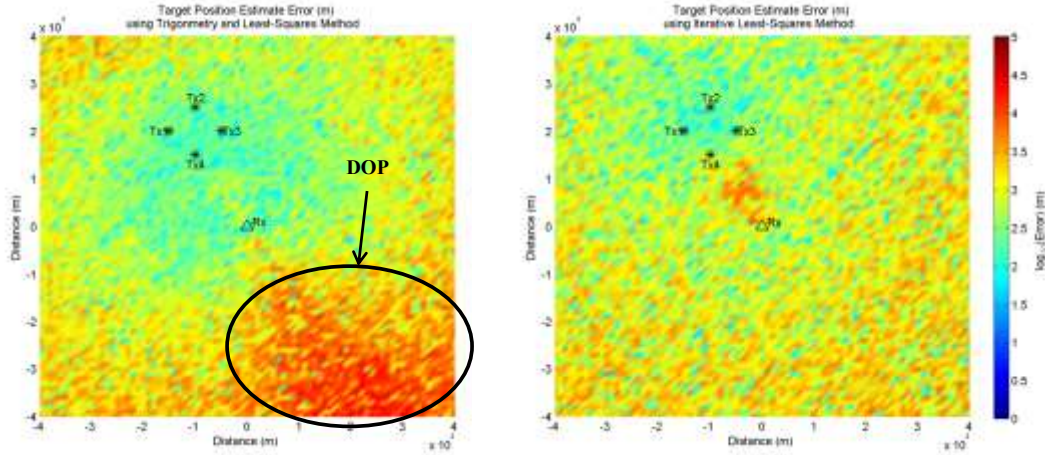


Figure 37. Dilution of precision comparison between elliptical and hyperbolic methods using SNR-independent measurement errors.

Referring to the target location error results where measurements with SNR-dependent measurement errors are used (Appendix H), the hyperbolic method, which uses fewer sources of measurement and data, produces more accurate location estimates compared to the elliptical method. However, overall location accuracy is poor due to low SNR and large DF and time delay measurement errors.

The results from the target location accuracy color plots mirror the observation made in detection coverage plots. Target location accuracy is best when the target lies within a transmitters-receiver cluster in receiver-centered geometry (Figure 38). Increasing the transmitter to receiver range effectively increases the transmitters-receiver cluster area but reduces the overall location accuracy within the cluster.

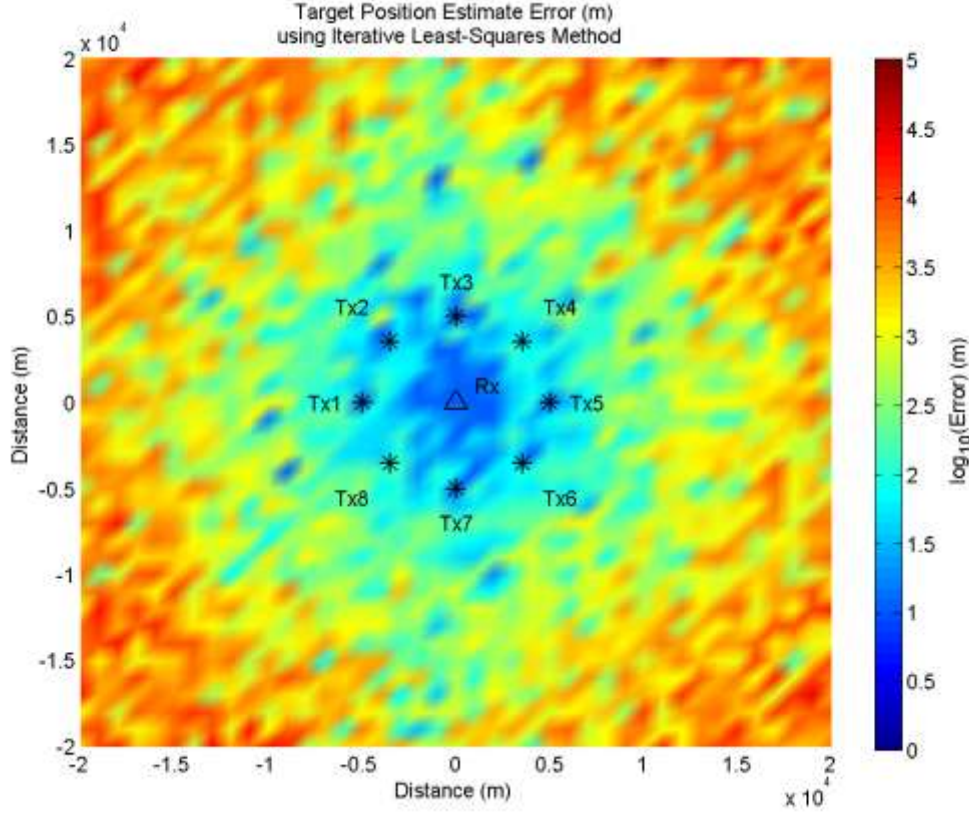


Figure 38. Target location errors using hyperbolic method (S-Band) with SNR-dependent measurement errors.

## 2. Error Ellipse of Target Position Estimate

To examine the spatial error distribution of target position estimates, 100 Monte Carlo simulations are performed for each transmitters-target-receiver geometry. The target position estimate from each Monte Carlo simulation is marked on a two-dimensional plot to produce a target location scatter plot. For the hyperbolic target location method, parameters of each estimate's error ellipse can be calculated for various levels of confidence. The equations used to compute the error ellipse semi-major axis length, semi-minor axis length, and orientation is covered briefly in Section II.E and derived in Appendix A.

Transmitter-receiver geometries can be broadly classified into two groups: (1) target within Tx-Rx cluster and (2) target outside Tx-Rx cluster.



Figure 39 and Figure 40 show the target location scatter plot from the elliptical and hyperbolic methods respectively when group (1) geometry occurs. The estimates from all 100 Monte Carlo simulations cover an approximately circular area, suggesting that the extent of target estimate uncertainty in the  $x$  and  $y$  direction is similar. The area covered by the scatter points is referred to as the error ellipse for position estimate. The error ellipse of estimates from the hyperbolic method is smaller than that from the elliptical method. This suggests that the hyperbolic method estimates target position more accurately.

Similarly, Figure 41 and Figure 42 show the target location scatter plot from the elliptical and hyperbolic methods respectively when group (2) geometry is considered. The estimates from all 100 Monte Carlo simulations in this case form an ellipse, exhibiting DOP. The resultant error ellipse from using the elliptical and hyperbolic method differs greatly with their semi-major axis appearing approximately orthogonal. To understand how measurement errors translate to uncertainty in the target location estimates, consider the graphical illustration in Figure 44 through Figure 47.

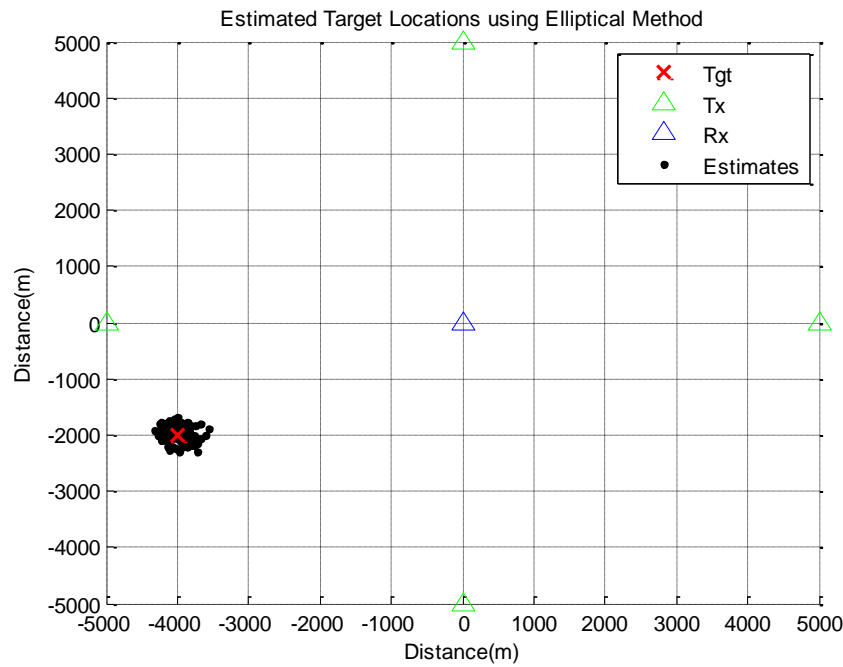


Figure 39. Target position estimate scatter plot from elliptical method for target in Tx-Rx cluster.

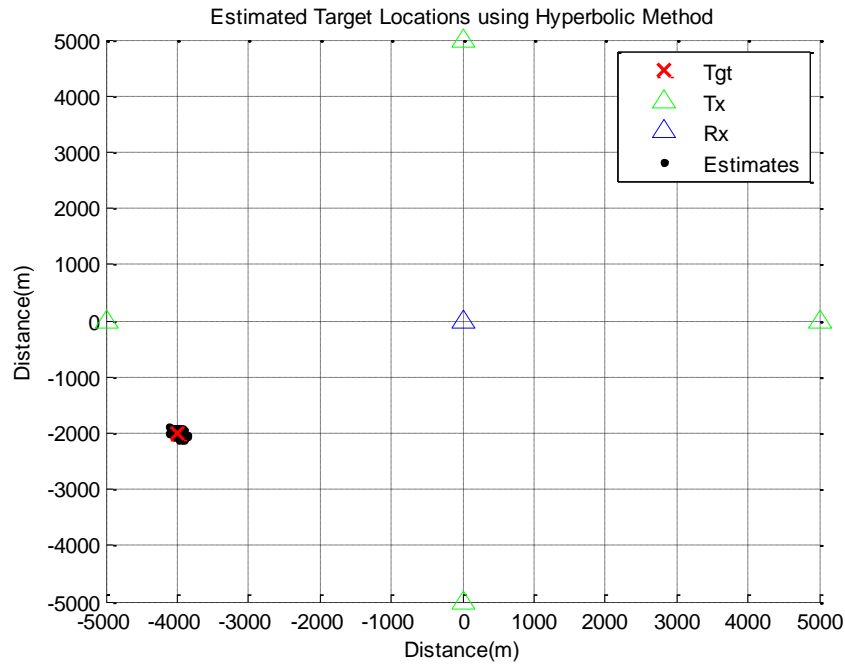


Figure 40. Target position estimate scatter plot from hyperbolic method for target in Tx-Rx cluster.

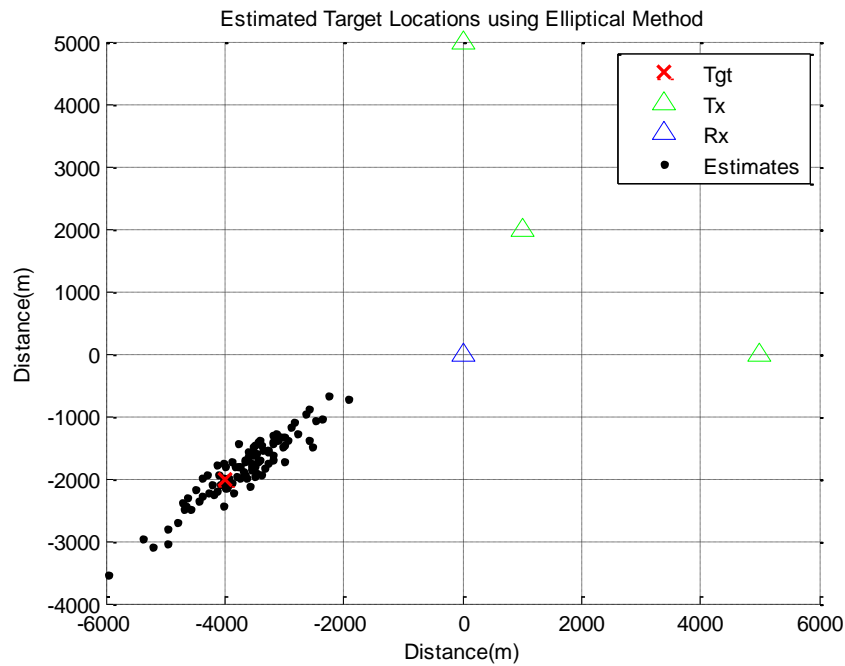


Figure 41. Target position estimate scatter plot from elliptical method for target outside Tx-Rx cluster.

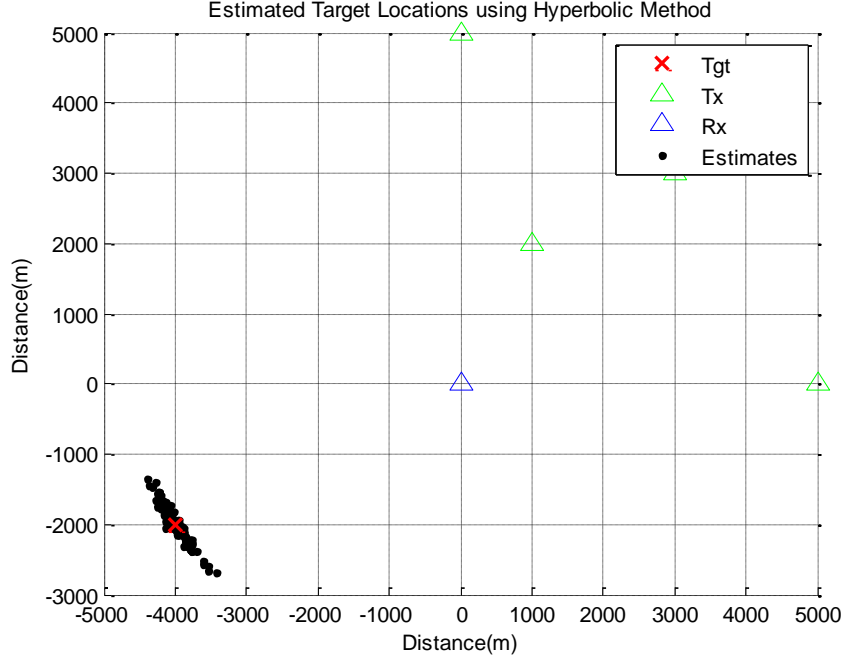


Figure 42. Target position estimate scatter plot from hyperbolic method for target outside Tx-Rx cluster.

In the elliptical location method, bistatic triangle parameters are computed using DF and time delay measurements as well as transmitters and receiver position data. The transmitter-to-target range  $R_T$ , receiver to target range  $R_R$ , and DF measurements are used to define several bearings which would intersect at the target's true position if all measurements are error-free. However, in reality, these bearings do not intersect at a single point, hence the elliptical method finds "best-fit" point of intersection and returns this point as the estimated target position. Graphically, uncertainty associated with each transmitter-to-target or receiver-to-target bearing is defined as a sector extending from the transmitter or receiver towards the target's position. The intersection of all sectors approximates the uncertainty associated with the target position. For geometry (1), the target position estimates from the elliptical method results in a relatively circular and small error ellipse (Figure 43), while for geometry (2), the error ellipse is eccentric with the semi-major axis aligned with the receiver's LOS (Figure 44).

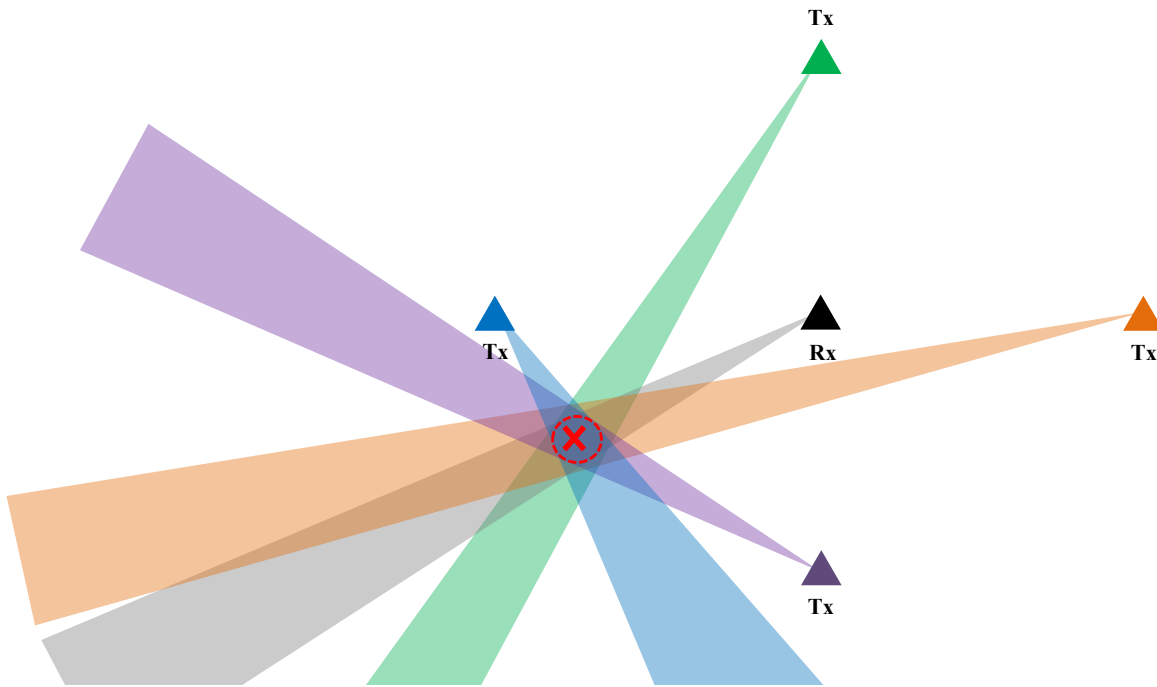


Figure 43. Uncertainty area associated with position estimates from elliptical method for target in Tx-Rx cluster.

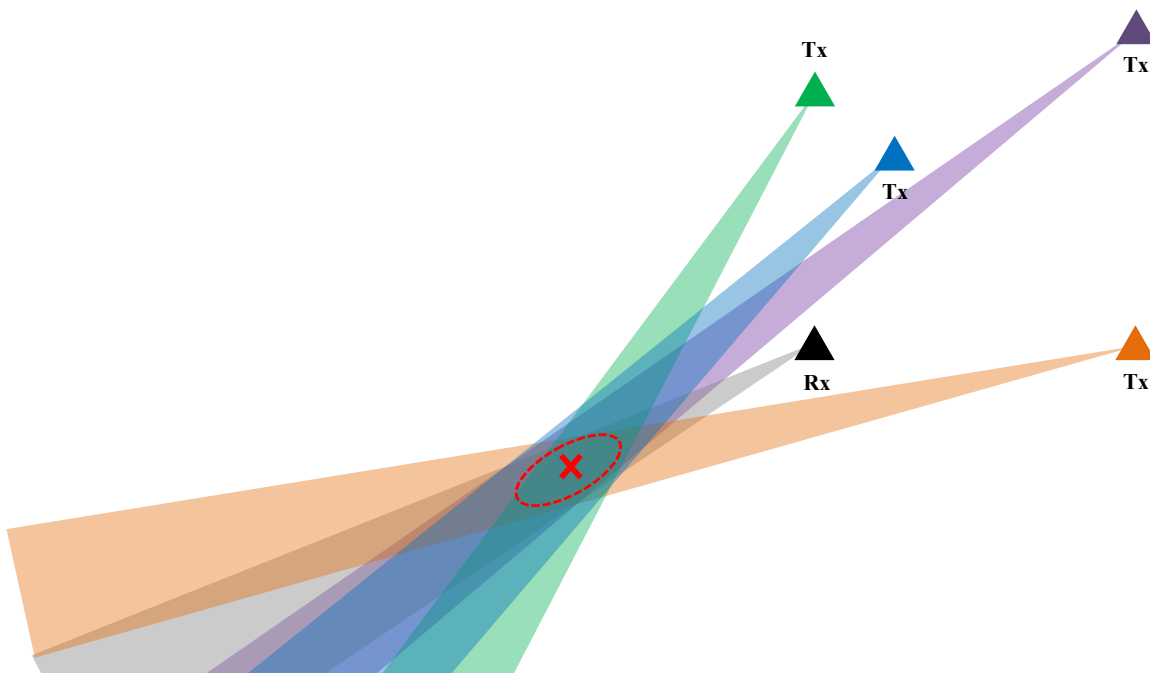


Figure 44. Uncertainty area associated with position estimates from elliptical method for target outside Tx-Rx cluster.

For the hyperbolic target location method, target position is estimated by minimizing the sum of squares of difference between time delay measurements and the estimated function. The range equivalent time delay measurement is defined by Eq. 12 and rewritten as

$$c\Delta T_{rt} = (R_T + R_R) - L. \quad (65)$$

For a transmitter-target-receiver pair, baseline  $L$  is constant; therefore, the time delay measurement will depend on the range sum  $(R_T + R_R)$ . As in Eq. 15, range sum equals twice the semi-major axis length. From the definition of an ellipse, the iso-contour of the constant time delay measurement is elliptical with the transmitter and receiver position as ellipse foci (Figure 45).

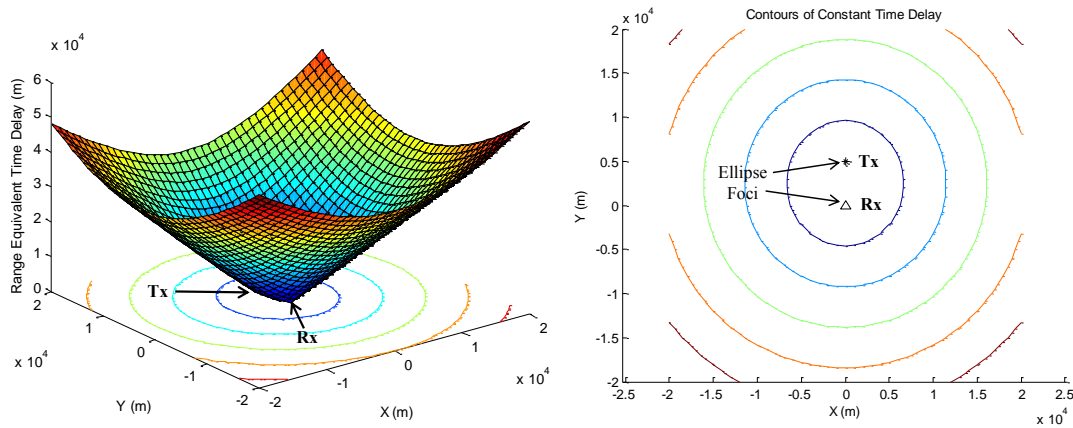


Figure 45. Elliptical iso-contours of constant time delay measurements with transmitter and receiver at ellipse foci.

In the hyperbolic target location method, an erroneous time delay measurement from a transmitter-target-receiver pair defines an ellipse with “thickness” in which the “thickness” is determined by the amount of error in the time delay measurement. The intersection of all ellipses approximates the uncertainty associated with the target position. For geometry (1), the target position estimates from the hyperbolic method result in a relatively circular and small error ellipse (Figure 46), while for geometry (2), the error

ellipse is eccentric with the semi-major axis perpendicular to the line extending from the target towards the receiver (Figure 47).

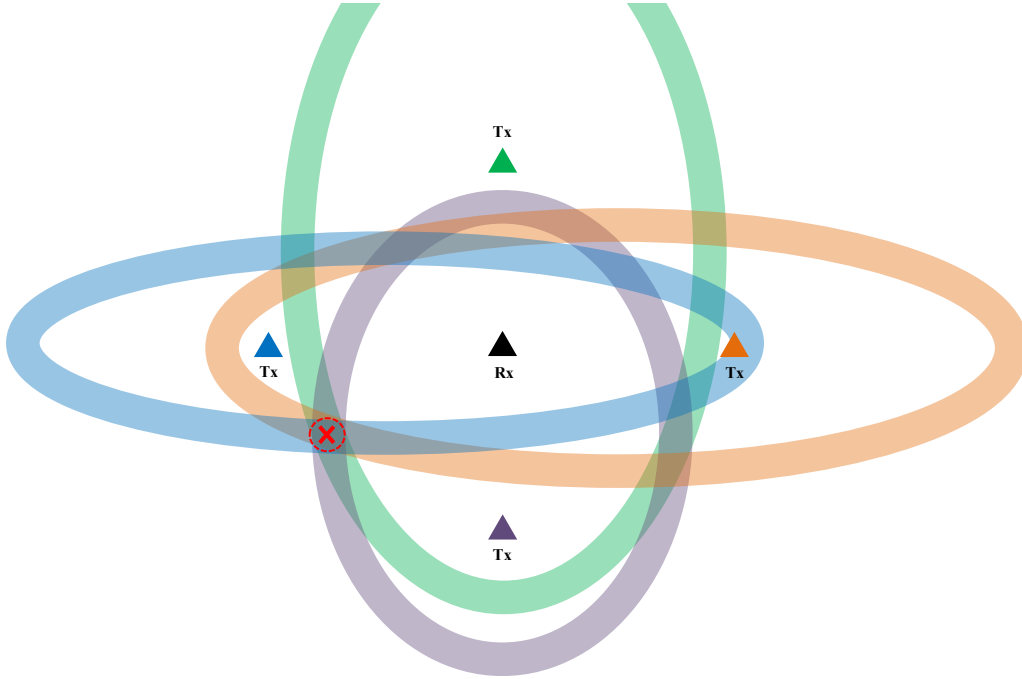


Figure 46. Uncertainty area associated with position estimates from hyperbolic method for target in Tx-Rx cluster.

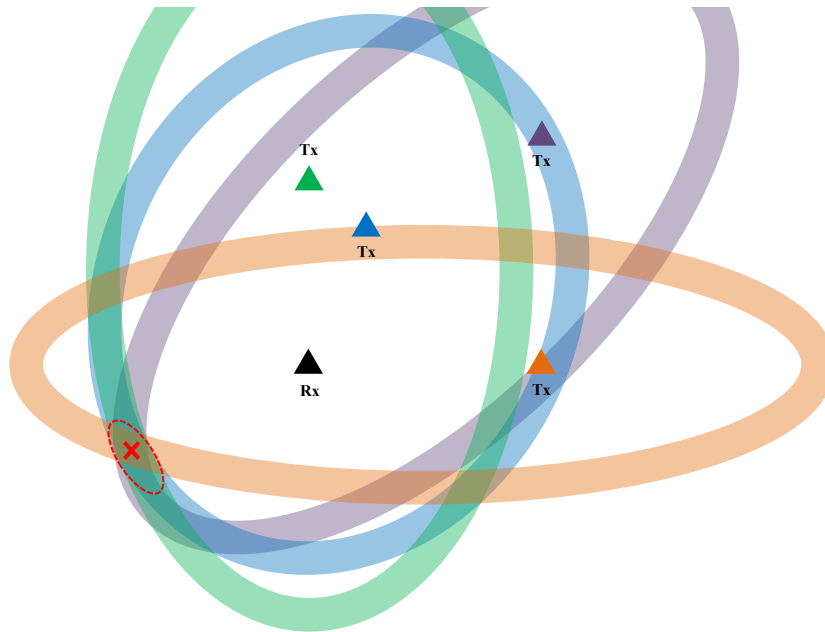


Figure 47. Uncertainty area associated with position estimates from hyperbolic method for target outside Tx-Rx cluster.

Comparing the scatter plots from the elliptical and hyperbolic methods in Figure 41 and Figure 42, respectively, it is evident that uncertainty associated with position estimates from the hyperbolic method is smaller. The error distribution of position estimates from elliptical and hyperbolic methods appear to be orthogonal and are more pronounced in geometries that exhibit DOP; that is, the semi-major axis of the error ellipse of estimates from the elliptical method is approximately aligned with the semi-minor axis of the error ellipse of estimates from the hyperbolic method, and vice versa. A possible option to improve target position estimates is to combine the elliptical and hyperbolic method in such a way that capitalizes on precision in their respective semi-minor axis direction.

Every target position estimate is accompanied by a measure of confidence. The method of computing the error ellipse parameters outlined in Section II.E and Appendix A is an indication of the estimate's accuracy. The error ellipse shows how measurement errors translate to the estimate's uncertainty given certain geometry with the ellipse semi-major and semi-minor axes being directions with greatest and least deviation. The size of the ellipse is determined by the critical chi-square value  $\chi^2_{2,\alpha}$  such that the area to the left  $(1-\alpha)\times 100\%$  is its corresponding confidence level. For a 90% confidence error ellipse, the critical chi-square value is 4.60, and it will enclose approximately 90% of the Monte Carlo position estimates. For the transmitters-target-receiver geometry in Figure 42, the error ellipse at various confidence levels for hyperbolic position estimates is shown in Figure 48. It was verified that the number of Monte Carlo estimates that fall within the ellipse agrees with the confidence level of the ellipse.

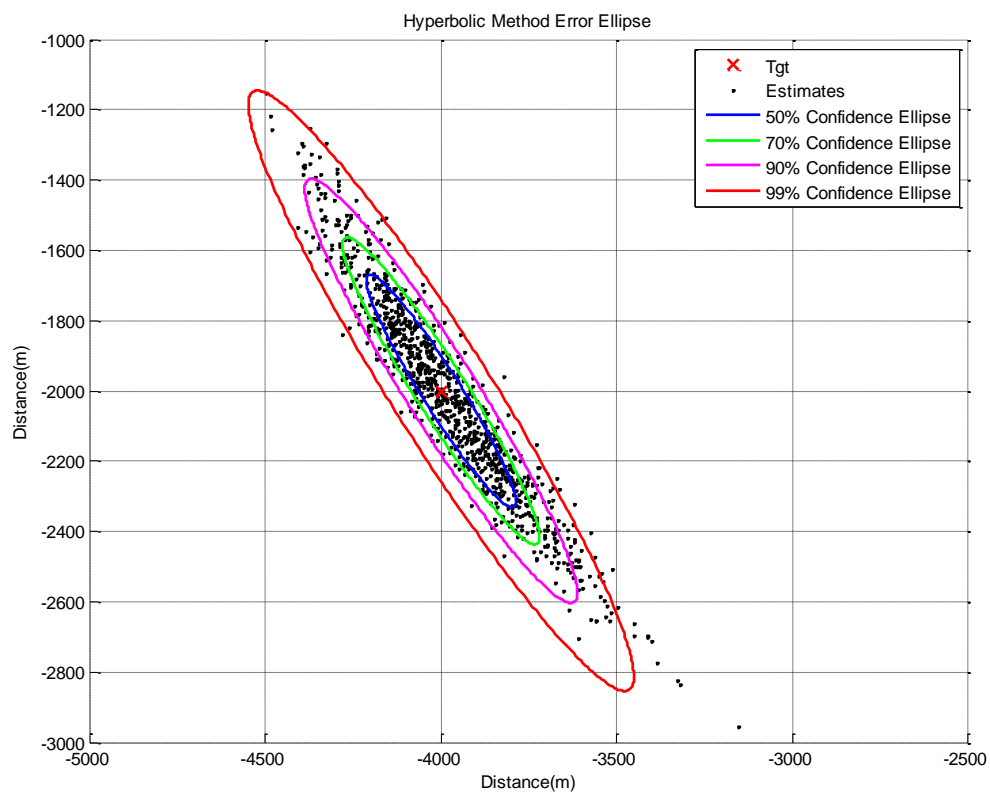


Figure 48. Hyperbolic target location estimate's error ellipse at 50%, 70%, 90%, and 99% confidence levels.



## **V. CONCLUSION**

### **A. SUMMARY OF FINDINGS**

This thesis explored two areas pertaining to the use of multiple passive non-cooperative opportunistic transmitters in target detection and location. To investigate these PBR issues, detection coverage and target location estimation models have been developed using FEKO and MATLAB software. The models were used to simulate detection performance and location estimation accuracy for various transmitter-target-receiver configurations in a maritime scenario with a low-RCS target.

The proposed PBR approach offers potential advantage in the detection of stealthy, low-RCS targets which are designed to minimize monostatic radar echoes. RCS returns of stealthy ships can be sufficiently large at certain return directions, allowing PBR to capitalize on this characteristic to detect low-RCS targets using opportunistic transmissions. Being a passive system allows the PBR receiver to remain covert, making it more resilient to detection and EA. The ability to leverage available transmission and to detect targets passively also serves to enhance situational awareness, thereby advancing one's position in the OODA loop during an operation. It is also advantageous to use multiple transmitters at separate locations for detection and target location estimation as it adds spatial diversity and reduces the effect of DOP.

#### **1. Findings for Detection Coverage**

Target detection performance varies with the number of transmitters, their parameters, and receiver parameters. It also depends upon the bistatic RCS scattering characteristic of the target. Detection performance—received target echo SNR and area with good target echo SNR—improves with the number of opportunistic transmitters and is observed to vary significantly with a slight change in receive angle due to the rapid variation in RCS returns versus angle from a target. Overall detection coverage area increases as transmitter(s) to receiver range increase at the expense of overall sensitivity. Detection coverage is generally the best when the target is located within the transmitters-receiver cluster with the highest SNR observed when the transmitter-target-

receiver is in the forward-scattering configuration. Detection gaps—defined as areas with the low SNR at the receiver—occur when the target is outside the transmitters-receiver cluster or away from bearings extending from the transmitter-receiver baseline. Outside the cluster of transmitters-receiver, detection is better when the transmitter-target-receiver is in the back-scattering configuration. Other than the areas that satisfy a back-scattering configuration, it is observed that there are additional areas or hyperbolic-like curves—typical of TDOA measurements—extending from the transmitters that exhibit good detection coverage. Therefore, the optimal transmitters-target-receiver configuration and geometry for target detection coverage is such that the target is within the spatial “net” of transmitters-receiver. The findings with regard to detection coverage align with the findings and observations in [4, 40].

## **2. Findings for Target Location**

Two target location estimation methods were investigated: (1) elliptical method and (2) hyperbolic method. The elliptical method solves for the bistatic triangle parameters for each PBR pair; these parameters are then used to define transmitter-to-target and receiver-to-target bearings, after which the “best fit” point of intersection is estimated as the target position. In the hyperbolic method, time delay measurements from all PBR pairs are used to estimate the target’s location by finding the least-squares solution. The results from the target location model showed that the DF measurement error is the dominant source of error for the elliptical method, while the time delay measurement error is the primary source of error for the hyperbolic method. The hyperbolic method generally estimates the target’s location more accurately than the elliptical method as it uses fewer measurement sources. It was also observed that overall location accuracy is poor when measurement errors are modeled as dependent on the SNR of the received target echo.

When SNR-dependent measurement errors are considered, results from the target location model agree closely with the observations made from the detection coverage results. Target location methods produce the most accurate results when the target lies within the transmitters-receiver cluster in a receiver-centered geometry. The transmitters-

receiver cluster area can be expanded by increasing the transmitters to receiver range; however, this reduces the overall location accuracy within the cluster.

Monte Carlo simulations are performed for both target location methods to explore the relation between spatial error distribution and transmitter-target-receiver geometry. The results from Monte Carlo simulations in a scatter plot reveal the uncertainty area associated with the target location estimate for a particular geometry. Across all geometries, the uncertainty area associated with estimates from the hyperbolic method covers a smaller area compared with that from the elliptical method, suggesting that the hyperbolic method estimates the target location with higher accuracy. For targets within the cluster of transmitters-receiver, the uncertainty area would be approximately circular. However, when targets are outside the cluster of transmitters-receiver, the uncertainty area is elliptical. Graphical illustrations were presented to understand how measurement errors translate to uncertainty estimates for both methods. Monte Carlo simulation results from the target location model showed that the elliptical and hyperbolic target location methods have approximately orthogonal error distribution, which are more pronounced when the uncertainty area associated with the estimates are elliptical. That is, the semi-major axis of the error ellipse of estimates from the elliptical method is approximately aligned with the semi-minor axis of the error ellipse of estimates from the hyperbolic method, and vice versa.

The method to compute the error ellipse parameters associated with the hyperbolic method was presented and included in the target location model. Every target position estimated from the hyperbolic method would be accompanied by a measure of confidence in the form of an error ellipse. Like Monte Carlo simulations, the error ellipse shows how measurement errors translate to an estimate's uncertainty. For an error ellipse at  $(1 - \alpha) \times 100\%$  confidence,  $(1 - \alpha)$  of the 100 Monte Carlo simulated estimates will, on average, fall within the computed ellipse.

## **B. FUTURE WORK**

Detection coverage models and target location models developed in this thesis can be further improved to include bistatic beam-to-beam issues and complex sources of

measurement and data error such as sea clutter and errors associated with sea-borne vessel's motion (e.g., pitch and roll). Real data can be used in the models developed in this study to extend the findings regarding target detection coverage and location accuracy. An extension to the current work is to investigate the feasibility and performance of using multiple passive cooperative opportunistic transmitters in maritime target detection and location as proposed in [40]. A combined target location method that leverages on the spatial precision of the elliptical and hyperbolic target location methods can be explored to improve estimation accuracy. Alternatively, the use of other sources of measurements, like Doppler information to estimate the target's location, can be investigated.

With target detection and location in place, the next step is to explore tracking algorithms, classification methods, and identification methods. The MIMO tracking algorithm, which uses the coherent-on-receiver method [41] or the track-before-detect method that enables tracking and detection of targets in low SNR environments [42], are feasible options. As stated in [4], an interesting extension would be to consider the use of bistatic ISAR signatures in the forward-scattering and back-scattering configurations to aid in target identification and classification [25].

## APPENDIX A. DERIVATION OF ERROR ELLIPSE PARAMETERS FROM BIVARIATE NORMAL DISTRIBUTION

This appendix presents the derivation of parameters that define the error ellipse [38]. To understand the how measurement errors translate to estimate position uncertainty in the form of an error ellipse, consider a univariate normal distribution with mean  $\mu$  and variance  $\sigma^2$  for the random variable  $X$ :

$$f(x) = \frac{1}{\sqrt{2\pi\sigma^2}} e^{-\frac{(x-\mu)^2}{2\sigma^2}}, \quad (66)$$

for  $-\infty < x < \infty$ ,  $-\infty < \mu < \infty$  and  $\sigma^2 > 0$ .

Similarly, a multivariate normal distribution with mean  $\mathbf{\mu}$  and covariance  $\Sigma$  for random variables in  $\mathbf{X}$  is expressed as

$$f(\mathbf{X}) = \frac{1}{\sqrt{(2\pi)^p |\Sigma|}} e^{-\frac{1}{2}(\mathbf{X}-\mathbf{\mu})^T \Sigma^{-1}(\mathbf{X}-\mathbf{\mu})} \quad (67)$$

for  $-\infty < \mathbf{X} < \infty$ ,  $-\infty < \mathbf{\mu} < \infty$  and for positive definite  $\Sigma$ . Eq. 67 is derived from Eq. 66

by rewriting the term  $\frac{(x-\mu)^2}{\sigma^2}$  in linear algebra formulation:

$$(x-\mu)^T (\sigma^2)^{-1} (x-\mu), \quad (68)$$

$$(\mathbf{X}-\mathbf{\mu})^T \Sigma^{-1} (\mathbf{X}-\mathbf{\mu}). \quad (69)$$

Eq. 69 is the squared Mahalanobis distance where  $\mathbf{X}$  and  $\mathbf{\mu}$  are  $(p \times 1)$  vectors,  $\Sigma$  is a  $(p \times p)$  positive definite covariance matrix, and  $p$  denotes the number of variables in vector  $\mathbf{X}$ .

To derive the semi-major axis and semi-minor axis lengths of an error ellipse in the XY-plane, reduce Eq. 67 into a bivariate normal distribution where

$$\mathbf{X} = \begin{bmatrix} x \\ y \end{bmatrix}, \mathbf{\mu} = \begin{bmatrix} \mu_x \\ \mu_y \end{bmatrix}, \Sigma = \begin{bmatrix} \sigma_x^2 & \rho_{xy}\sigma_x\sigma_y \\ \rho_{yx}\sigma_y\sigma_x & \sigma_y^2 \end{bmatrix}. \quad (70)$$

By substituting Eq. 70 into the Mahalanobis distance in Eq. 69,

$$(\mathbf{X}-\boldsymbol{\mu})^T \Sigma^{-1} (\mathbf{X}-\boldsymbol{\mu}) = \frac{1}{1-\rho_{xy}^2} \left[ \frac{(x-\mu_x)^2}{\sigma_x^2} - \frac{2\rho_{xy}(x-\mu_x)(x-\mu_y)}{\sigma_x\sigma_y} + \frac{(x-\mu_y)^2}{\sigma_y^2} \right], \quad (71)$$

the probability density function of a pair of jointly Gaussian random variables is then expressed as

$$f_{XY}(x, y) = \frac{1}{2\pi\sigma_x\sigma_y\sqrt{1-\rho_{xy}^2}} e^{\left\{ -\frac{1}{2(1-\rho_{xy}^2)} \left[ \frac{(x-\mu_x)^2}{\sigma_x^2} - \frac{2\rho_{xy}(x-\mu_x)(x-\mu_y)}{\sigma_x\sigma_y} + \frac{(x-\mu_y)^2}{\sigma_y^2} \right] \right\}}, \quad (72)$$

for  $-\infty < x < \infty$ ,  $-\infty < y < \infty$ .

Figure 49 shows the joint Gaussian probability density function (pdf) for various correlation and standard deviation values. The shape and orientation of the joint Gaussian pdf surface depends on the values of  $\sigma_x$ ,  $\sigma_y$ , and  $\rho_{xy}$ , while the size of the surface contours depends on the pdf value  $f_{XY}(x, y)$  in consideration.

An error ellipse is defined as a locus of points with constant  $f_{XY}(x, y)$  values, as seen in the surface contour plots in Figure 49. Graphically, the error ellipse is the points of intersection between the pdf surface and a horizontal plane. Given the values of  $\sigma_x$ ,  $\sigma_y$ , and  $\rho_{xy}$ ,  $f_{XY}(x, y)$  is constant for values of  $x$  and  $y$  when the exponential argument in Eq. 72 is constant. Mathematically, this is expressed as

$$(\mathbf{X}-\boldsymbol{\mu})^T \Sigma^{-1} (\mathbf{X}-\boldsymbol{\mu}) = c. \quad (73)$$

Let  $\mathbf{X}_1 = \mathbf{X}-\boldsymbol{\mu}$  such that Eq. **Error! Reference source not found.** reduces to

$$\mathbf{X}_1^T \Sigma^{-1} \mathbf{X}_1 = c. \quad (74)$$

Factorize the covariance matrix  $\Sigma$  by eigen-decomposition:

$$\Sigma = \mathbf{P}\mathbf{D}\mathbf{P}^{-1}, \quad (75)$$

where  $\mathbf{P}$  is a matrix of eigenvectors and  $\mathbf{D}$  is a diagonal matrix whose elements are the corresponding eigenvalues  $(\lambda_1, \lambda_2)$ .

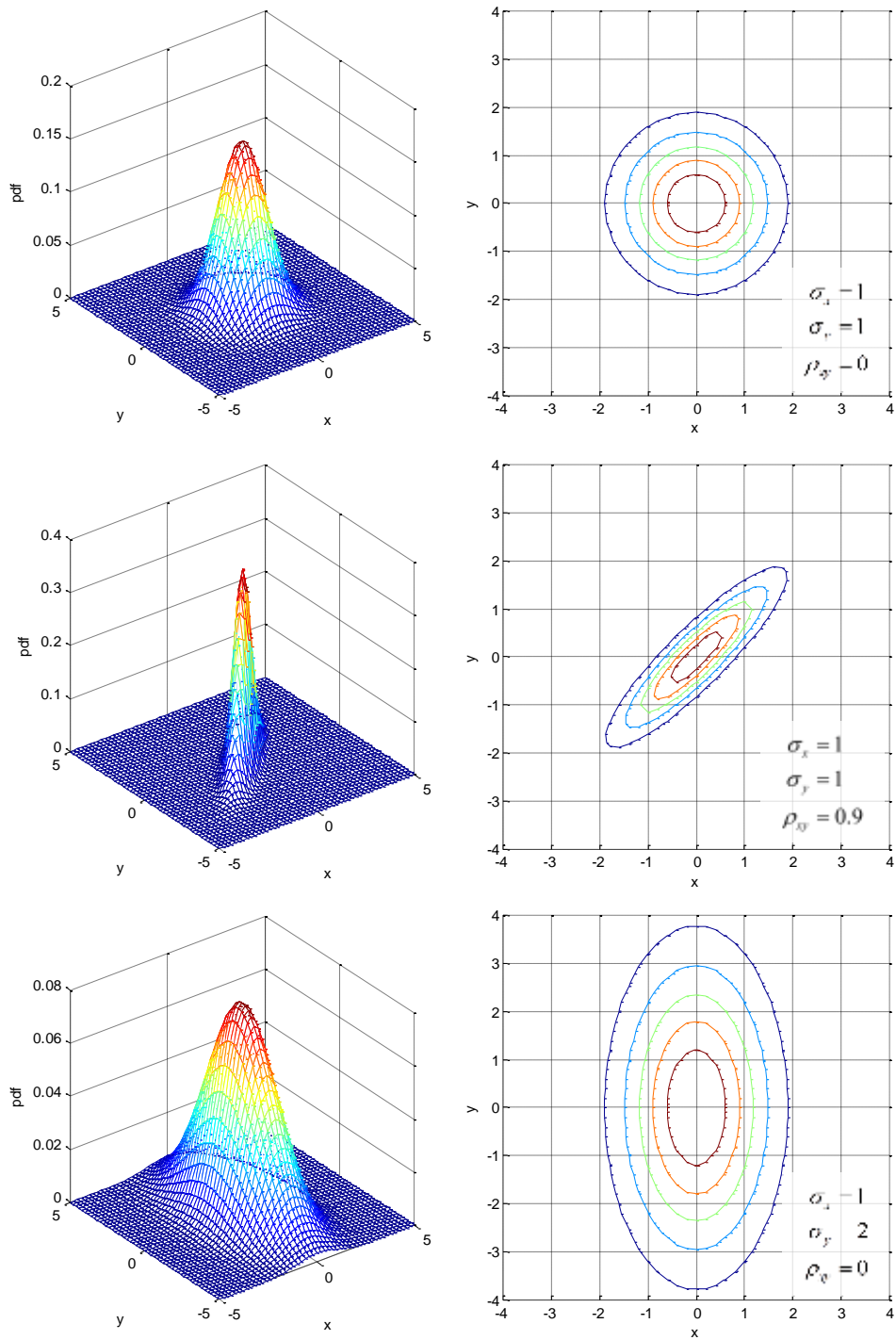


Figure 49. Joint Gaussian pdf surface and contours for various  $\sigma_x$ ,  $\sigma_y$ , and  $\rho_{xy}$  values. After [38].

The eigenvectors of the covariance matrix represent the direction in which the data varies the most and are the vectors along the error ellipse's semi-major and semi-minor axis. The corresponding eigenvalues indicate the spread of the data in the direction of the eigenvectors (Figure 50). For an axis-aligned error ellipse such that covariance is zero, the eigenvalues equal the variances of the covariance matrix, and the eigenvectors are in the direction of the x-axis and y-axis. However, for correlated data, the eigenvectors represent the direction with the largest spread of data and the eigenvalue determines the extend of spread.

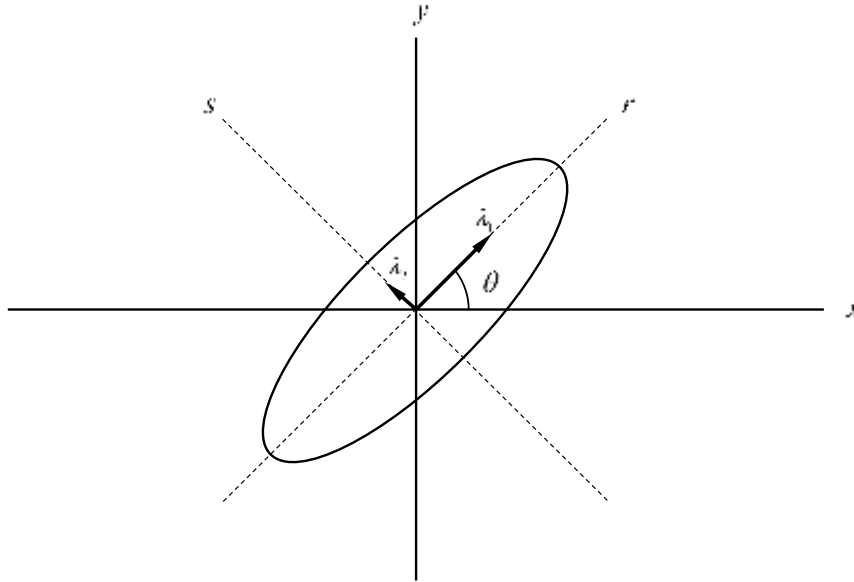


Figure 50. Eigenvectors  $(\lambda_1, \lambda_2)$  of a covariance matrix on an error ellipse.

If  $\Sigma$  is a symmetric matrix,  $\mathbf{P}^{-1} = \mathbf{P}^T$ , Eq. 75 is then expressed as

$$\Sigma = \mathbf{P}\mathbf{D}\mathbf{P}^T. \quad (76)$$

When  $\Sigma$  can be eigen-decomposed and when none of its eigenvalues are zero, then  $\Sigma$  is non-singular and its inverse is given by

$$\Sigma^{-1} = \mathbf{P}\mathbf{D}^{-1}\mathbf{P}^T \quad (77)$$

and

$$\mathbf{D}^{-1} = \mathbf{P}^T \Sigma^{-1} \mathbf{P}. \quad (78)$$



As illustrated in Figure 50, define the  $r$ -axis and  $s$ -axis as the principle axis of the error ellipse. The principle axis is defined as rotating the original  $x$ -axis and  $y$ -axis through an angle  $\theta$  and is expressed mathematically as

$$\begin{bmatrix} x \\ y \end{bmatrix} = \mathbf{P} \begin{bmatrix} r \\ s \end{bmatrix}. \quad (79)$$

To determine the semi-major and semi-minor axis lengths of the error ellipse, substitute Eq. 78 and Eq. 79 into Eq. 74

$$\begin{aligned} [r \ s] \mathbf{P}^T \Sigma^{-1} \mathbf{P} [r \ s]^T &= c \\ [r \ s] D^{-1} [r \ s]^T &= c \\ [r \ s] \begin{bmatrix} 1/\lambda_1 & 0 \\ 0 & 1/\lambda_2 \end{bmatrix} [r \ s]^T &= c \\ \frac{r^2}{\lambda_1} + \frac{s^2}{\lambda_2} &= c. \end{aligned} \quad (80)$$

The general form of an ellipse centered at the origin is

$$\frac{x^2}{a^2} + \frac{y^2}{b^2} = 1 \quad (81)$$

where  $a$  and  $b$  are the semi-major and semi-minor axis lengths, respectively. Comparing Eq. 80 and Eq. 81,

$$\left. \begin{aligned} a &= \sqrt{c\lambda_1} \\ b &= \sqrt{c\lambda_2} \end{aligned} \right\}_{\lambda_1 > \lambda_2}. \quad (82)$$

To understand the significance of the constant  $c$ , consider a  $(p \times 1)$  multivariate normal vector  $\mathbf{X} \sim N(\boldsymbol{\mu}, \Sigma)$ . Geometrically, degrees of freedom is interpreted as the dimension of the vector subspace. Hence, the squared Mahalanobis distance between  $\mathbf{X}$  and  $\boldsymbol{\mu}$  is a chi-square distribution with  $p$  degrees of freedom (Figure 51):

$$(\mathbf{X} - \boldsymbol{\mu})^T \Sigma^{-1} (\mathbf{X} - \boldsymbol{\mu}) \sim \chi_p^2. \quad (83)$$

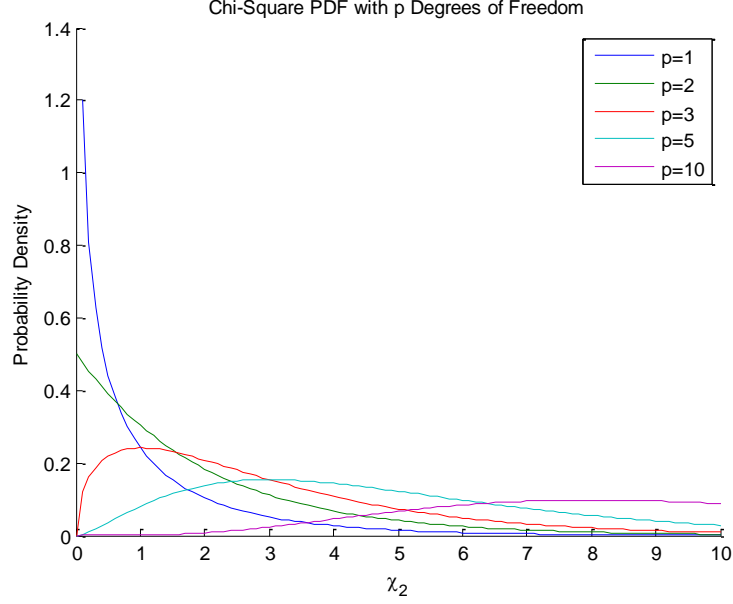


Figure 51. Chi-square pdf for  $p$  degrees of freedom.

For a hyper-ellipse, defined as the squared Mahalanobis distance equal to a critical value of a chi-square distribution with  $p$  degrees of freedom and evaluated at  $\alpha$ , the probability of the random vector  $\mathbf{X}$  falling inside the ellipse is  $1 - \alpha$ .

$$\Pr\left\{(\mathbf{X}-\boldsymbol{\mu})^T \boldsymbol{\Sigma}^{-1}(\mathbf{X}-\boldsymbol{\mu}) \leq \chi_p^2\right\} = 1 - \alpha \quad (84)$$

where  $\alpha$  refers to the area to the right of the chi-square critical value (Figure 52).

Therefore, the hyper-ellipse is defined as a locus of points with constant  $f_{XY}(x, y)$  values such that

$$(\mathbf{X}-\boldsymbol{\mu})^T \boldsymbol{\Sigma}^{-1}(\mathbf{X}-\boldsymbol{\mu}) = \chi_p^2. \quad (85)$$

By comparing Eq. 73 and Eq. 85, Eq. 82 can be written as

$$\left. \begin{aligned} a &= \sqrt{\chi_{2,\alpha}^2 \lambda_1} \\ b &= \sqrt{\chi_{2,\alpha}^2 \lambda_2} \end{aligned} \right\}_{\lambda_1 > \lambda_2}. \quad (86)$$

For a two-dimensional hyper-ellipse, the chi-squared distribution with two degrees of freedom,  $p = 2$  will be used.

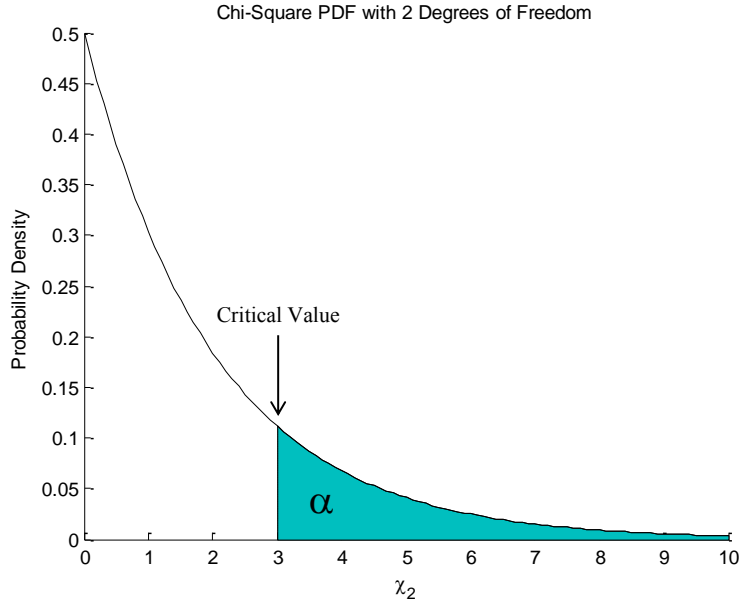


Figure 52. Chi-square pdf where the area to the right of the critical value is  $\alpha$ .

For an error ellipse with confidence level  $(1-\alpha)\times 100\%$ , the relevant  $\chi_{2,\alpha}^2$  value in Eq. 86 is obtained from the chi-square distribution table. A sample of a chi-square distribution table is given in Table 8.

Table 8. Chi-square distribution table

Degrees of Freedom	Probability										
	0.95	0.90	0.80	0.70	0.50	0.30	0.20	0.10	0.05	0.01	0.001
1	0.004	0.02	0.06	0.15	0.46	1.07	1.64	2.71	3.84	6.64	10.83
2	0.10	0.21	0.45	0.71	1.39	2.41	3.22	4.60	5.99	9.21	13.82
3	0.35	0.58	1.01	1.42	2.37	3.66	4.64	6.25	7.82	11.34	16.27
4	0.71	1.06	1.65	2.20	3.36	4.88	5.99	7.78	9.49	13.28	18.47
5	1.14	1.61	2.34	3.00	4.35	6.06	7.29	9.24	11.07	15.09	20.52

Referring to Figure 53, the error ellipse's principle axis  $[r \ s]$  is defined as the counterclockwise rotation of the original  $xy$ -axis  $[x \ y]$  through an angle  $\theta$ . The vector representation of the original  $xy$ -coordinates as a function of the  $rs$ -coordinates is

$$\boldsymbol{\varsigma} = \boldsymbol{A}\boldsymbol{\gamma} \quad (87)$$

where  $\boldsymbol{\varsigma} = [r \ s]^T$ ,  $\boldsymbol{\gamma} = [x \ y]^T$  and  $\mathbf{A} = \begin{bmatrix} \cos \theta & \sin \theta \\ -\sin \theta & \cos \theta \end{bmatrix}$ .

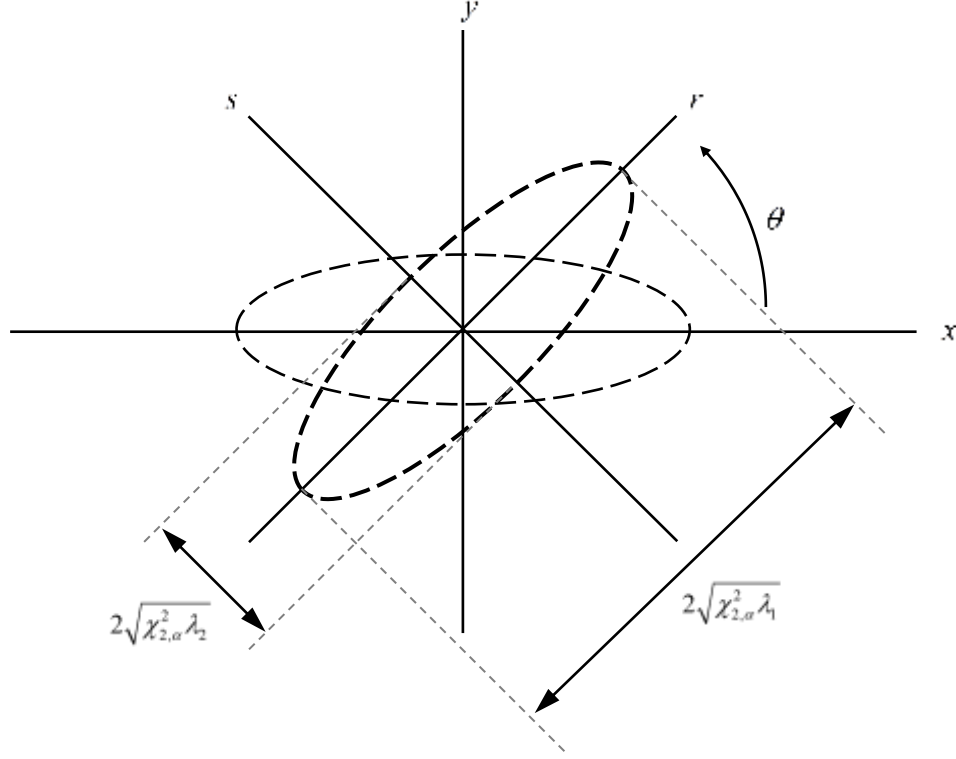


Figure 53. Rotation of error ellipse principle axis. From [38].

From Eq. 87,

$$\boldsymbol{\Sigma}_{\boldsymbol{\varsigma}} = \mathbf{A} \boldsymbol{\Sigma}_{\boldsymbol{\gamma}} \mathbf{A}^T, \quad (88)$$

$$\boldsymbol{\Sigma}_{\boldsymbol{\varsigma}} = \begin{bmatrix} \sigma_r^2 & 0 \\ 0 & \sigma_s^2 \end{bmatrix}, \quad (89)$$

$$\boldsymbol{\Sigma}_{\boldsymbol{\gamma}} = \begin{bmatrix} \sigma_x^2 & \rho_{xy} \sigma_x \sigma_y \\ \rho_{xy} \sigma_x \sigma_y & \sigma_y^2 \end{bmatrix}. \quad (90)$$

Substituting Eq. 89 and Eq. 90 into Eq. 88 yields

$$\begin{bmatrix} \sigma_r^2 & 0 \\ 0 & \sigma_s^2 \end{bmatrix} = \begin{bmatrix} \cos \theta & \sin \theta \\ -\sin \theta & \cos \theta \end{bmatrix} \begin{bmatrix} \sigma_x^2 & \rho_{xy} \sigma_x \sigma_y \\ \rho_{xy} \sigma_x \sigma_y & \sigma_y^2 \end{bmatrix} \begin{bmatrix} \cos \theta & -\sin \theta \\ \sin \theta & \cos \theta \end{bmatrix},$$

which is further reduced to

$$\sigma_r^2 = \sigma_x^2 \cos^2 \theta + 2\rho_{xy} \sigma_x \sigma_y \sin \theta \cos \theta + \sigma_y^2 \sin^2 \theta, \quad (91)$$

$$\sigma_s^2 = \sigma_x^2 \sin^2 \theta - 2\rho_{xy} \sigma_x \sigma_y \sin \theta \cos \theta - \sigma_y^2 \cos^2 \theta, \quad (92)$$

$$0 = (\sigma_y^2 - \sigma_x^2) \sin \theta \cos \theta + \rho_{xy} \sigma_x \sigma_y (\cos^2 \theta - \sin^2 \theta). \quad (93)$$

Simplifying Eq. 92 gives the orientation of the error ellipse:

$$\theta = \frac{1}{2} \tan^{-1} \left( \frac{2\rho_{x_e y_e} \sigma_{x_e} \sigma_{y_e}}{\sigma_{x_e}^2 - \sigma_{y_e}^2} \right). \quad (94)$$

THIS PAGE INTENTIONALLY LEFT BLANK

## APPENDIX B. SPECIFICATION SHEET FOR MANTADIGITAL RADAR BY KELVIN HUGHES

# NAVIGATION RADAR

## MANTADIGITAL™ RADAR SYSTEMS



Kelvin Hughes offers a range of radar systems. From the state of the art SharpEye™ solid state technology to conventional magnetron transceivers, all with our innovative multifunction MantaDigital™ displays and low profile antennas.

Variants include: 10kW and 25kW in X band frequency; 30kW magnetron and SharpEye™ 200W solid state transceiver in S band frequency.

### DISPLAY TECHNOLOGY

The MantaDigital™ multifunction navigation workstation provides radar, chart radar, ECDIS and Conning functionality in a single station. The different type Approved modes can all be displayed with a simple 'point and click' at the relevant screen icon.

Key features include dual PPI, ETD (Enhanced Target Detection), ice detection, chart radar, dynamic clutter suppression, vessel predictor and radar overlay.

### ENHANCED TARGET DETECTION

ETD significantly enhances the display of all targets without interfering with the normal radar appearance or operation. This is achieved by correlating returns over a long period of time and then allocating colour shades depending on the persistency of a return and using different colours for stationary and moving targets. When combined with the dual PPI, the operator can continue using the radar in the normal way with the addition of an advanced detection view on the secondary PPI. ETD is of great benefit in ice or for detecting floating debris and small boats.

### DUAL PPI

The modern radar display risks becoming cluttered with information such as from ARPA symbology, trails, AIS and Chart data. When looking for small intermittent contacts, this is not ideal and so we have introduced a second PPI screen. This allows the navigator to benefit from the data while still being able to keep a clear screen for small target searches. The second screen can be configured independently of the first and so, for example, trails can be set to Track on one and Relative on the other, giving the Navigator a better and instant visual appreciation of the risk of collision and course and speed of other vessels.

### SHARPEYE™ SOLID STATE TECHNOLOGY

No magnetron equals no routine maintenance, ultra high reliability, and low cost of ownership.

Despite the low (200W) peak power, the detection performance, especially in poor weather conditions, is superior to that of magnetron radars. Radar performance gets benefits from the transceiver being positioned aboard, thereby minimising signal loss in the waveguide while also simplifying installation. The high reliability and lack of routine maintenance means the need to subsequently access the transceiver is almost removed.

### ANTENNA AND TURNING UNITS

Antennas available are 1.5m, 1.0m and 0.5m in X band frequency and 0.9m in S band frequency, and are all of the patented low profile design to reduce wind loading and increase in-service life. The antennas use the polyrod lens principle that allows a reduced vertical dimension enabling a significantly lighter and low profile design that reduces the stress on the rotor and gearbox.



SITUATIONAL INTELLIGENCE. THE WORLD OVER.

## MANTADIGITAL™ RANGE

SYSTEM	SIZE	DESCRIPTION	TRANSCIVER	ANTENNA
10kW	MD1	22" DISPLAY	10kW S-BAND UPLINK	5.2m IT 90°
	MD6	30" DISPLAY	10kW S-BAND UPLINK	5.2m ANTENNA OPTION
		10kW S-BAND UPLINK	10kW S-BAND UPLINK	TURNING UNIT (PROVIDES HOLDING FOR 10kW TRANSMITTERS)
2kW	MD10	22" DISPLAY	2kW S-BAND UPLINK	3.0m IT 90°
	MD11	30" DISPLAY	2kW S-BAND UPLINK	3.0m ANTENNA OPTION
SHARPEYE™	MD12	22" DISPLAY	5.0kW S-BAND UPLINK	4.0m ANTENNA
	MD13	30" DISPLAY	5.0kW S-BAND UPLINK	TURNING UNIT (PROVIDES HOLDING FOR SHARPEYE™ TRANSMITTERS)
		5.0kW S-BAND UPLINK	5.0kW S-BAND UPLINK	DRIVE CONTROL UNIT
3.0kW	MD14	22" DISPLAY	3.0kW S-BAND UPLINK	3.0m ANTENNA
	MD15	30" DISPLAY	3.0kW S-BAND UPLINK	TURNING UNIT

TRANSCIVER SPEC	10kW	25kW	SHARPEYE™	30kW
REAL POWER	10kW	25kW	~150W (33W SYNTH)	30kW
MAXIMUM LIFE	10,000 HRS TYPICAL	10,000 HRS TYPICAL	NO MAINTENANCE	10,000 HRS TYPICAL
WORKS PROBABLY	NO	YES	YES (100% RELIABLE)	NO
FREQUENCY BAND	0.1-10MHz +/- 30MHz	0.1-10MHz +/- 30MHz	0.1-10.0 MHz 8 GHz (40% CHANNELS)	0.05-10MHz +/- 10MHz
FREQUENCY	0.1-10MHz	0.1-10MHz	0.1-10MHz	0.1-10MHz
PULSE COMPRESSION @	500ns/1000ns	100ns/1000ns	-	500ns/1000ns
PULSE COMPRESSION (M)	200ns/1000ns	200ns/1000ns	-	200ns/1000ns
PULSE COMPRESSION (L)	600ns/1000ns	900ns/1000ns	-	600ns/1000ns
RECOVER TIME	200 NS	200 NS	~100 NS	200 NS
RECOVER @ FREQUENCY	10MHz	10MHz	10MHz	10MHz
RECOVER @ BANDWIDTH	60MHz	60MHz	10MHz	60MHz
MINIMUM RANGE	100m	100m	100m	100m
RANGE RESOLUTION	100m (10m to 100m) 100m	100m (10m to 100m) 100m	100m	100m (10m to 100m) 100m

\* SharpEye™ transmits a non-linear sequence of S, M and L pulses simultaneously. Each transmission is unique, enabling pulse compression.

[illegible]

UK (Head Office): Kelvin Hughes Ltd  
Voltage, Molson Avenue,  
Enfield EN3 7JL, UK  
t: +44 (0)1992 856 300

**BeneLux:** Kelvin Hughes (Nederland) BV  
Postbus 11 E-451 10-418 T&T

Far East: Kelvin Hughes Pte Ltd  
Singapore t. +65 6545 9880

Scandinavia: A/S Kelvin Hughes  
Copenhagen T. +45 44 23 22 27

USA: Kelvin Hughes LLC  
New Orleans, LA +1 504 731 2999

WWW.KELVINHUGHES.COM

curved@cam.ac.uk



SITUATIONAL INTELLIGENCE: THE WORLD OVER

INFORMATION SUBJECT TO CHANGE WITHOUT NOTICE | (MAY 2014 ISSUE)

Figure 54. Technical Specifications for MantaDigital Radar by Kelvin Hughes.  
From [43].



## APPENDIX C. SPECIFICATION SHEET FOR TELEDYNE DEFENCE QR026 EW RECEIVER



**TELEDYNE  
DEFENCE**

A Teledyne Technologies Company

0.5 to 18GHz  
High Performance Receiver  
**Technical Data QR026**



### Features

- Full Band Coverage Options to >40GHz
- Fast Tune Speed
- High Spurious Free Dynamic Range
- Low Distortion
- Simultaneous ELINT & ESM Operation
- Frequency Selective RF Protection
- Compact, Expandable Architecture
- Low power consumption
- Optional 1GHz IF

### Applications

- Electronic Intelligence (ELINT)
- Electronic Support Measures (ESM)
- Defence Aids Systems (ECM Sw-Off)
- Combined ELINT / ESM Sensors
- Ground, Airborne & Naval Environments

### Product Description

The QR026 high performance receiver provides a new approach for ESM / ELINT applications, encompassing several features offering wide-band synthesized capability from 500MHz to 18.5GHz, with frequency extensions available up to 40 GHz. The QR026 builds on the carrier developed for the QR010 receiver family and uses a compact, monolithic module for maximum system flexibility.

The QR026 offers high pre-selection selectivity, but without the drawbacks of slow tune speeds and high DC power requirements associated with conventional YIG based receivers. Tune speeds of <125µsec are achievable over the full tuning range. Amplitude and group delay characteristics are excellent, over the full 500MHz RF bandwidth, with even higher performance over the middle 6GHz (400MHz) bandwidth. Performance over the central 100MHz is exceptional (better than 1µs group delay), offering the lowest jitter for high quality ELINT signal extension. Wave control is via front panel Ethernet, 10 / 100 Base T.

The temperature compensated unit exhibits low noise figure, high IP3 performance and consumes < 60 Watts in single channel configuration.

The modular architecture of the receiver allows it to be configured as a single, fixed, drop in used channel and with phase & amplitude matched performance across all channels. The receiver provides IF outputs at 100 and 180MHz, with user selectable IF bandwidths available. A 1GHz IF output is available on demand. The receiver can be supplied as an integrated rack or as parts for integration in a customer system.

TELEDYNE DEFENCE  
10000 WILLOW CREEK DRIVE  
CHICAGO, IL 60634  
USA  
TELE: 773 399 0000  
FAX: 773 399 0001  
WWW.TELEDYNEDEFENCE.COM

QR026 Rev. 3.2  
2011-01-01

TELEDYNE DEFENCE  
10000 WILLOW CREEK DRIVE  
CHICAGO, IL 60634  
USA  
TELE: 773 399 0000  
FAX: 773 399 0001  
WWW.TELEDYNEDEFENCE.COM



**TELEDYNE  
DEFENCE**  
A Teledyne Technologies Company

0.5 to 18GHz  
High Performance Receiver  
Technical Data QR026

### Electrical Specification

Parameter	Typical Value
*RF Input Frequency Range Optional extension to 0 - 40GHz	0.5 - 18GHz
*Maximum input CW	<150mW
*LO Frequency	<30GHz Max
*Gain 20dB typ - 660MHz IF 20dB typ - 1500MHz IF	
*Gain Variation (500MHz IF BW)	<1.5dB typ for any one frequency and any LO Signal in the IF bandwidth
*Gain Variation (any 100MHz IF BW)	<1.5dB typ
*Cross Coupling Variation (500MHz IF BW)	80dB over the normal BW BW 10dB over the full bandwidth. 3dB typ. <1ns in channel 100MHz
*Input Attenuator	20dB range typ
*RF Attenuator	15dB Max. 10dB range typ
*VSWR (RF input side)	2.5:1
*Noise Figure	10dB max (Noise Fig. 3dB)
*Noise Floor	<100dB
*Input IF	660MHz (Factory Option)
*Single Tone SFDR	80dB typ (500MHz BW)
*Intermod 2 Tone SFDR	10dB typ (500MHz BW)
*Spurious Generated Spurious	<50dB max (max. input power)
*Tune Speed	100Hz/sec - input track command by GPIB control
*Tune Accuracy	0.1Hz
*Tune Resolution	1MHz (1Hz resolution)
*Tune Noise	
1kHz	0.001mW
10kHz	0.0001mW
100kHz	0.00001mW
1MHz	0.000001mW
10MHz	0.0000001mW
*Size	100mm x 200mm (single channel)
*Total Power Consumption	<10W in full test configuration
*Input Power Supply	Typ. 250WDC, 20V - 250VAC
*Weight	<10kg
*Operating Temperature Range	-10°C to +50°C
*Options	* Frequency Extension to 40GHz * Single 100MHz or 200MHz Channel * Signal (FPGA) with 100MHz resolution * Alternative Board / Assembly Configurations * Alternative IF Outputs (100MHz, 150MHz, 200MHz) * Alternative test configurations or analogue carrier in direct mode for integration in customer test * Alternative user interface hardware

QR026 Rev. 1.0  
April 2011  
Page 2 of 4

© Teledyne Defence Ltd, 2011. All rights reserved. Datasheet may be subject to change.

Figure 55. Technical Specifications for Teledyne Defence QR026 EW Receiver.  
From [44].

## APPENDIX D. SPECIFICATION SHEET FOR POYNTING DEFENCE DF-A0062 DF RECEIVER



VERSION: 2.0



### PRODUCT DESCRIPTION:

This direction finding antenna covers a frequency range of 20 MHz to 6 GHz. A separate, but fully integrated active monitoring antenna gives high sensitivity omni-directional coverage on the same axis as the DF antenna, without interfering with the DF array.

The full-size elements on all bands give excellent DF sensitivity. Ultimate angular resolution for strong signals is well under 1° for most of the frequency range. Dipole elements provide good cross-polarisation rejection, and fair performance for signals arriving from up to 15° above or below the horizon.

The integrated monitoring antenna is in two bands, mounted above the Band C & D DF antenna module housed in the radome. Each band of the monitoring array is amplified at the top of the cable, and passively combined to give continuous coverage over the frequency range 20 MHz to 6 GHz, with a single output connector.

This DF antenna is designed to be usable with either a 5- or 2-channel phase-sensitive receiver and correlative algorithm. Characterisation of the antenna can be performed on request.

**Related products:** DF-A0064, DF-A0057-03, DF-A0038 and DF-A0066



PAGE 1 of 4

## Direction Finding and Monitoring Antenna

20 – 6000 MHz

Product Code: DF-A0062

### SPECIFICATIONS:

<b>Product codes:</b>	
DF-A0062	DF with monitoring up to 6 GHz
<b>Electrical – DF:</b>	
DF frequency range	Band A: 20 – 300 MHz; Band B: 300 – 1000 MHz; Band C: 1000 – 3000 MHz; Band D: 3000 – 6000 MHz
Nominal input impedance	50 Ω
Antenna type	5-element DF interferometer (From 5 to 2-channel receiver compatible)
Polarisation	Vertical
Output cables	RG 400 cables
DF connectors	20 x TNC male
Monitoring connector	1 x N male
<b>Electrical – monitoring:</b>	
Frequency range	20 – 6000 MHz
Nominal H-plane beamwidth	360°
Nominal E-plane beamwidth	90°
Typical VSWR*	2:1
Polarisation	Vertical
Connector type	N-type male
Nominal impedance	50 Ω
Input voltage (via coax)*	13 – 24 V DC
Input current*	< 150 mA
Power consumption (nom)*	< 2.25 W
OP1dB (typ.)†	≥ 11 dBm
OP2 (typ.)†	≥ 31 dBm
OP3 (typ.)†	≥ 21 dBm
Sensitivity (typ.)	20 – 100 MHz 100 – 1000 MHz
(S/N = 10 dB, BW = 1 Hz)†	–20 dBµV/m –30 dBµV/m
	1 – 3 GHz 3 – 6 GHz
	–35 dBµV/m –40 dBµV/m
<b>Mechanical:</b>	
Cross-sectional wind area	1.50 m² (including antenna switch)
Maximum wind speed	160 km/h (without ice load)
Assembled height	3.60 m
Assembled diameter (max)	2.70 m
Shipping dimensions	2.20 m x 0.90 m x 0.60 m
Weight of antenna	60 kg
Weight including shipping container	135 kg

\* In active mode

### ELECTRICAL FEATURES:

- Full-size DF
- Wideband DF
- 5-element interferometer
- Optimised for 2-channel receivers
- High sensitivity omni antenna integrated
- Tactical rapid deploy/stow design with integrated dust caps

### MECHANICAL FEATURES:

- Designed for tower mounting

defence@poynting.co.za  
www.poyntingdefence.com

Poynting Antennas has a policy of continuous development and future specifications may change without notice.

**DEFENCE AND  
SPECIALISED**

Figure 56. Technical Specifications for Poynting Defence DF A0062 DF Receiver. From [45].

THIS PAGE INTENTIONALLY LEFT BLANK

## APPENDIX E. DETECTION COVERAGE PLOTS FOR TARGET PLANE IN S-BAND

Referring to detection coverage for the plate at  $0^\circ$  and  $180^\circ$  orientations in Figure 57 and Figure 58, respectively, received SNR is the greatest when the transmission and reception of the target plane echo occurs in the vicinity of the target plane faces (at  $90^\circ$  and  $270^\circ$  RCS mainlobes) and minimum when transmission and reception occurs at the edges of the plate ( $0^\circ$  and  $180^\circ$ ). Similar observations were made for detection coverage for target plane at  $90^\circ$  and  $-90^\circ$  orientation (Figure 59 and Figure 60).

Comparing the detection coverage for a plate at a  $45^\circ$  orientation with different transmitter positions in Figure 61 and Figure 62, it is evident that different transmitter-receiver geometry can result in similar detection coverage. The target position with the greatest SNR is observed when either transmission or reception LOS falls in the vicinity of the plate faces. Similar observations were made for a plate at a  $-45^\circ$  orientation (Figure 63 and Figure 64).

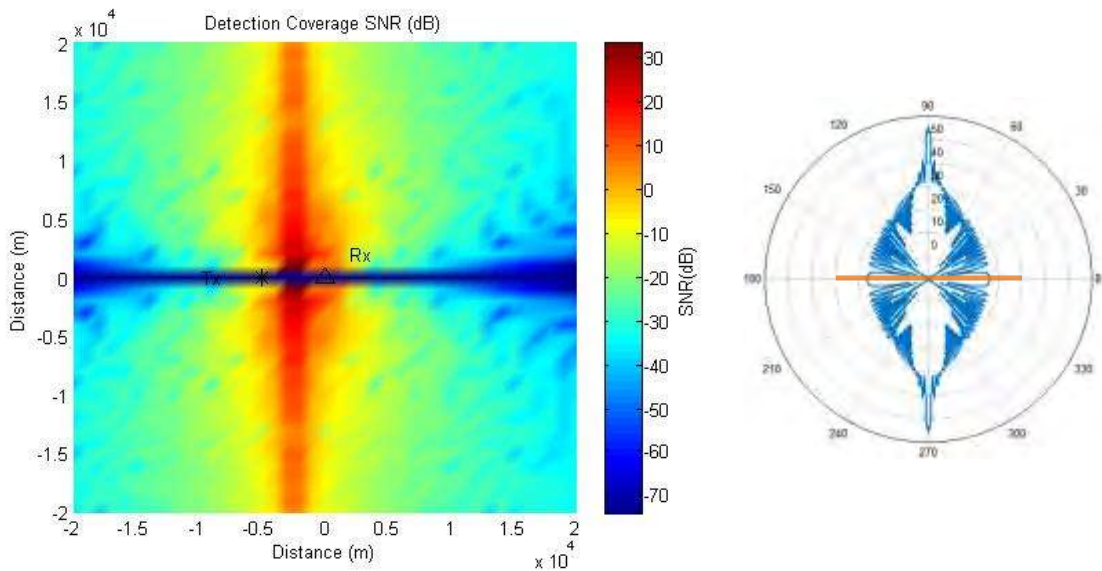


Figure 57. Detection coverage (left) for Tx at  $[-5000, 0]$  and target plate at  $0^\circ$  orientation with corresponding S-band bistatic RCS (right).



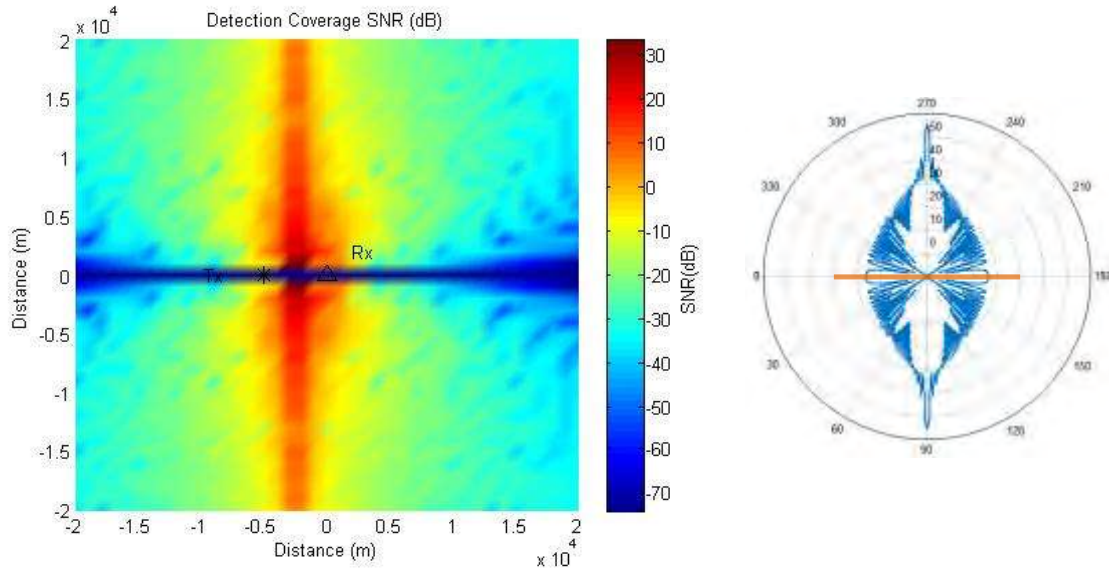


Figure 58. Detection coverage (left) for Tx at [-5000, 0] and target plate at 0° orientation with corresponding S-band bistatic RCS (right).

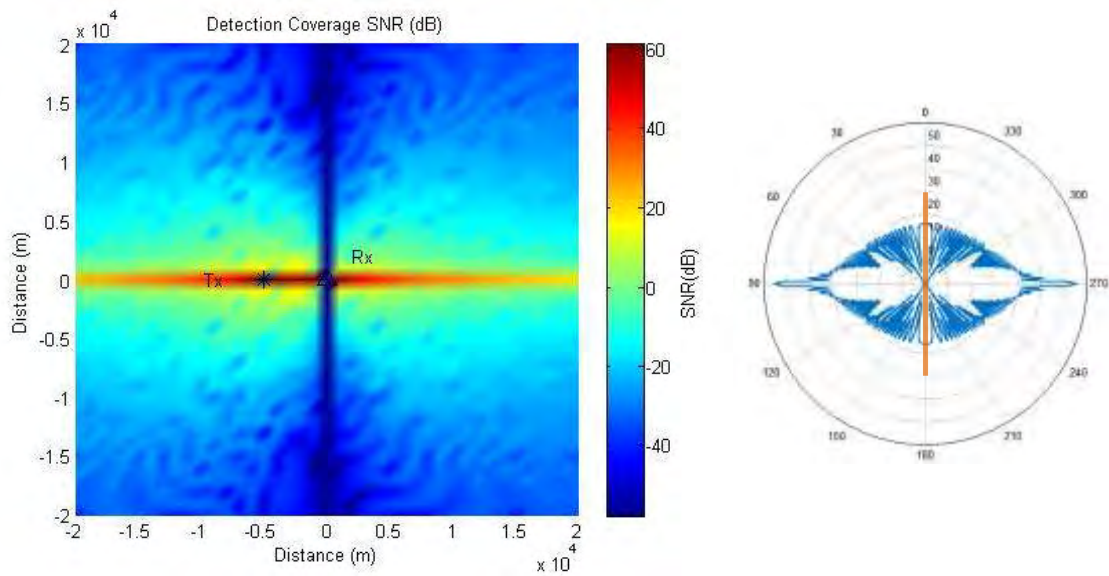


Figure 59. Detection coverage (left) for Tx at [-5000, 0] and target plate at 90° orientation with corresponding S-band bistatic RCS (right).

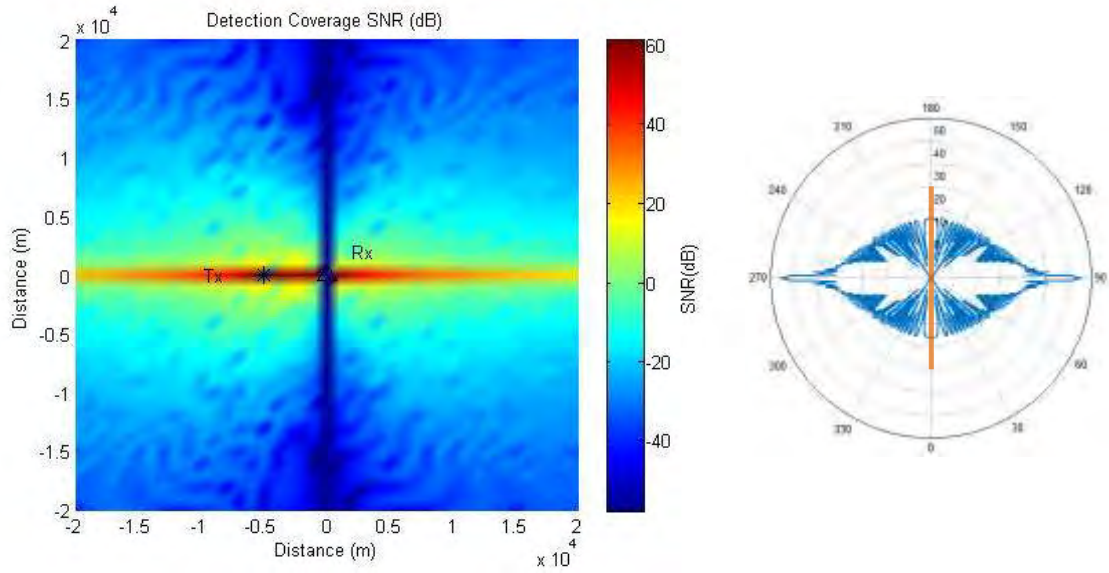


Figure 60. Detection coverage (left) for Tx at  $[-5000, 0]$  and target plate at  $-90^\circ$  orientation with corresponding S-band bistatic RCS (right).

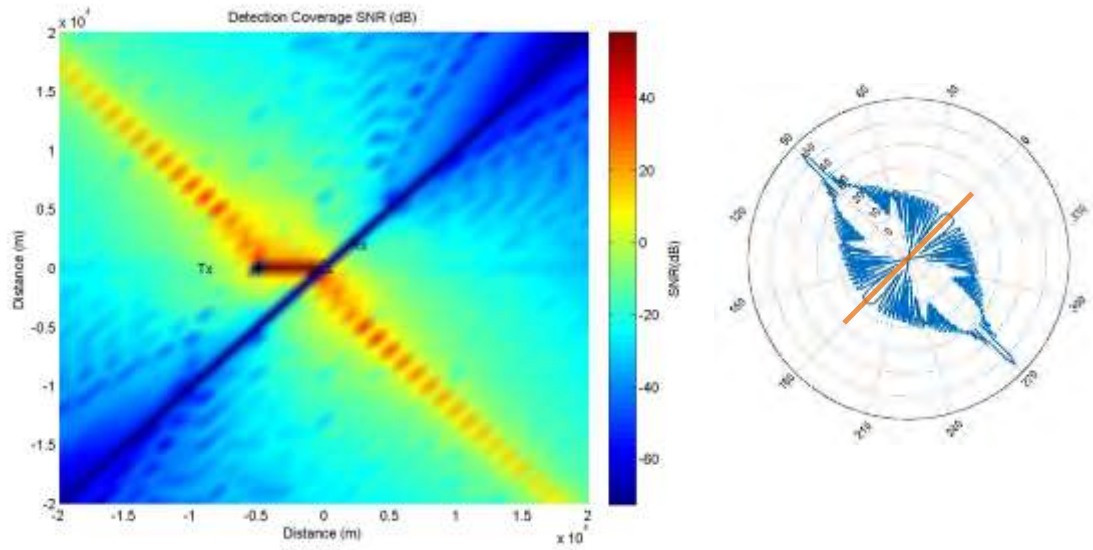


Figure 61. Detection coverage (left) for Tx at  $[-5000, 0]$  and target plate at  $45^\circ$  orientation with corresponding S-band bistatic RCS (right).

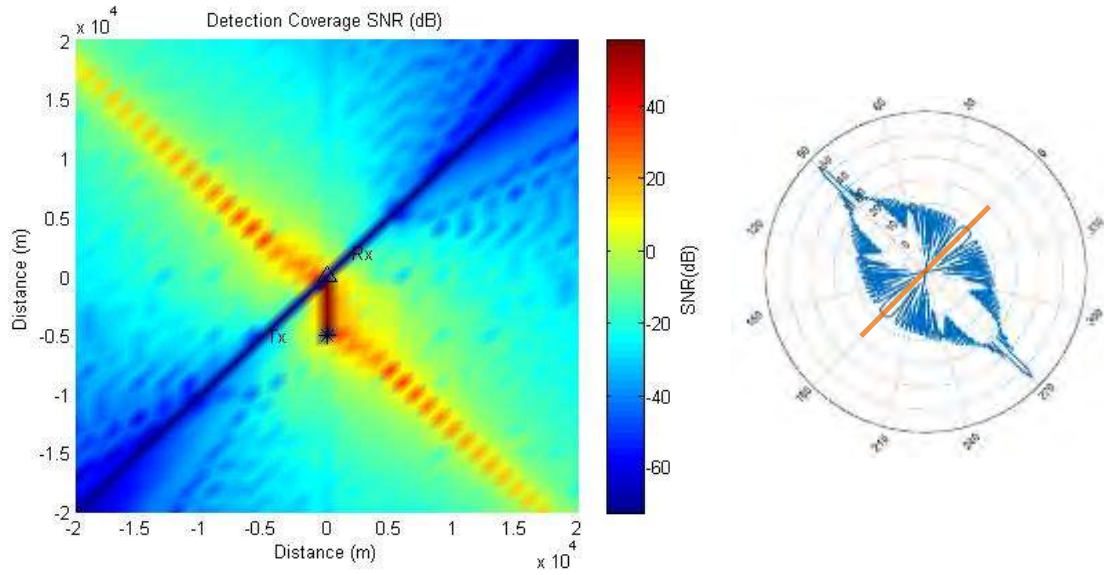


Figure 62. Detection coverage (left) for Tx at  $[0, 5000]$  and target plate at  $45^\circ$  orientation with corresponding S-band bistatic RCS (right).

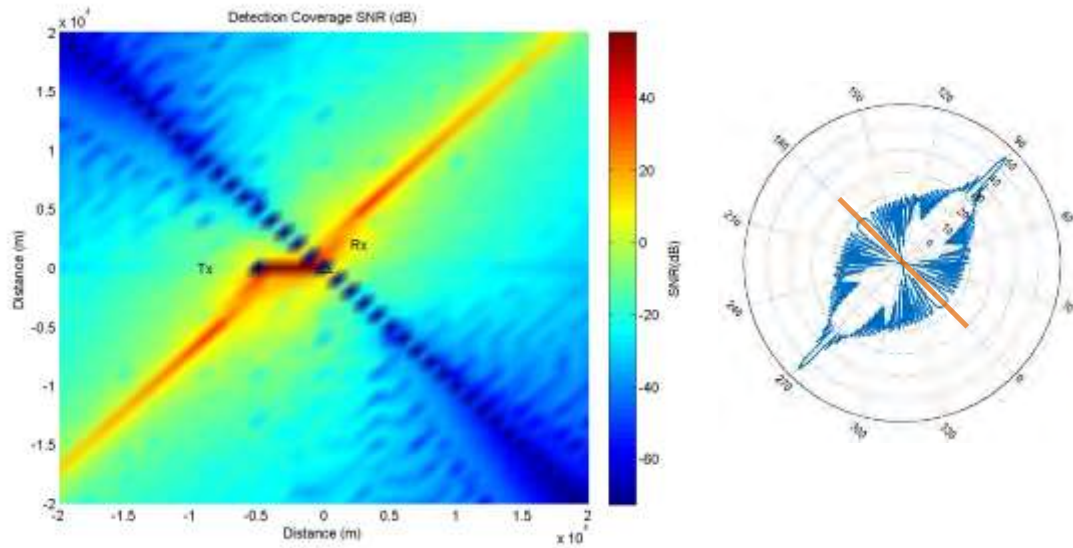


Figure 63. Detection coverage (left) for Tx at  $[-5000, 0]$  and target plate at  $-45^\circ$  orientation with corresponding S-band bistatic RCS (right).



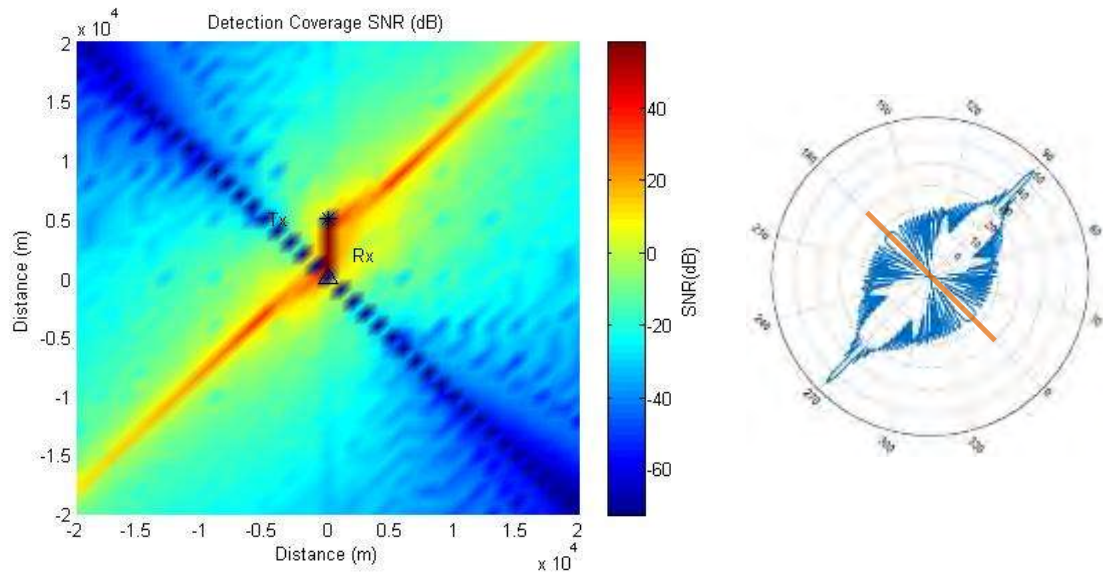


Figure 64. Detection coverage (left) for Tx at [0, 5000] and target plane at  $-45^\circ$  orientation with corresponding S-band bistatic RCS (right).

THIS PAGE INTENTIONALLY LEFT BLANK

## APPENDIX F. DETECTION COVERAGE RESULTS

### F.1 VARY NUMBER OF TRANSMITTERS

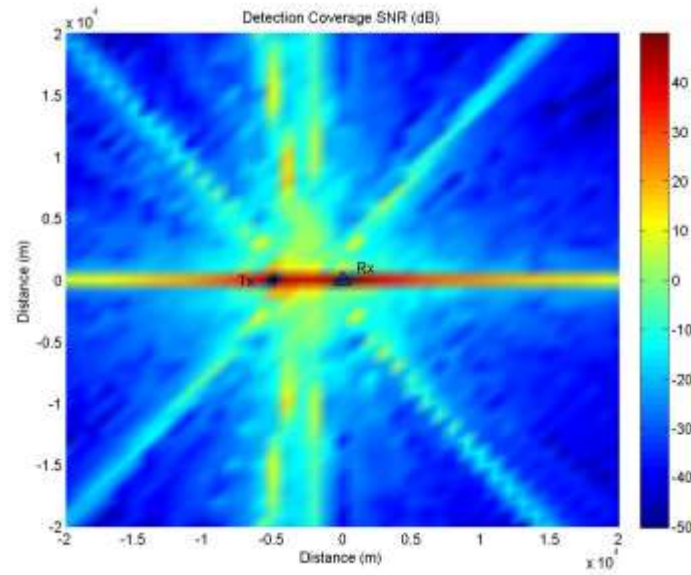


Figure 65. Detection coverage at S-Band for 1 Tx at 5 km range and target at  $0^\circ$  orientation.

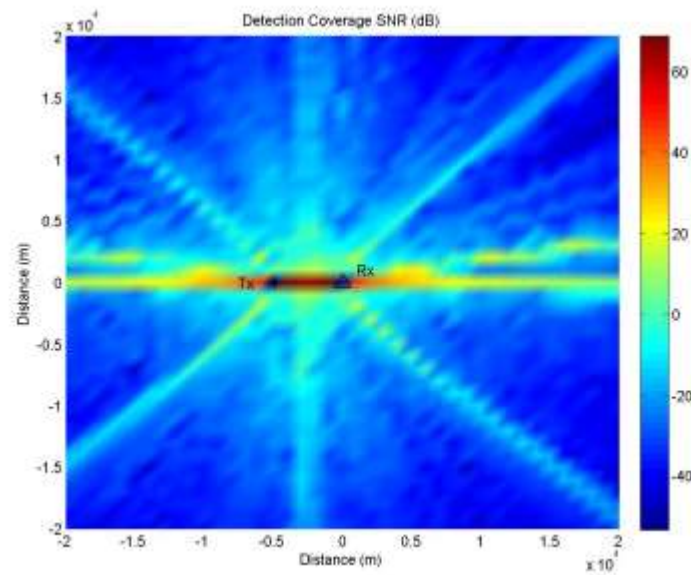


Figure 66. Detection coverage at S-Band for 1 Tx at 5 km range and target at  $-90^\circ$  orientation.

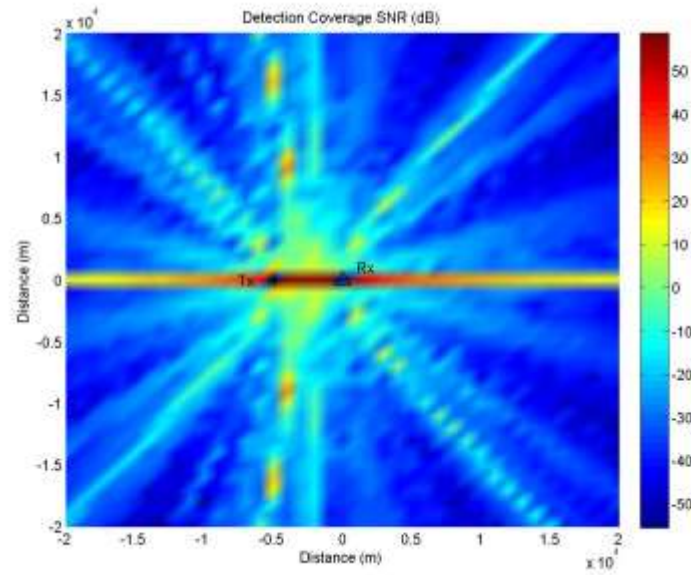


Figure 67. Detection coverage at X-Band for 1 Tx at 5 km range and target at  $0^\circ$  orientation.

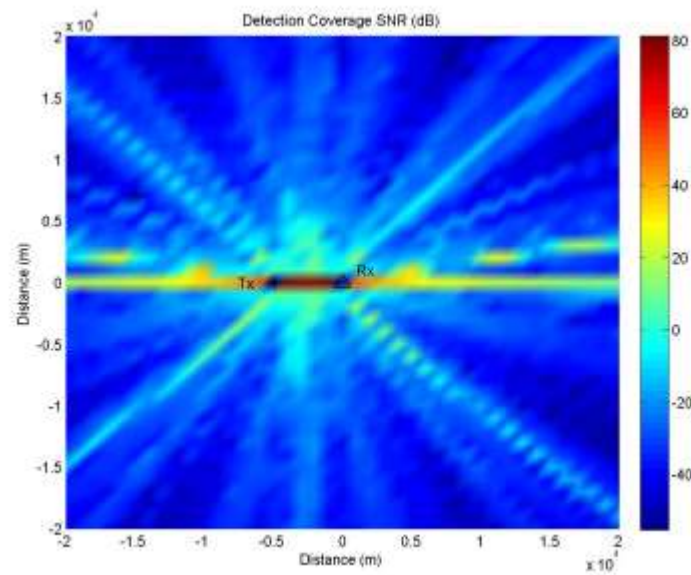


Figure 68. Detection coverage at X-Band for 1 Tx at 5 km range and target at  $-90^\circ$  orientation.

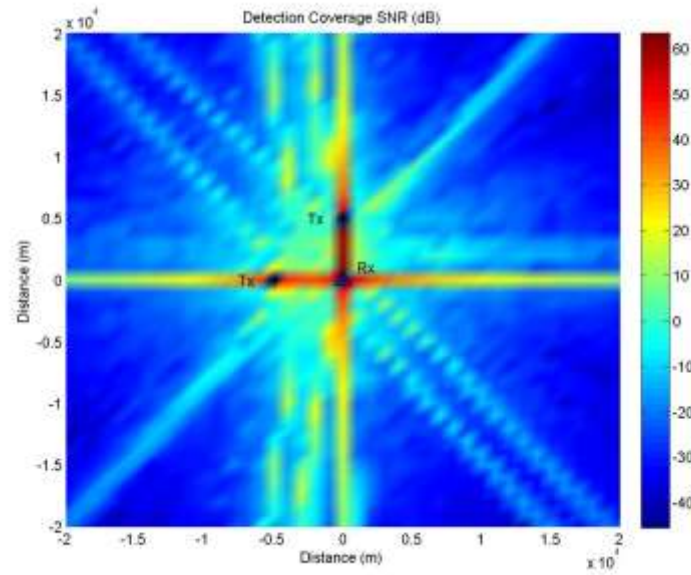


Figure 69. Detection coverage at S-Band for 2 Tx at 5 km range and target at  $0^\circ$  orientation.

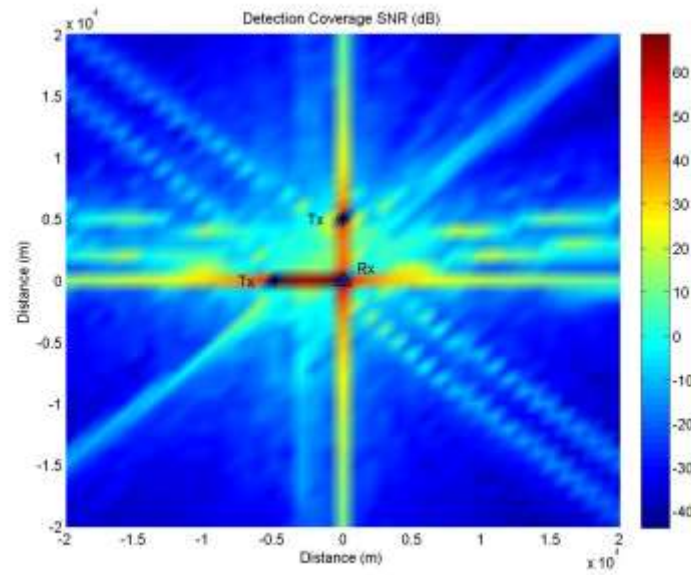


Figure 70. Detection coverage at S-Band for 2 Tx at 5 km range and target at  $-90^\circ$  orientation.

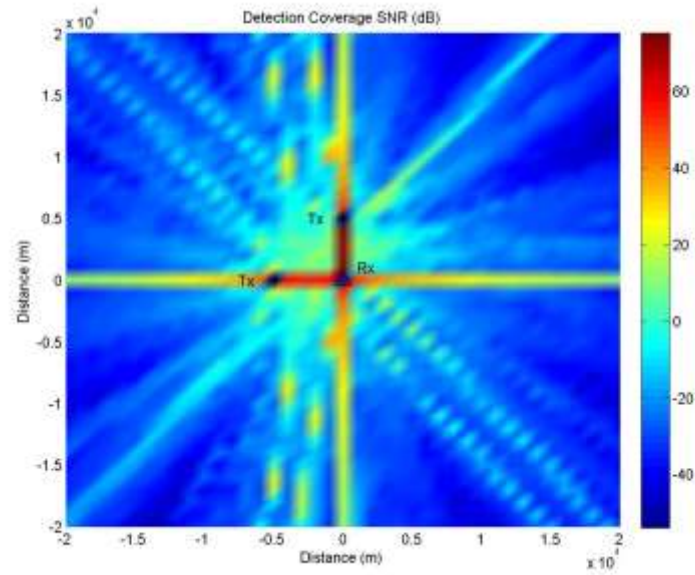


Figure 71. Detection coverage at X-Band for 2 Tx at 5 km range and target at  $0^\circ$  orientation.

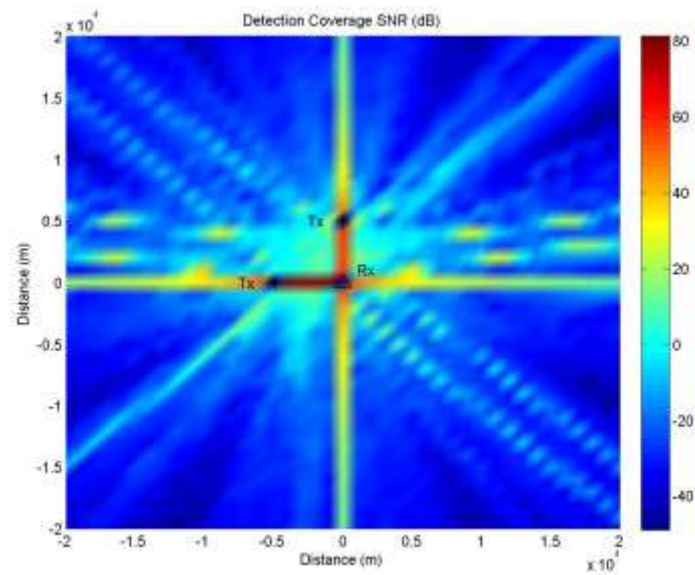


Figure 72. Detection coverage at X-Band for 2 Tx at 5 km range and target at  $-90^\circ$  orientation.



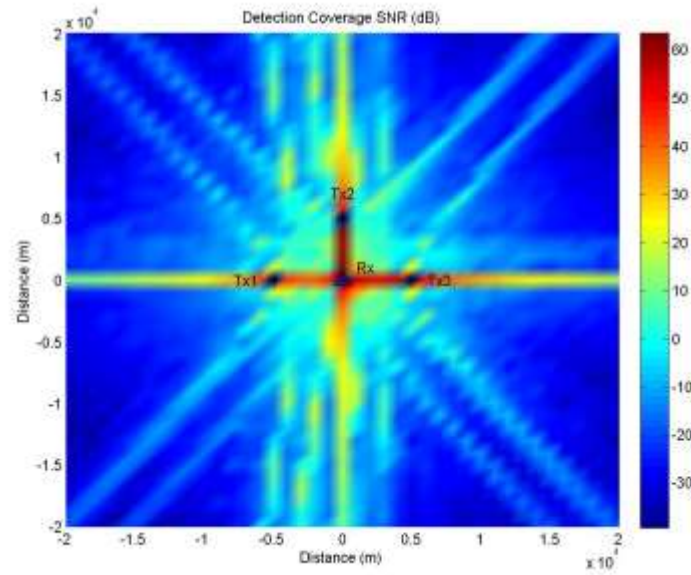


Figure 73. Detection coverage at S-Band for 3 Tx at 5 km range and target at  $0^\circ$  orientation.

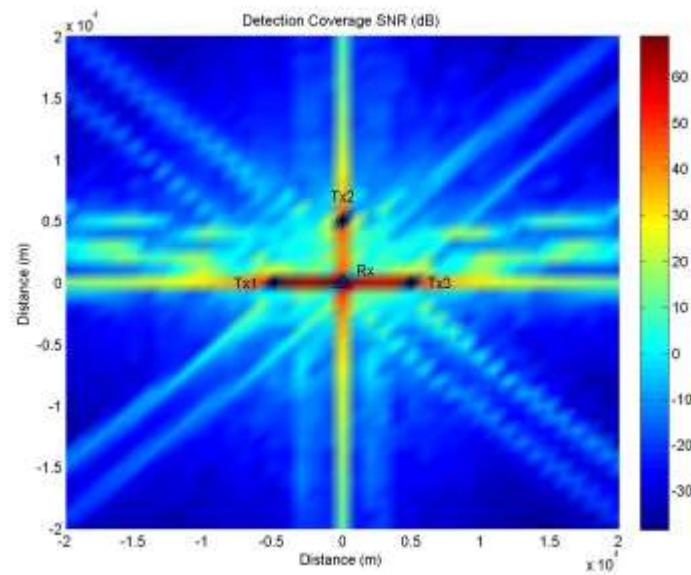


Figure 74. Detection coverage at S-Band for 3 Tx at 5 km range and target at  $-90^\circ$  orientation.

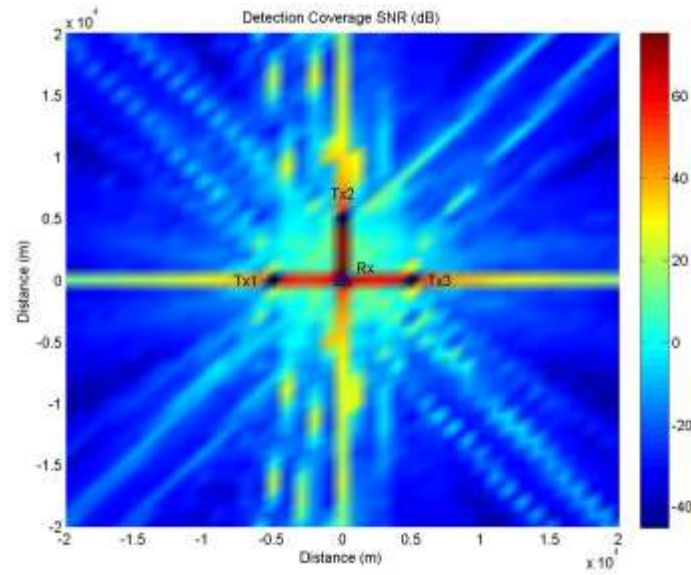


Figure 75. Detection coverage at X-Band for 3 Tx at 5 km range and target at  $0^\circ$  orientation.

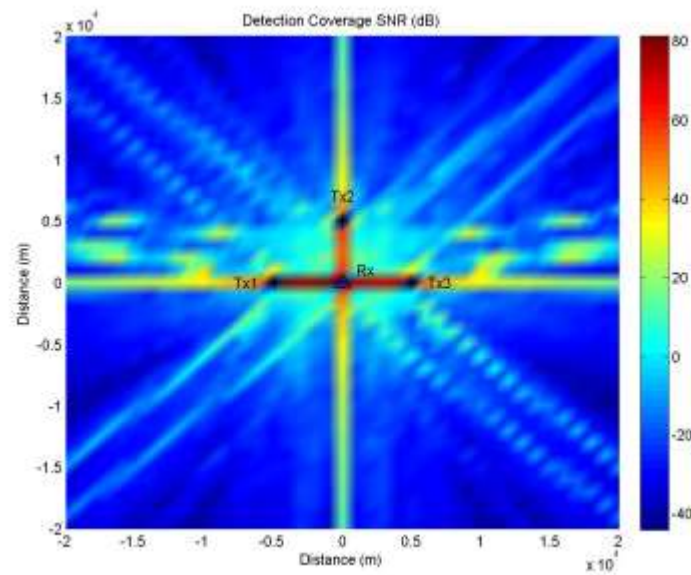


Figure 76. Detection coverage at X-Band for 3 Tx at 5 km range and target at  $-90^\circ$  orientation.



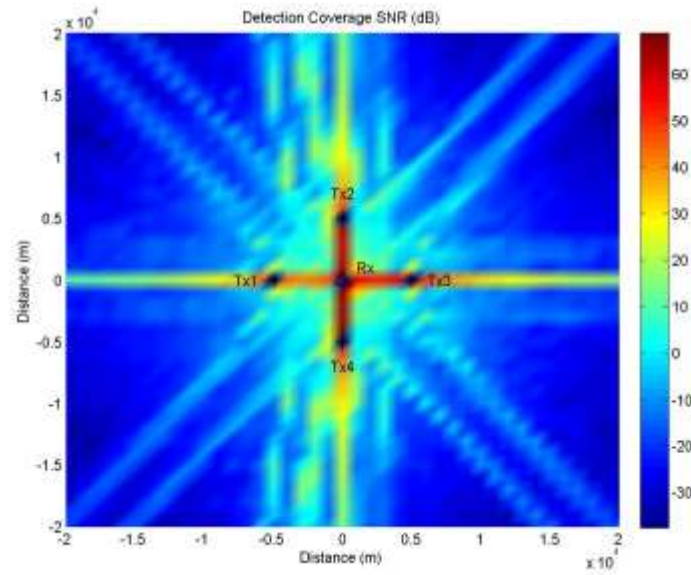


Figure 77. Detection coverage at S-Band for 4 Tx at 5 km range and target at  $0^\circ$  orientation.

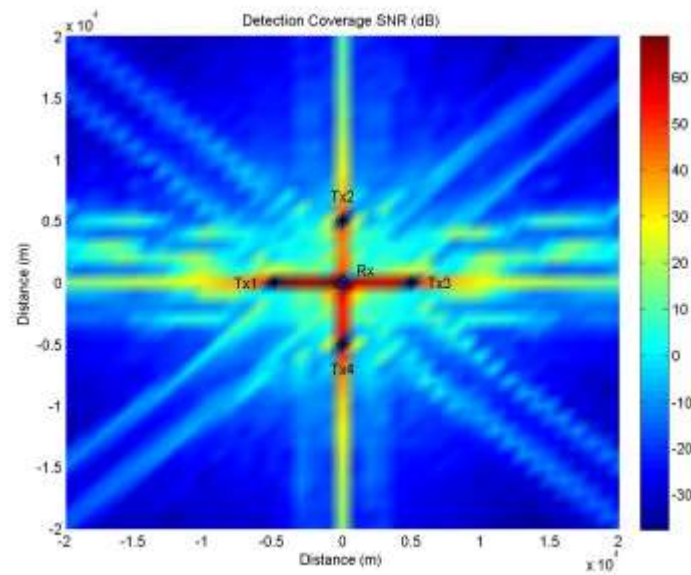


Figure 78. Detection coverage at S-Band for 4 Tx at 5 km range and target at  $-90^\circ$  orientation.

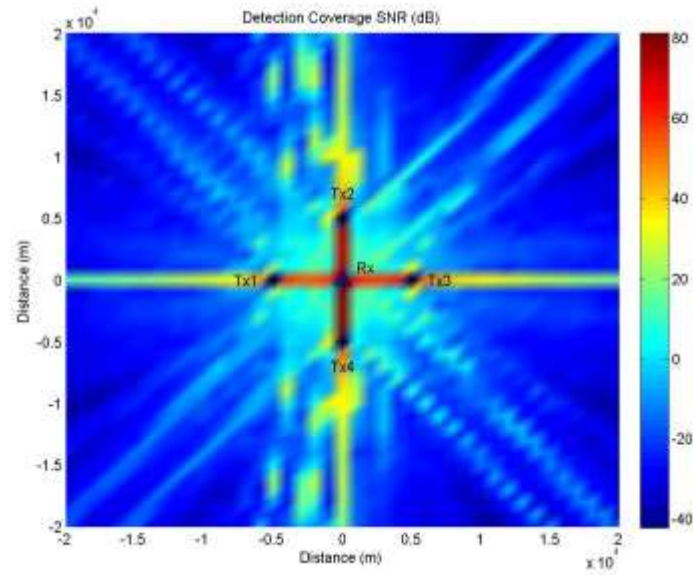


Figure 79. Detection coverage at X-Band for 4 Tx at 5 km range and target at  $0^\circ$  orientation.

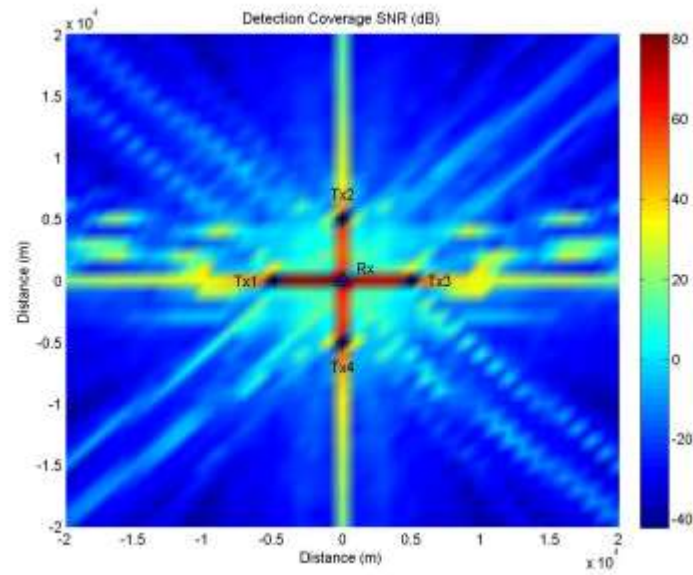


Figure 80. Detection coverage at X-Band for 4 Tx at 5 km range and target at  $-90^\circ$  orientation.

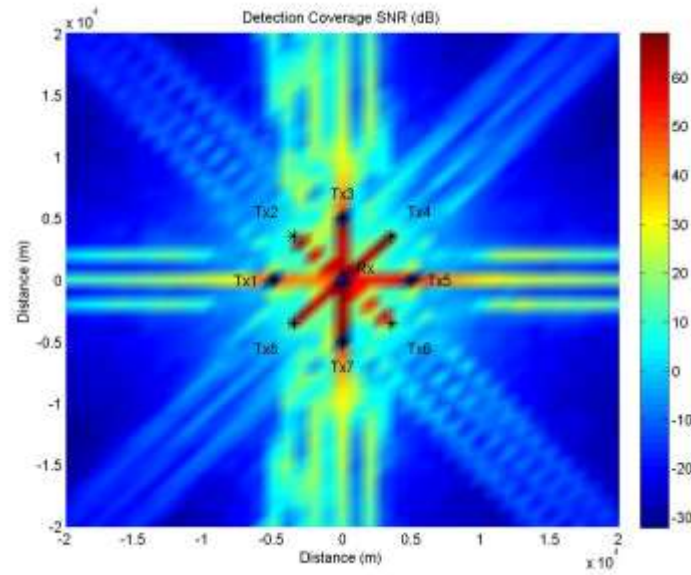


Figure 81. Detection coverage at S-Band for 8 Tx at 5 km range and target at  $0^\circ$  orientation.

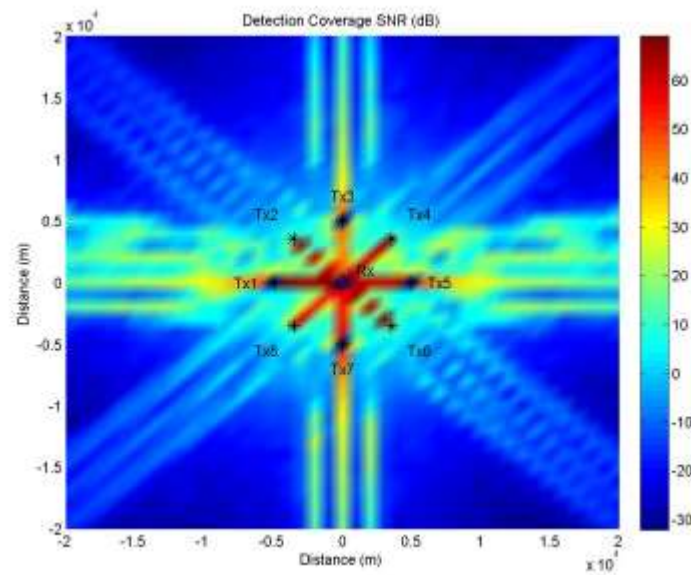


Figure 82. Detection coverage at S-Band for 8 Tx at 5 km range and target at  $-90^\circ$  orientation.

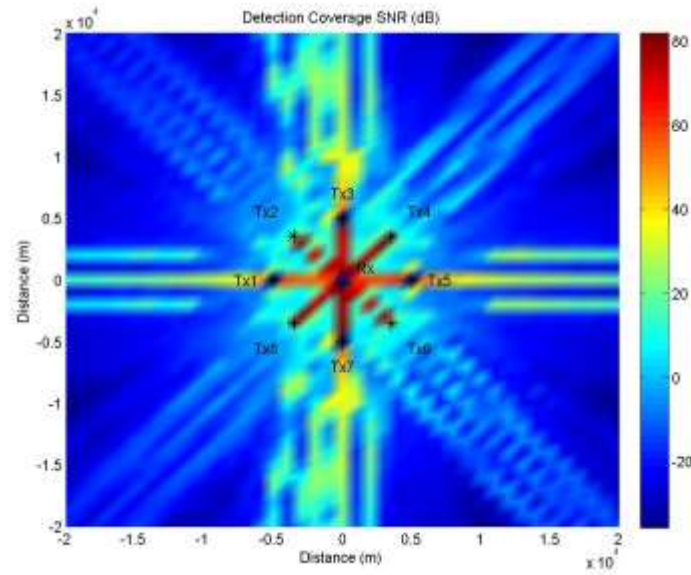


Figure 83. Detection coverage at X-Band for 8 Tx at 5 km range and target at  $0^\circ$  orientation.

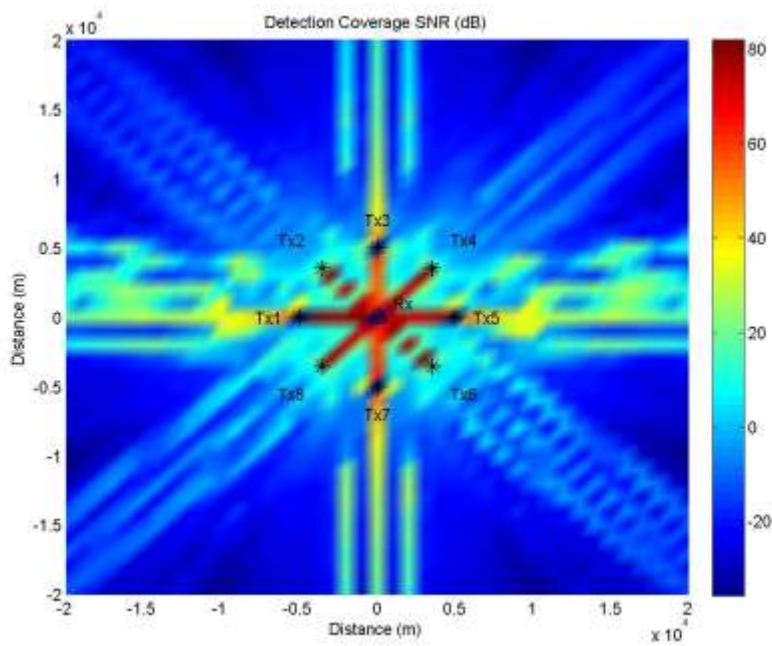


Figure 84. Detection coverage at X-Band for 8 Tx at 5 km range and target at  $-90^\circ$  orientation.

## F.2 VARY TRANSMITTER RANGE

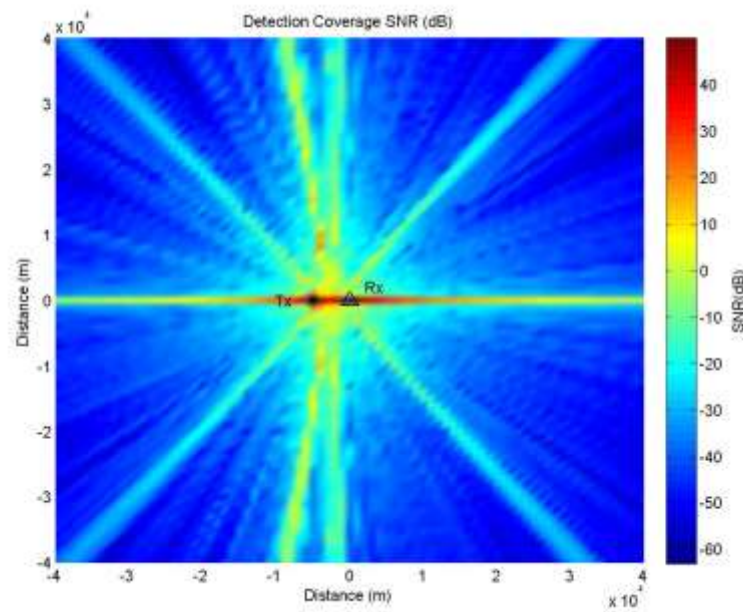


Figure 85. Detection coverage at S-Band for 1 Tx at 5 km range and target at 0° orientation.

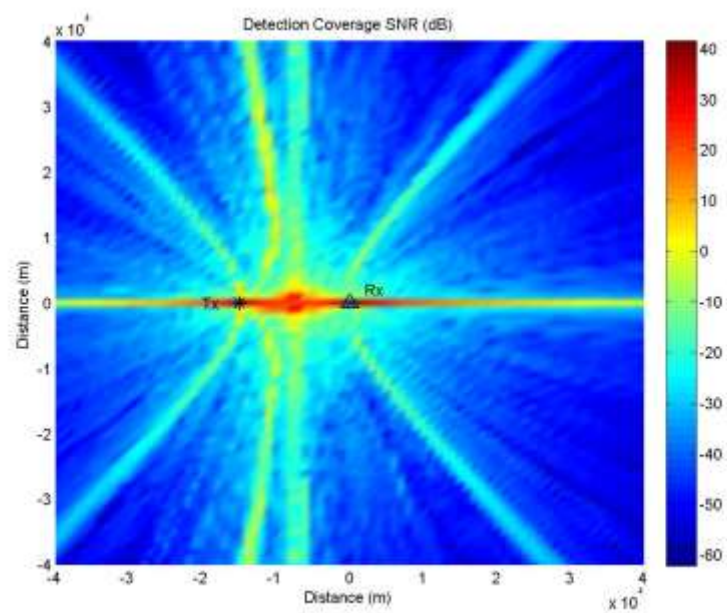


Figure 86. Detection coverage at S-Band for 1 Tx at 15 km range and target at 0° orientation.



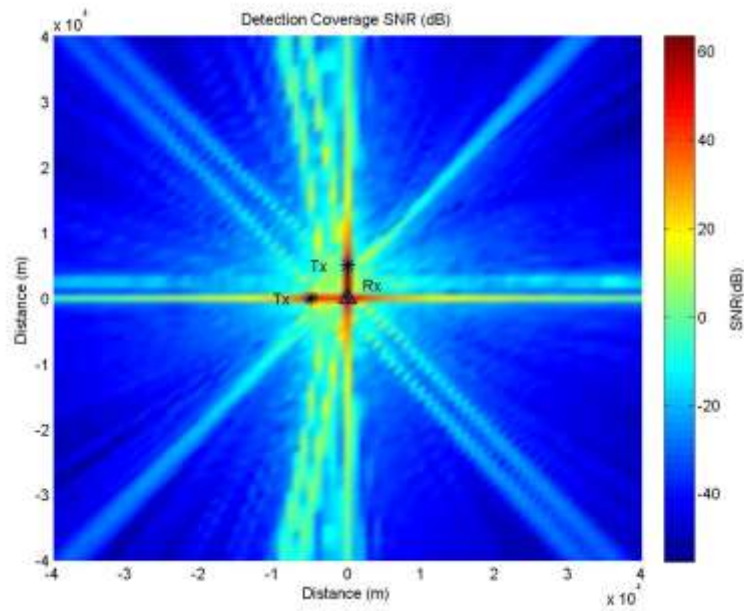


Figure 87. Detection coverage at S-Band for 2 Tx at 5 km range and target at  $0^\circ$  orientation.

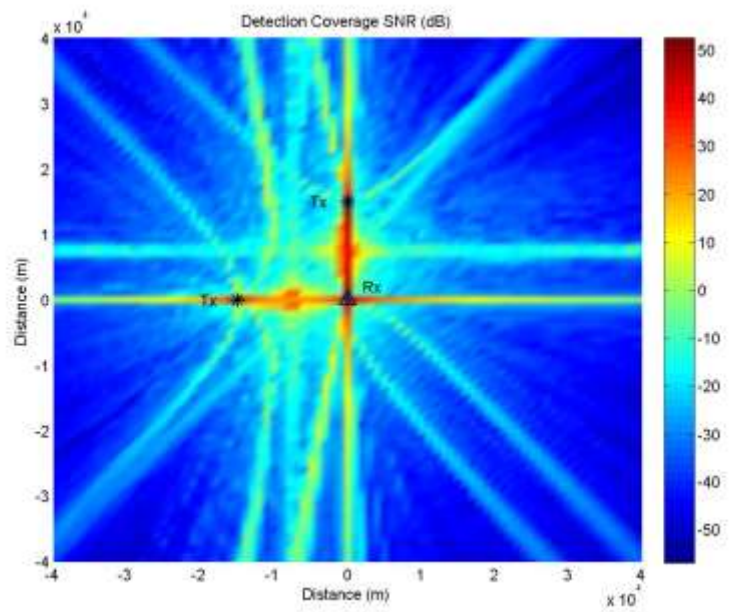


Figure 88. Detection coverage at S-Band for 2 Tx at 15 km range and target at  $0^\circ$  orientation.

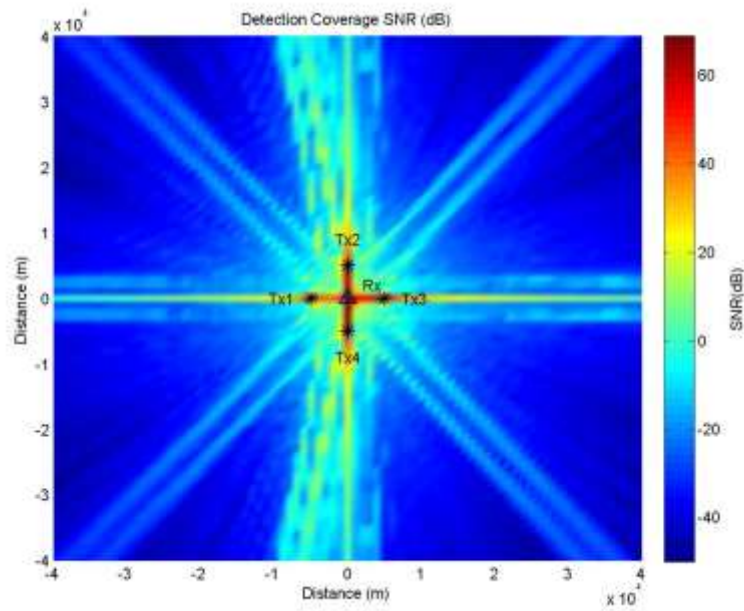


Figure 89. Detection coverage at S-Band for 4 Tx at 5 km range and target at  $0^\circ$  orientation.

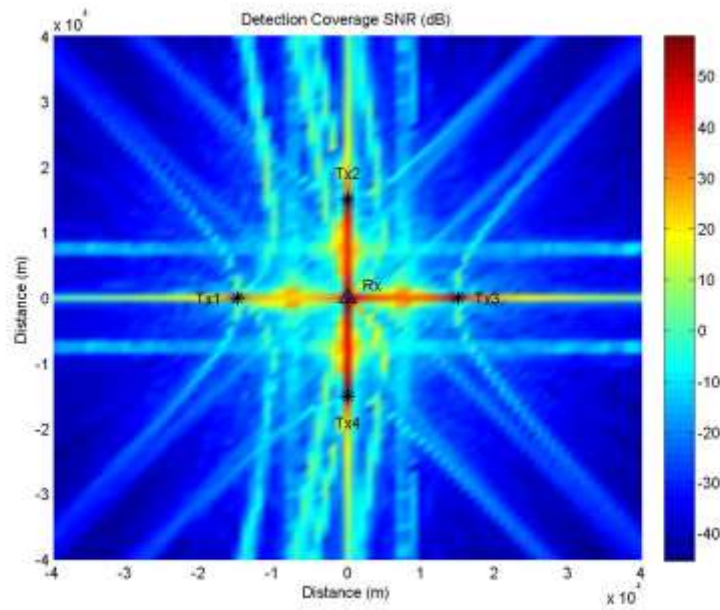


Figure 90. Detection coverage at S-Band for 4 Tx at 15 km range and target at  $0^\circ$  orientation.

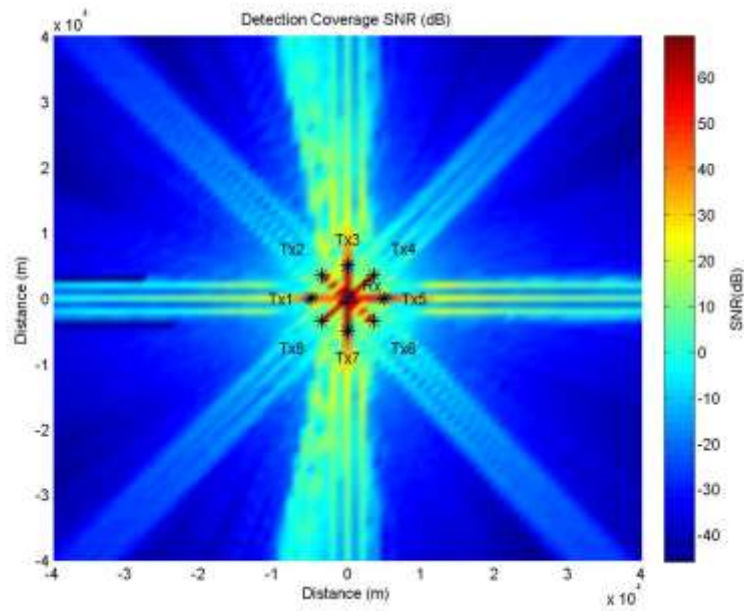


Figure 91. Detection coverage at S-Band for 8 Tx at 5 km range and target at  $0^\circ$  orientation.

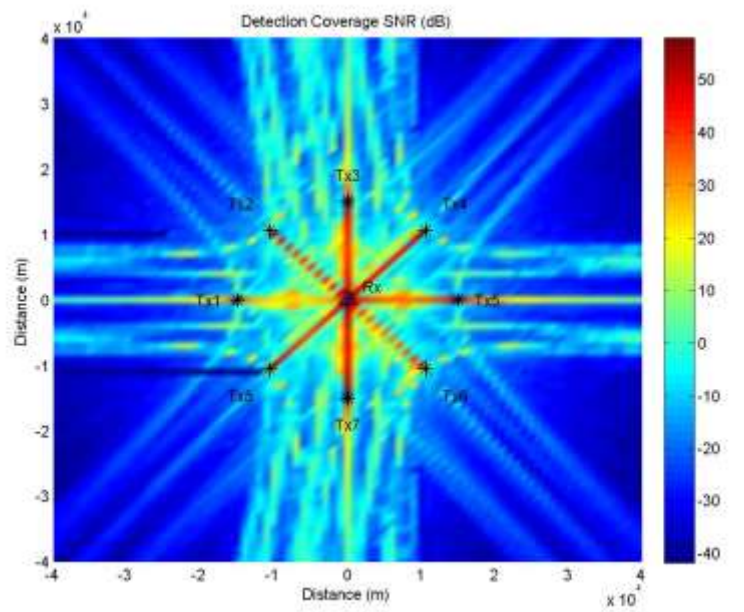


Figure 92. Detection coverage at S-Band for 8 Tx at 15 km range and target at  $0^\circ$  orientation.



### F.3 VARY TRANSMITTER-TARGET-RECEIVER GEOMETRY

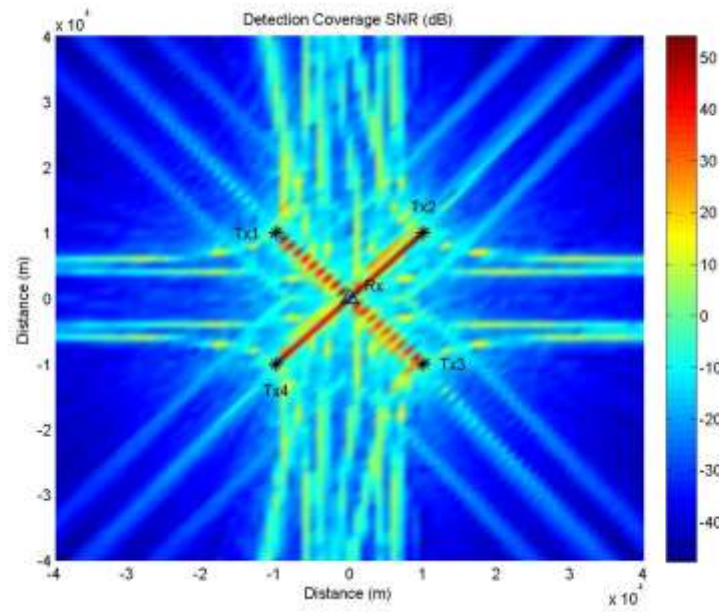


Figure 93. Detection coverage at S-Band for 4 Tx in receiver-centered geometry and target at 0° orientation.

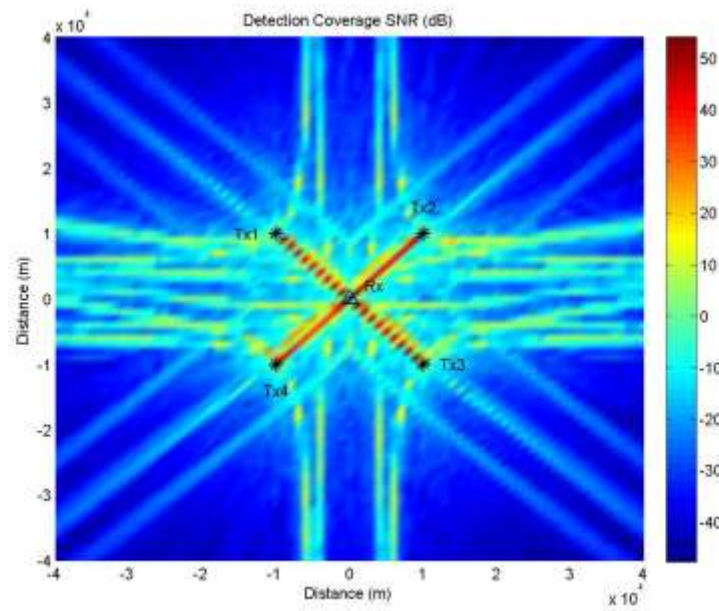


Figure 94. Detection coverage at S-Band for 4 Tx in receiver-centered geometry and target at -90° orientation.

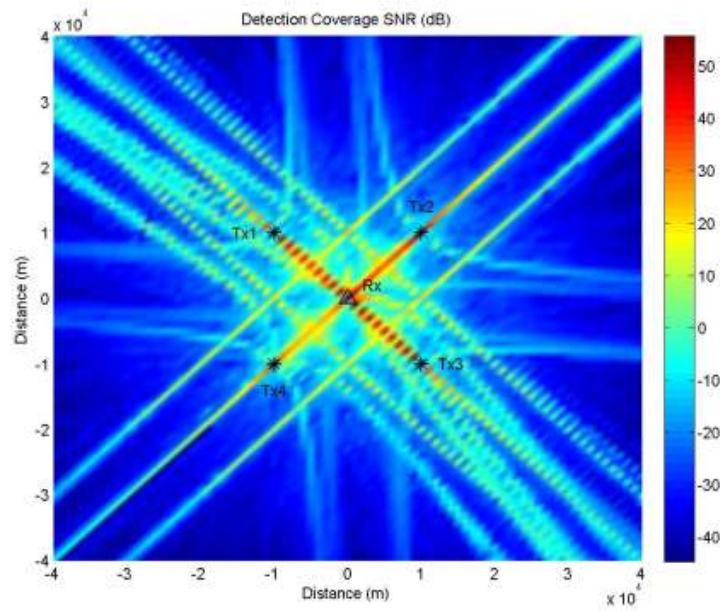


Figure 95. Detection coverage at S-Band for 4 Tx in receiver-centered geometry and target at  $45^\circ$  orientation.

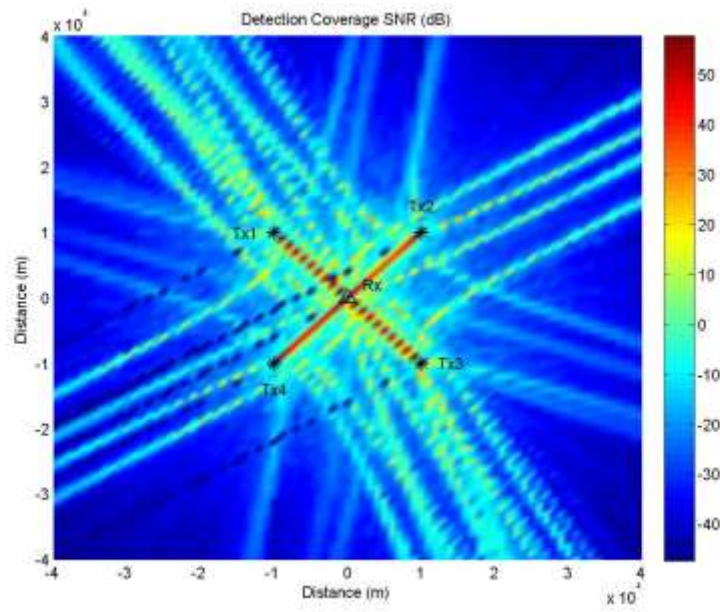


Figure 96. Detection coverage at S-Band for 4 Tx in receiver-centered geometry and target at  $30^\circ$  orientation.

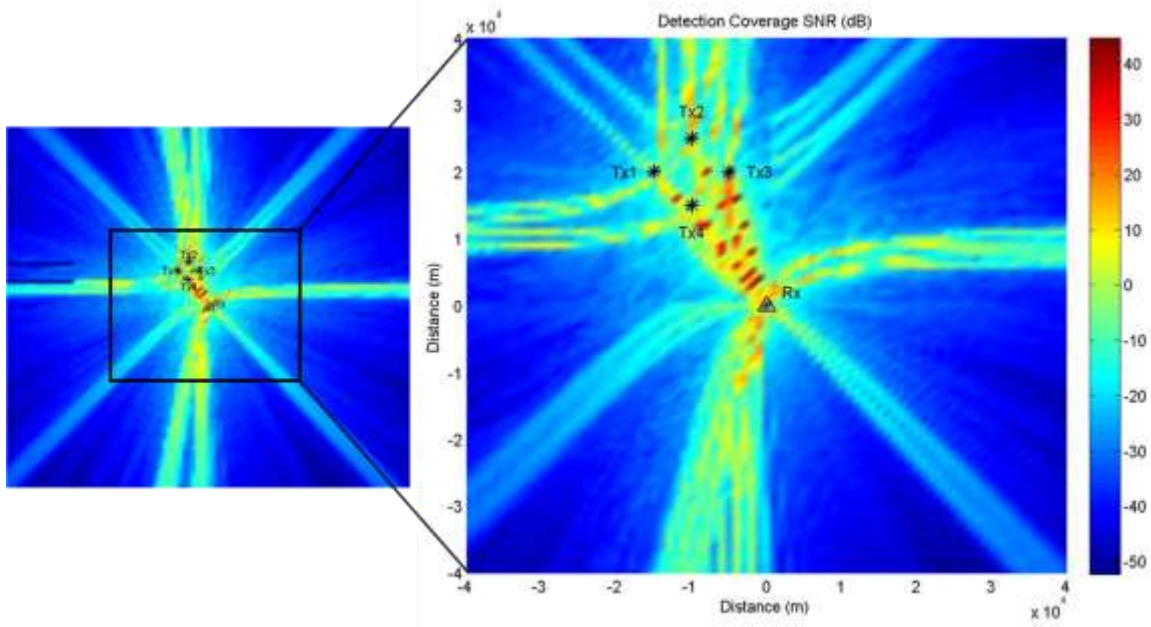


Figure 97. Detection coverage at S-Band for 4 Tx in transmitter-clustered geometry and target at  $0^\circ$  orientation.

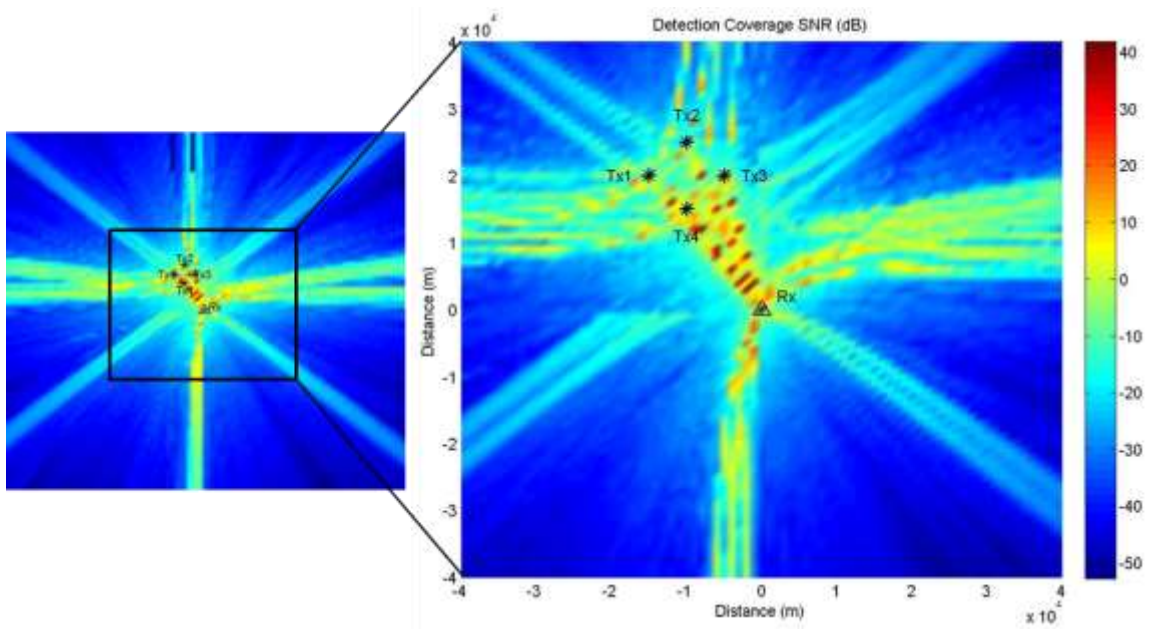


Figure 98. Detection coverage at S-Band for 4 Tx in transmitter-clustered geometry and target at  $-90^\circ$  orientation.



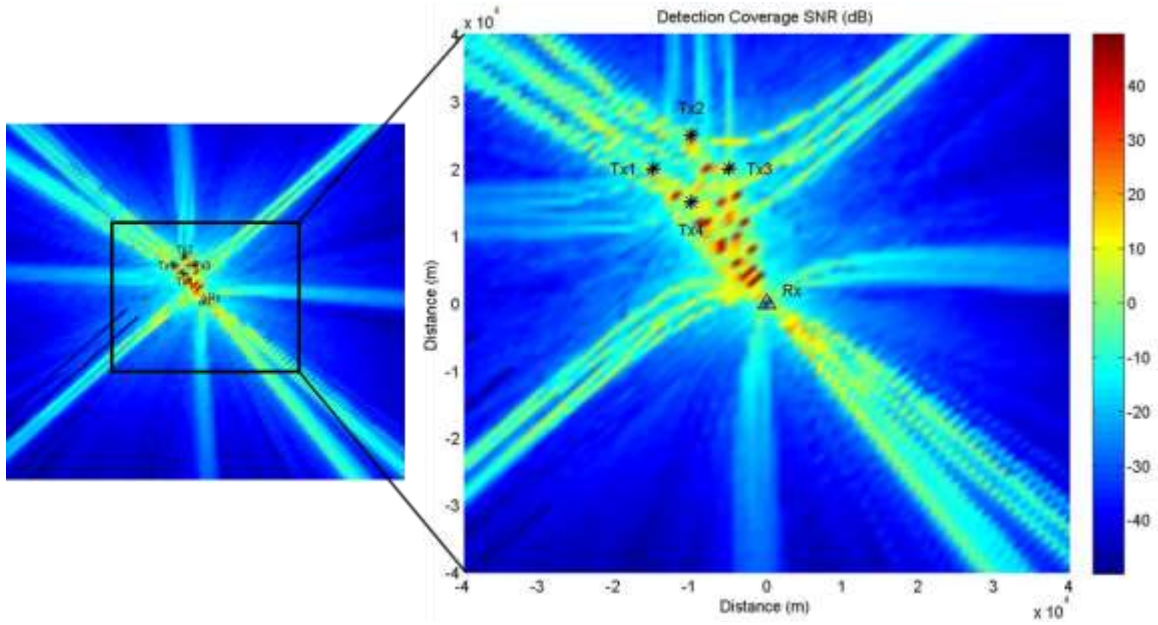


Figure 99. Detection coverage at S-Band for 4 Tx in transmitter-clustered geometry and target at  $45^\circ$  orientation.

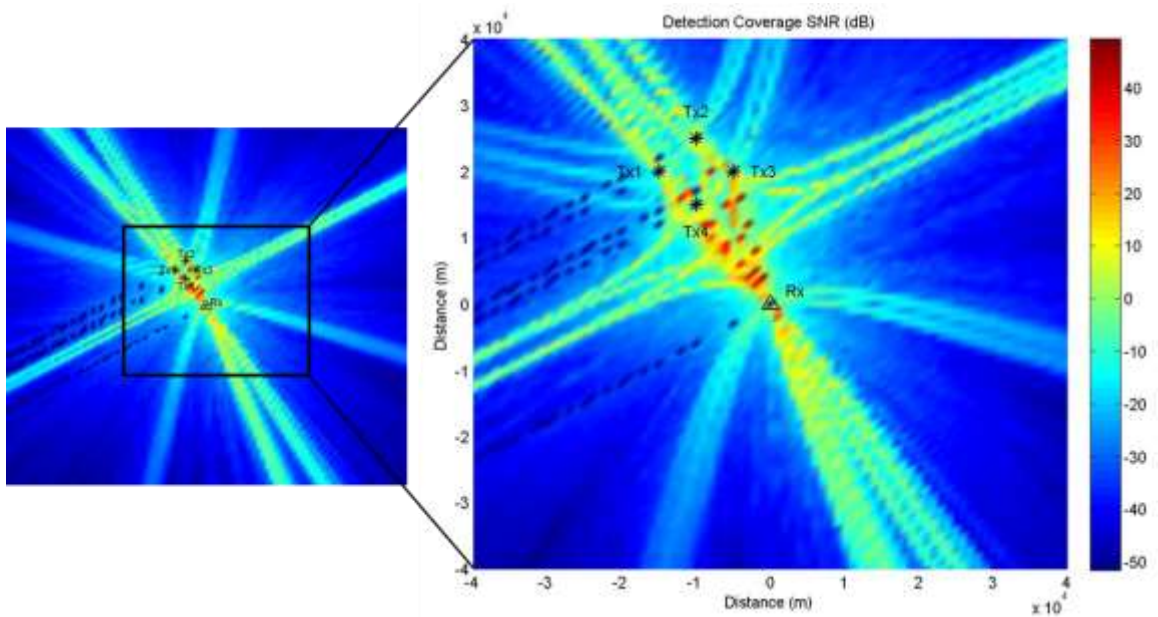


Figure 100. Detection coverage at S-Band for 4 Tx in transmitter-clustered geometry and target at  $30^\circ$  orientation.

#### F.4 RANDOMLY DISTRIBUTED TRANSMITTERS

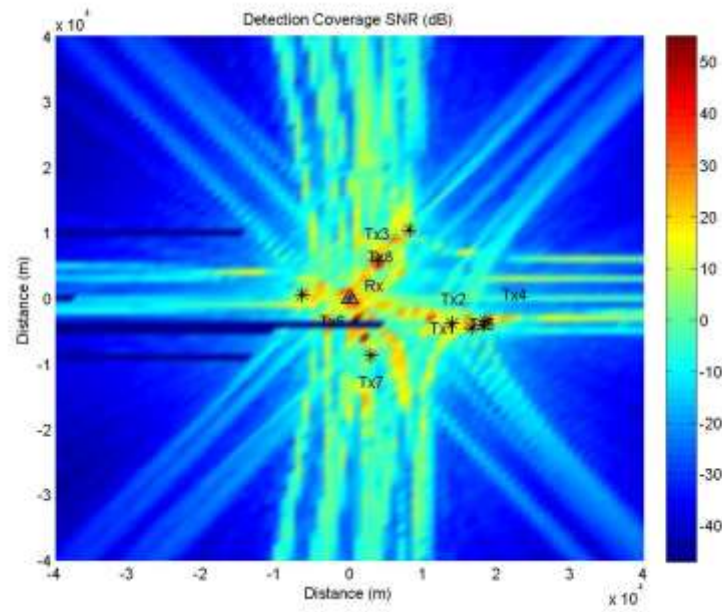


Figure 101. Detection coverage at S-Band for 8 Tx randomly positioned around Rx at 5–20 km range and target at  $0^\circ$  orientation.

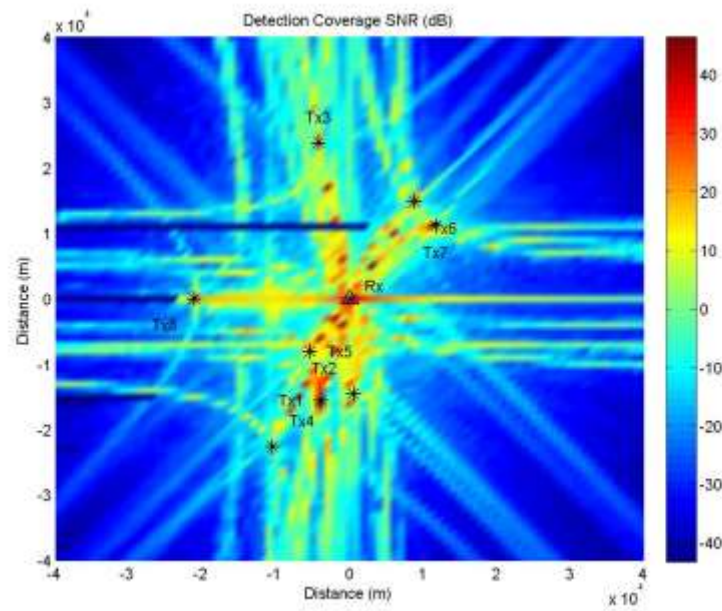


Figure 102. Detection coverage at S-Band for 8 Tx randomly positioned around Rx at 5–30 km range and target at  $0^\circ$  orientation.

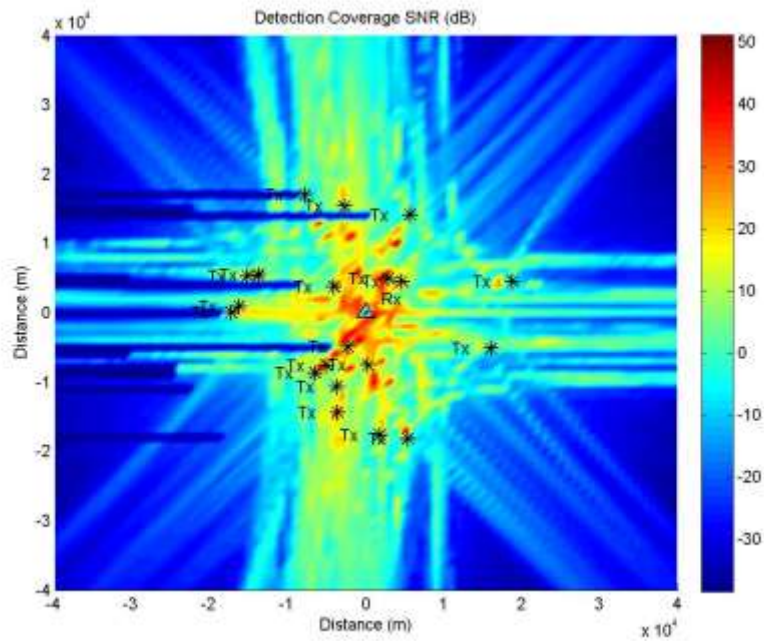


Figure 103. Detection coverage at S-Band for 20 Tx randomly positioned around Rx at 5–20 km range and target at  $0^\circ$  orientation.

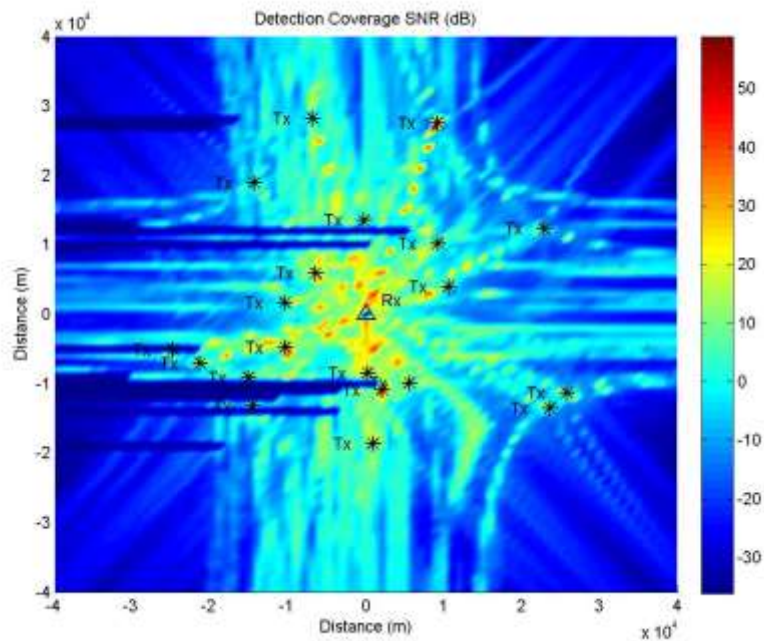


Figure 104. Detection coverage at S-Band for 20 Tx randomly positioned around Rx at 5–30 km range and target at  $0^\circ$  orientation.



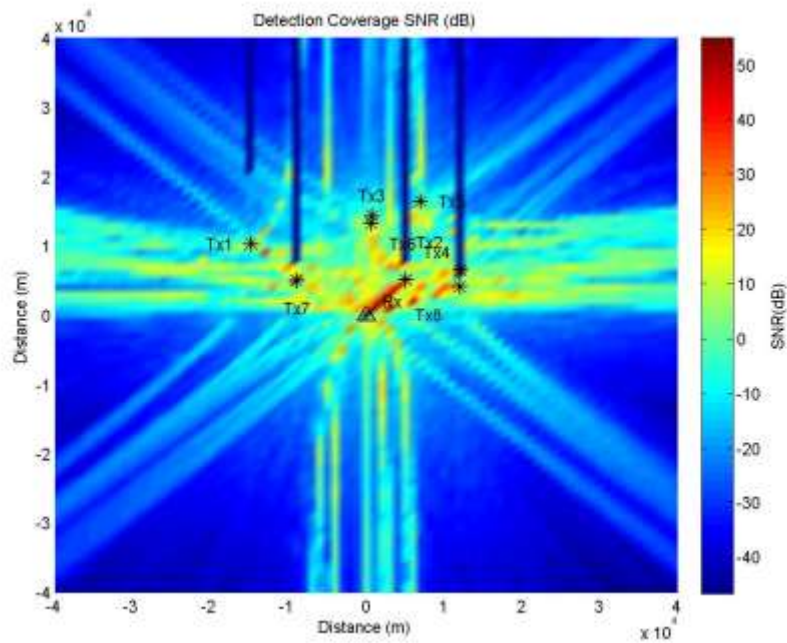


Figure 105. Detection coverage at S-Band for 8 Tx randomly positioned around Rx at 5–20 km range and target at  $-90^\circ$  orientation.

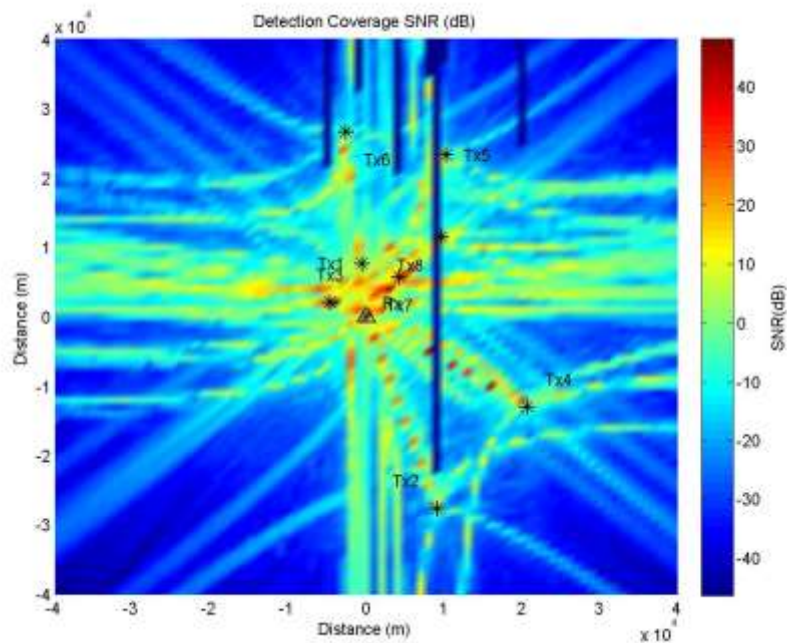


Figure 106. Detection coverage at S-Band for 8 Tx randomly positioned around Rx at 5–30 km range and target at  $-90^\circ$  orientation.

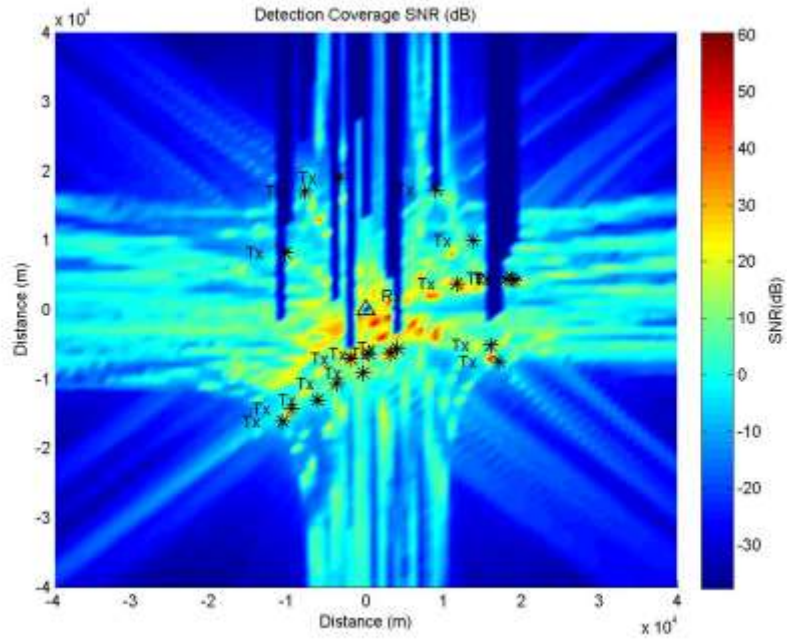


Figure 107. Detection coverage at S-Band for 20 Tx randomly positioned around Rx at 5–20 km range and target at  $-90^\circ$  orientation.

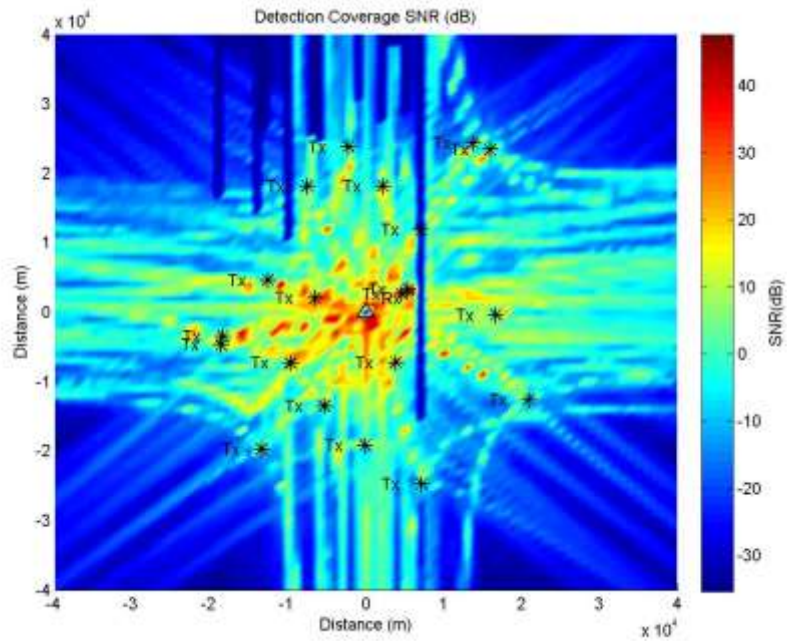


Figure 108. Detection coverage at S-Band for 20 Tx randomly positioned around Rx at 5–30 km range and target at  $-90^\circ$  orientation.



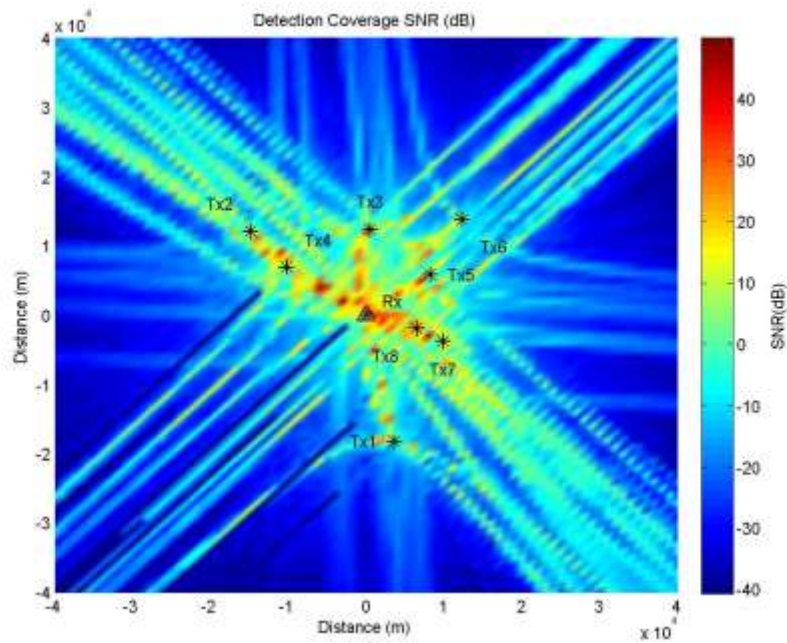


Figure 109. Detection coverage at S-Band for 8 Tx randomly positioned around Rx at 5–20 km range and target at 45° orientation.

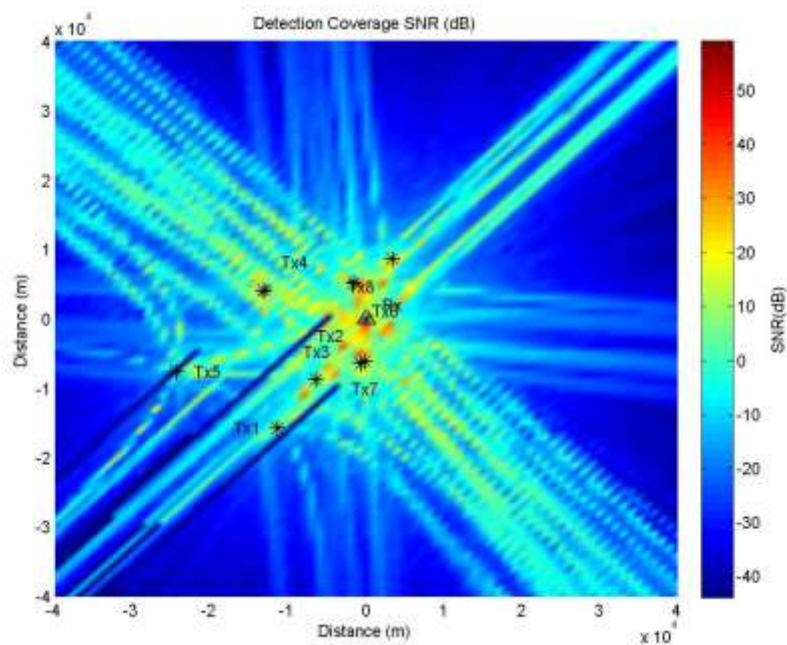


Figure 110. Detection coverage at S-Band for 8 Tx randomly positioned around Rx at 5–30 km range and target at 45° orientation.

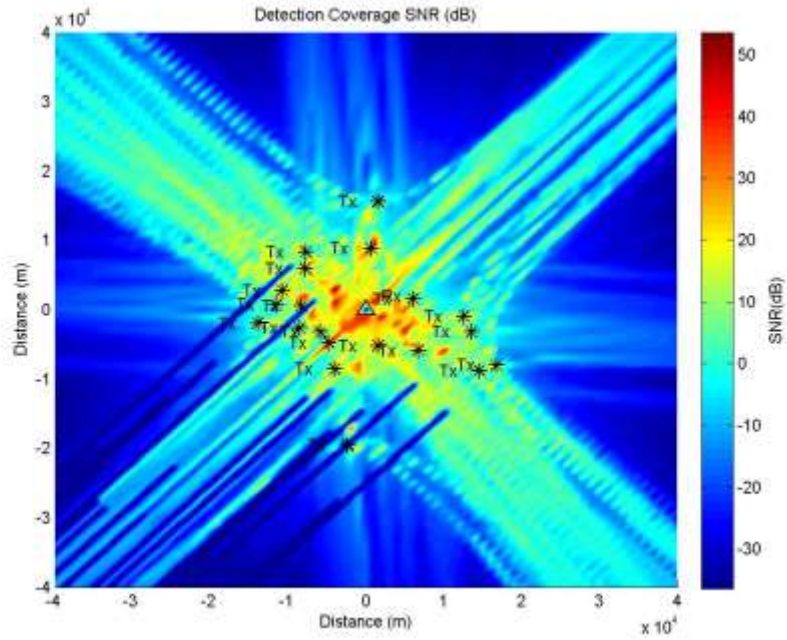


Figure 111. Detection coverage at S-Band for 20 Tx randomly positioned around Rx at 5–20 km range and target at 45° orientation.

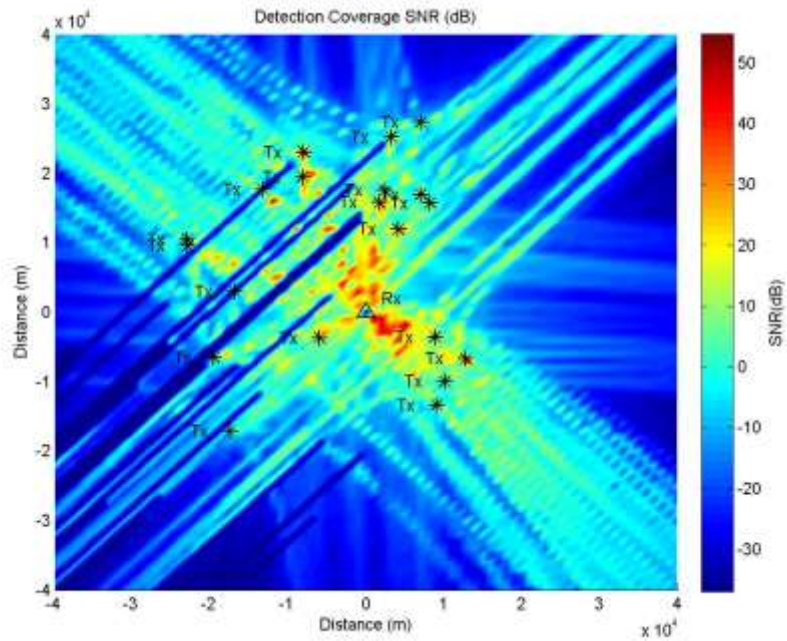


Figure 112. Detection coverage at S-Band for 20 Tx randomly positioned around Rx at 5–30 km range and target at 45° orientation.

## APPENDIX G. TARGET PATH DETECTION RESULTS

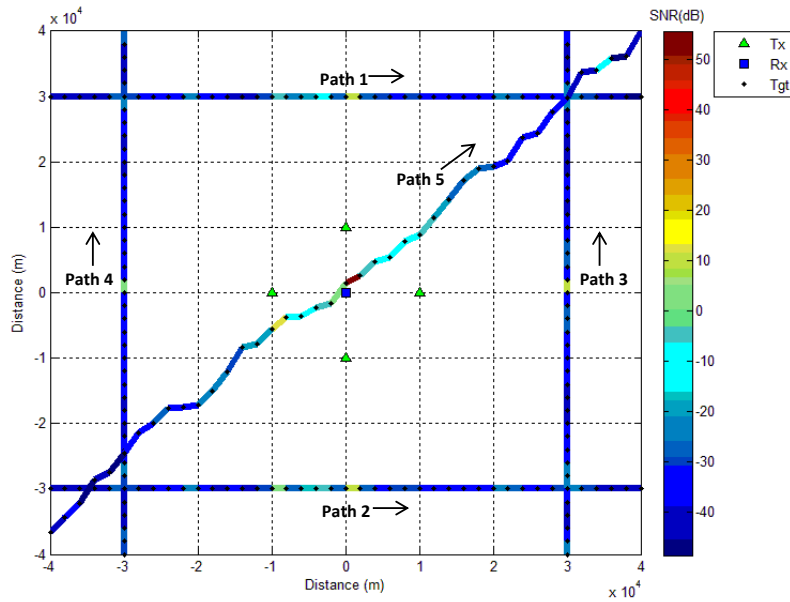


Figure 113. Detection coverage along target's path (2 km resolution) at S-Band for 4 Tx. RCS computed by calling FEKO.

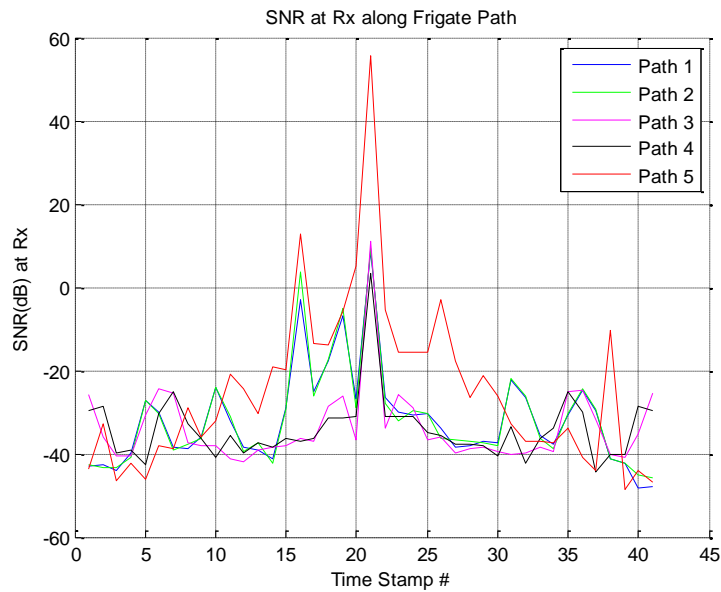


Figure 114. SNR at receiver along target's path (2 km resolution) at S-Band for 4 Tx. RCS computed by calling FEKO.

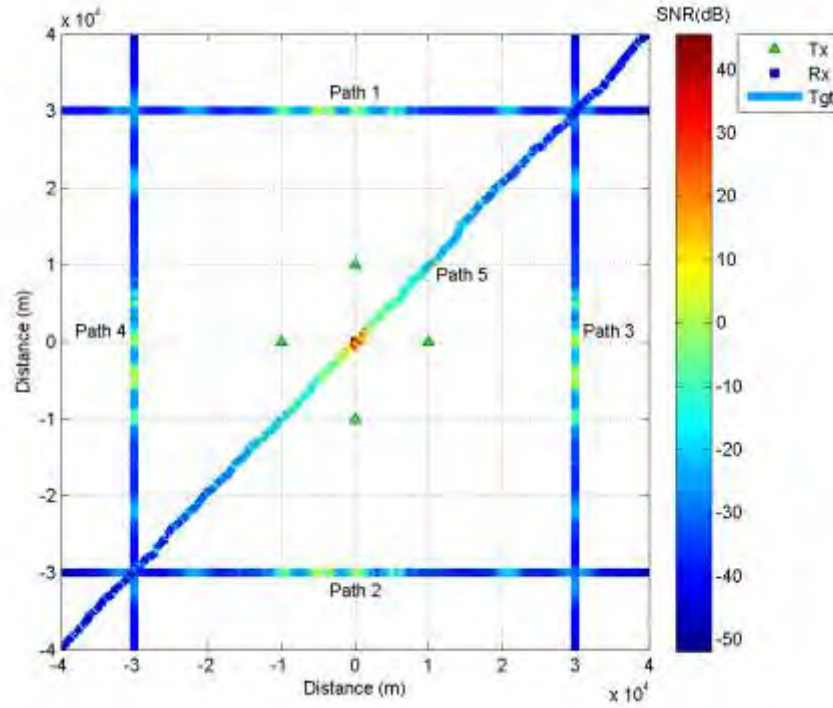


Figure 115. Detection coverage along target's path (100 m resolution) at S-Band for 4 Tx. RCS extracted from pre-computed RCS table.

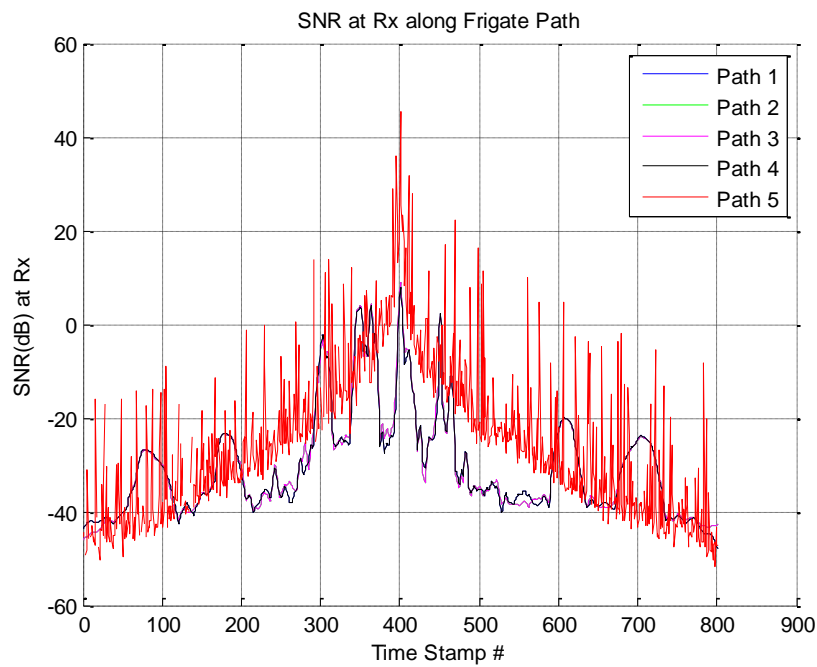


Figure 116. SNR at receiver along target's path (100 m resolution) at S-Band for 4 Tx. RCS extracted from pre-computed RCS table.

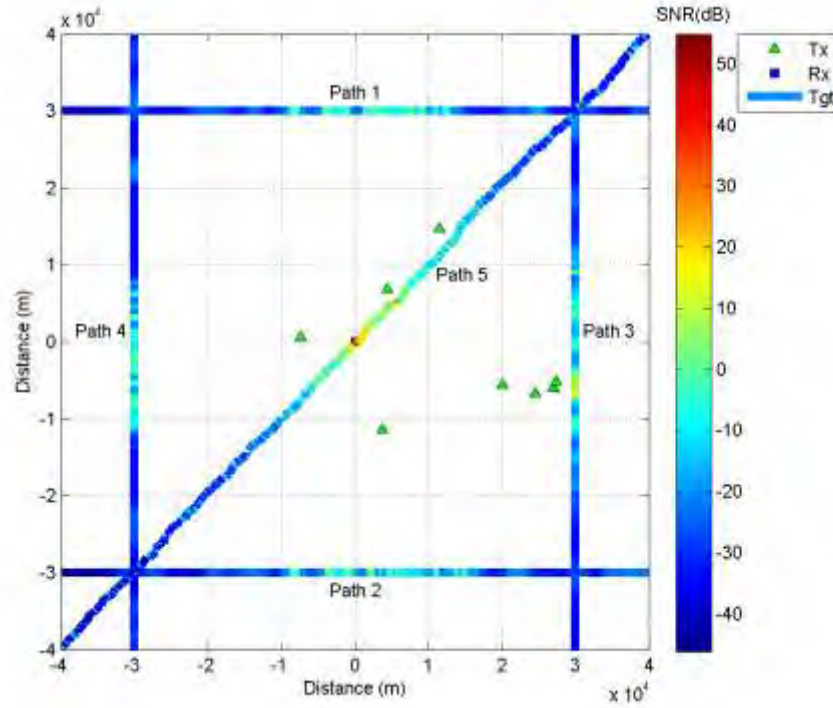


Figure 117. Detection coverage along target's path (100 m resolution) at S-Band for 8 Tx randomly position. RCS extracted from pre-computed RCS table.

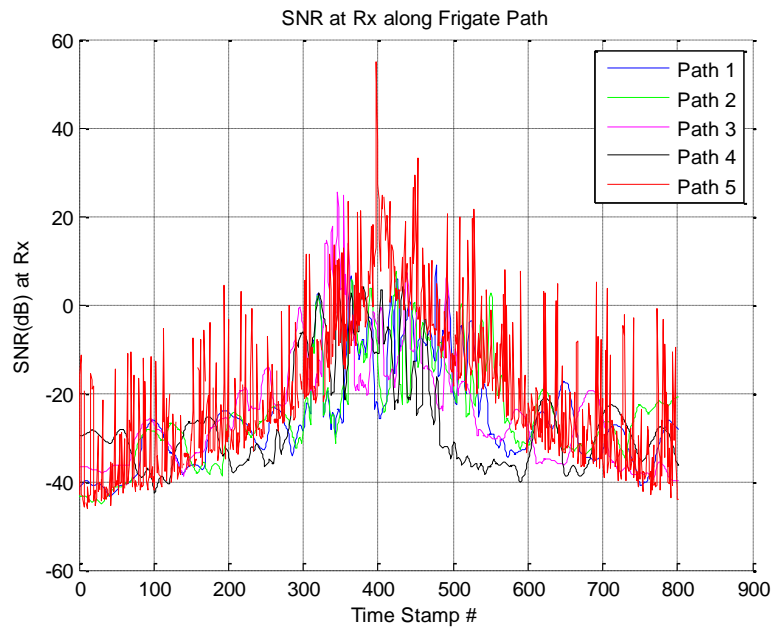


Figure 118. SNR at receiver along target's path (100 m resolution) at S-Band for 8 Tx randomly position. RCS extracted from pre-computed RCS table.

THIS PAGE INTENTIONALLY LEFT BLANK



## APPENDIX H. TARGET LOCATION RESULTS

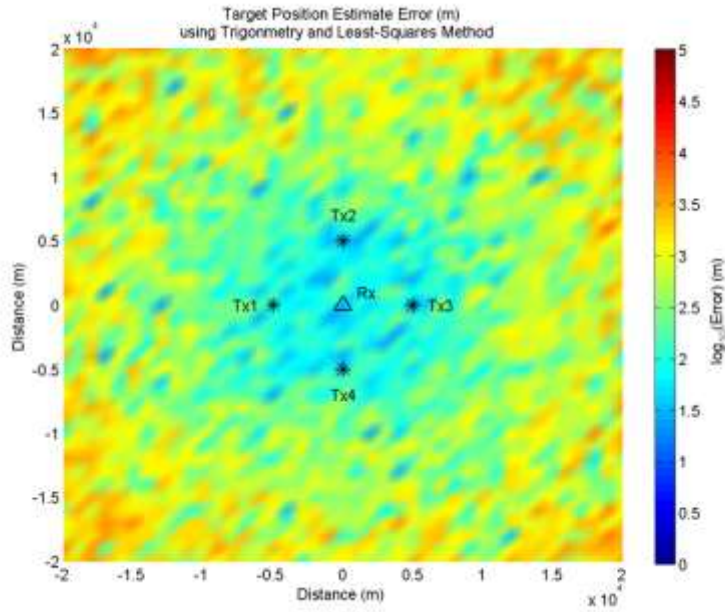


Figure 119. Target location errors using elliptical method (S-Band, 4 Tx at 5 km range) and SNR-independent measurement errors.

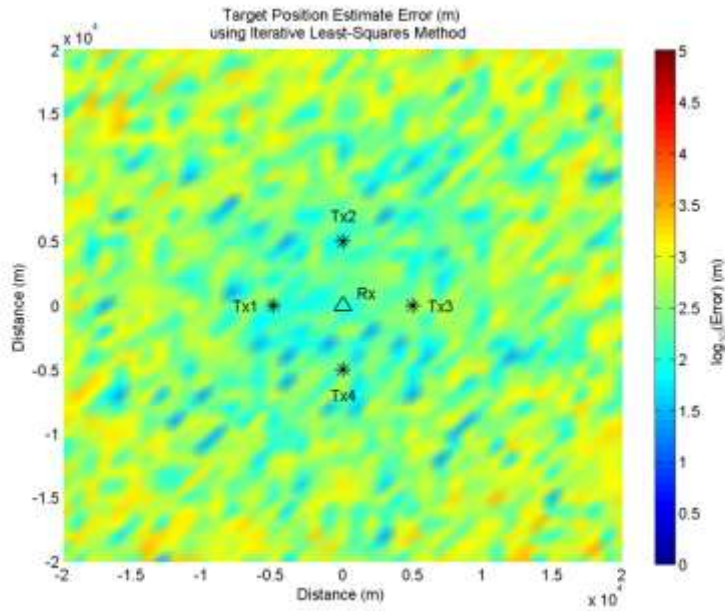


Figure 120. Target location errors using hyperbolic method (S-Band, 4 Tx at 5 km range) and SNR-independent measurement errors.

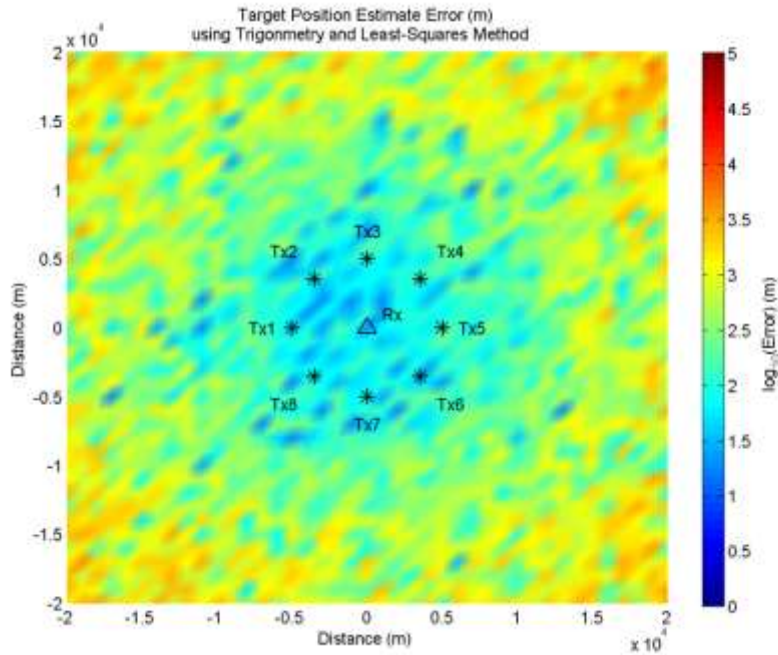


Figure 121. Target location errors using elliptical method (S-Band, 8 Tx at 5 km range) and SNR-independent measurement errors.

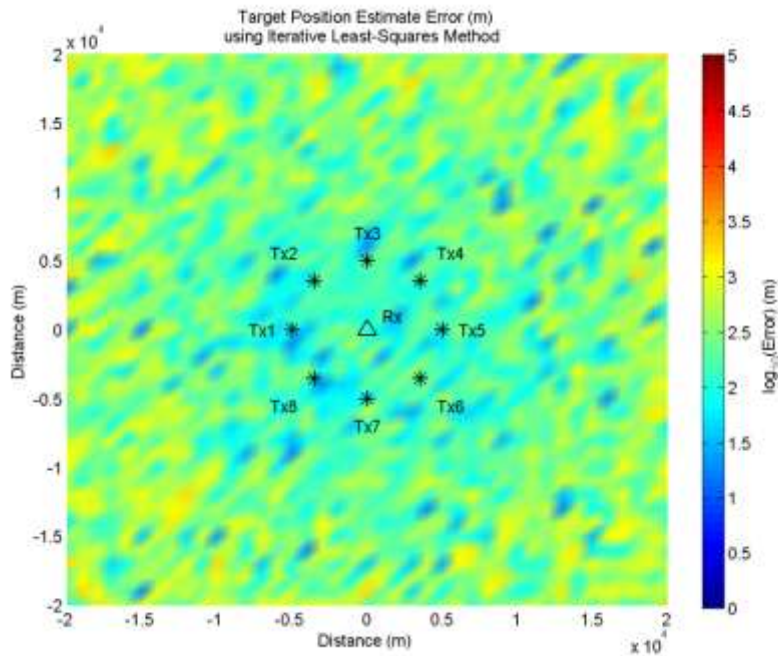


Figure 122. Target location errors using hyperbolic method (S-Band, 8 Tx at 5 km range) and SNR-independent measurement errors.



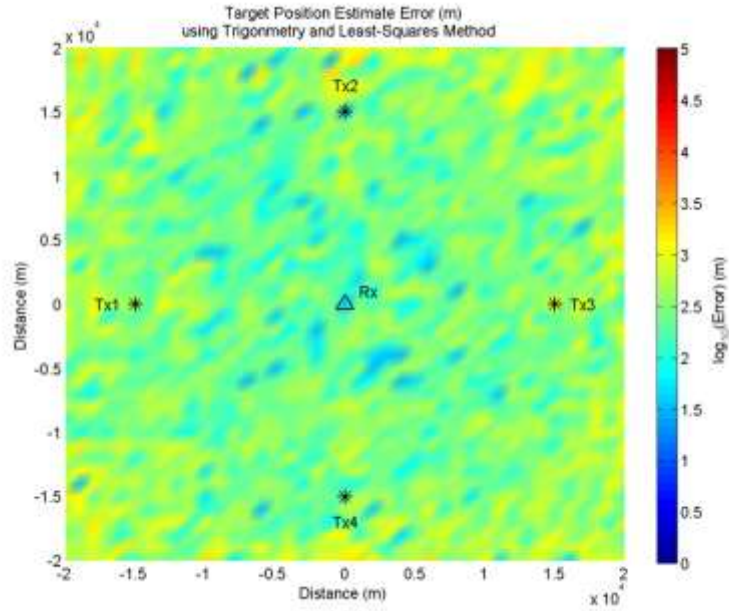


Figure 123. Target location errors using elliptical method (S-Band, 4 Tx at 15 km range) and SNR-independent measurement errors.

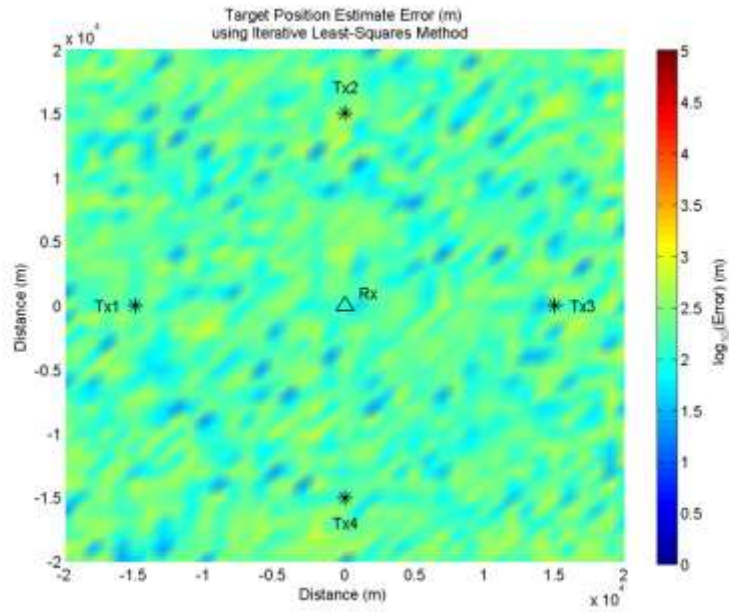


Figure 124. Target location errors using hyperbolic method (S-Band, 4 Tx at 15 km range) and SNR-independent measurement errors.

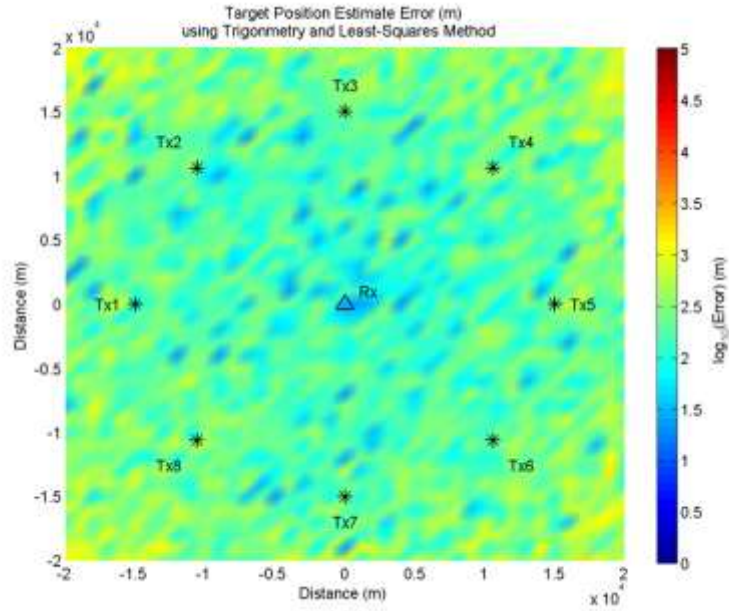


Figure 125. Target location errors using elliptical method (S-Band, 8 Tx at 15 km range) and SNR-independent measurement errors.

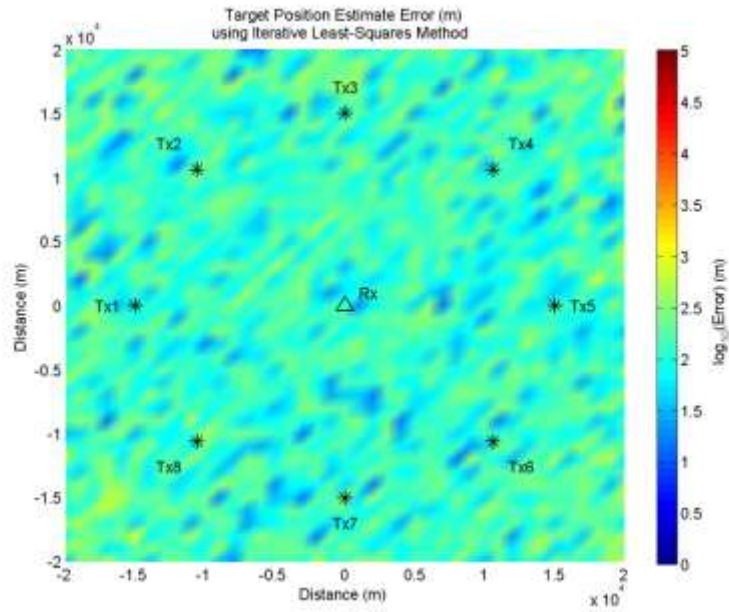


Figure 126. Target location errors using hyperbolic method (S-Band, 8 Tx at 15 km range) and SNR-independent measurement errors.

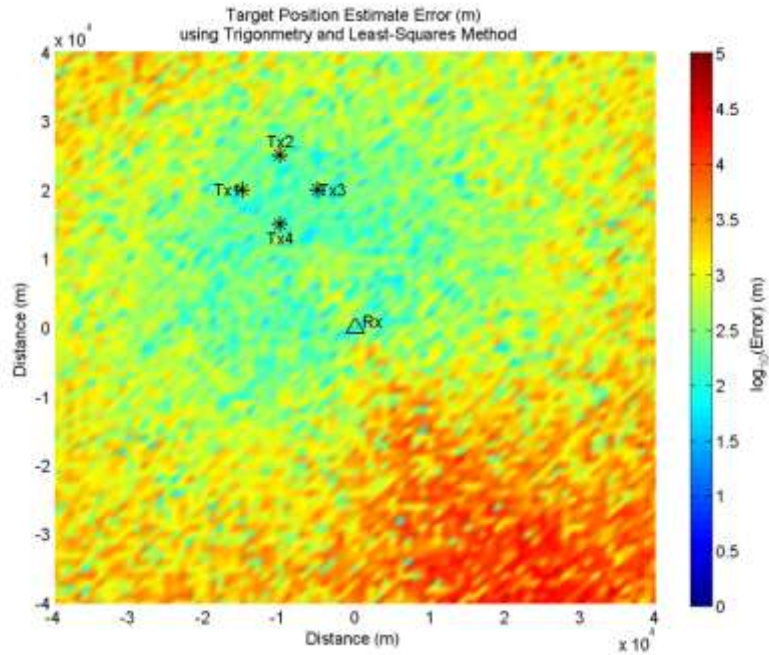


Figure 127. Target location errors using elliptical method (S-Band, 4 Tx clustered) and SNR-independent measurement errors.

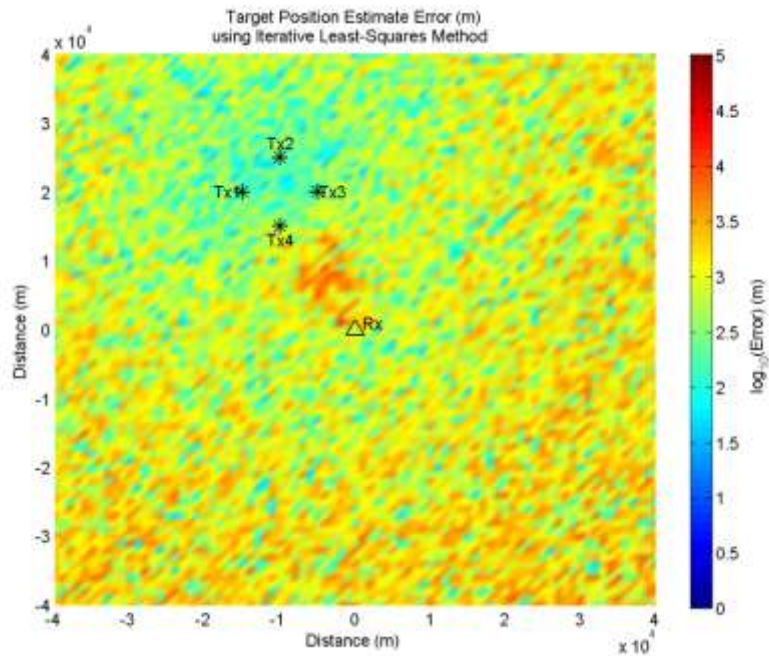


Figure 128. Target location errors using hyperbolic method (S-Band, 4 Tx clustered) and SNR-independent measurement errors.



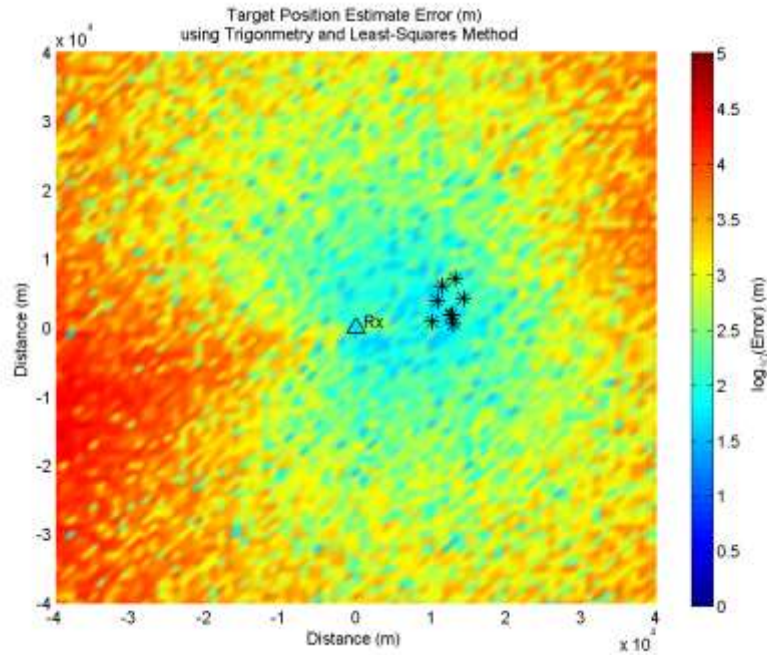


Figure 129. Target location errors using elliptical method (S-Band, 8 Tx clustered) and SNR-independent measurement errors.

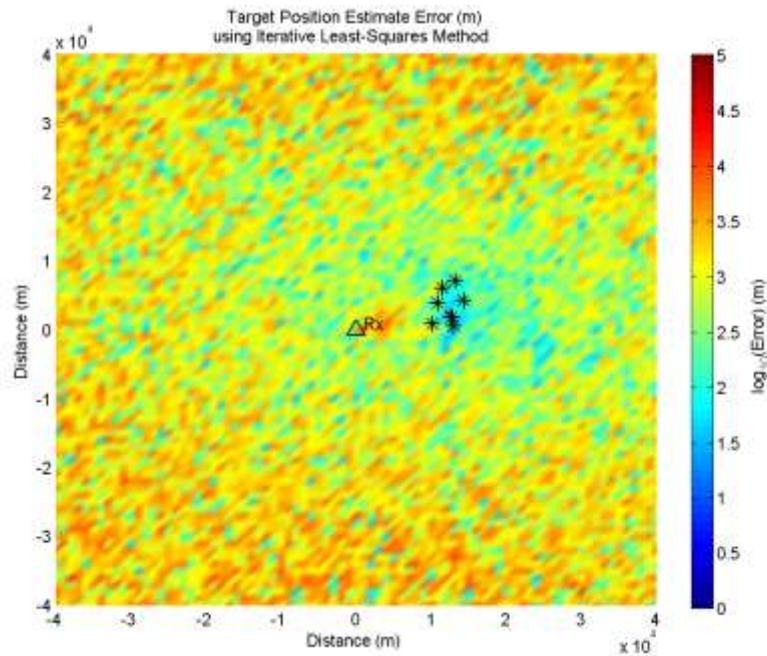


Figure 130. Target location errors using hyperbolic method (S-Band, 8 Tx clustered) and SNR-independent measurement errors.

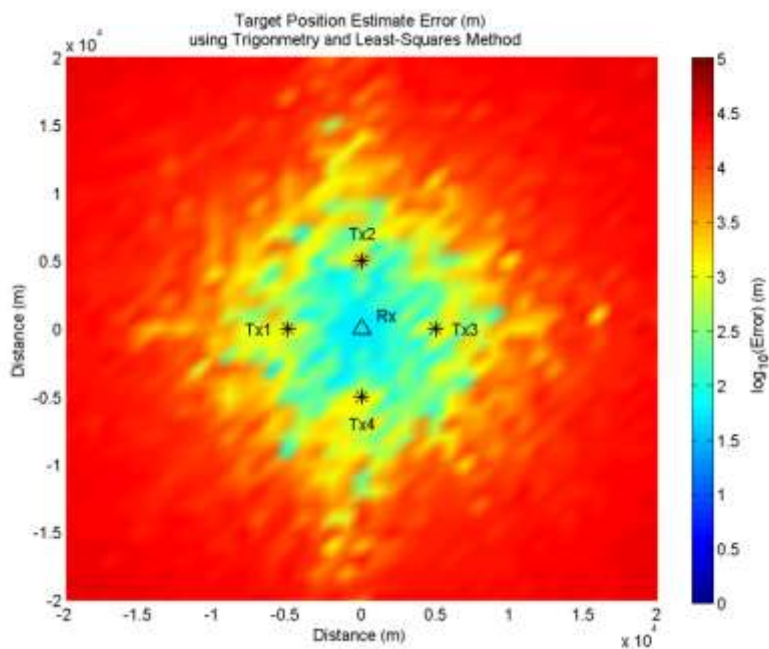


Figure 131. Target location errors using elliptical method (S-Band, 4 Tx at 5 km range) and SNR-dependent measurement errors.

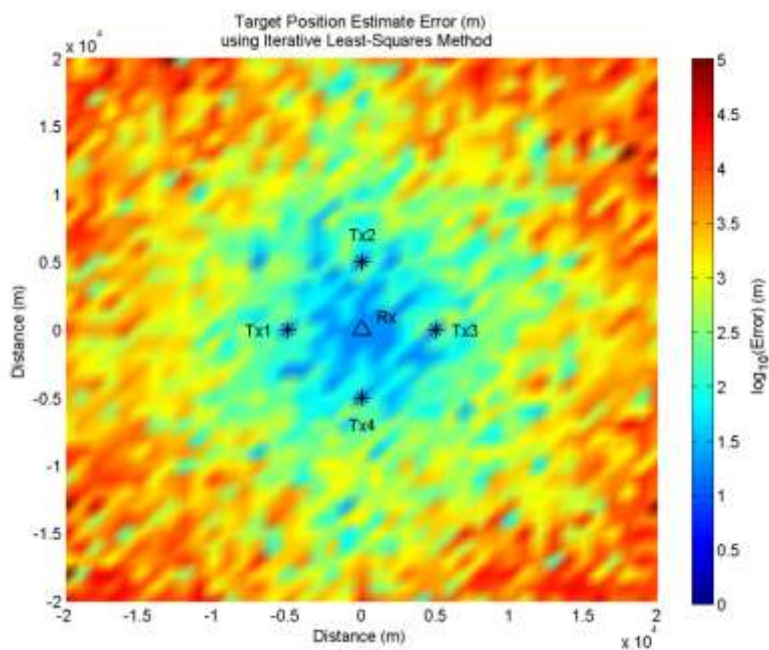


Figure 132. Target location errors using hyperbolic method (S-Band, 4 Tx at 5 km range) and SNR-dependent measurement errors.

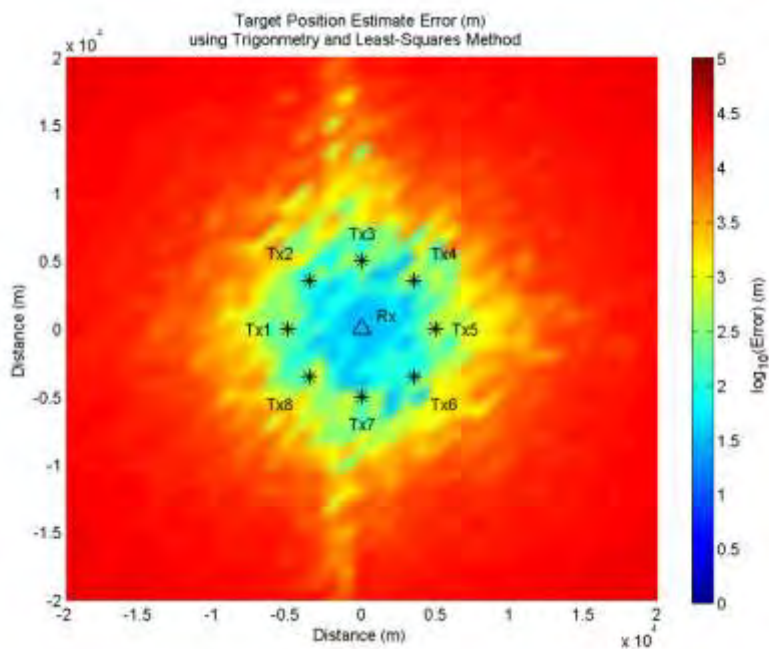


Figure 133. Target location errors using elliptical method (S-Band, 8 Tx at 5 km range) and SNR-dependent measurement errors.

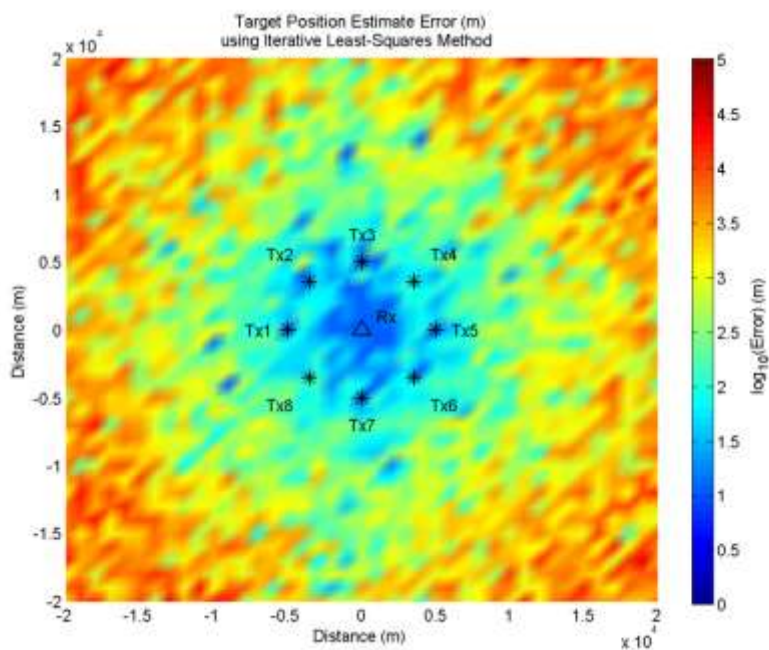


Figure 134. Target location errors using hyperbolic method (S-Band, 8 Tx at 5 km range) and SNR-dependent measurement errors.

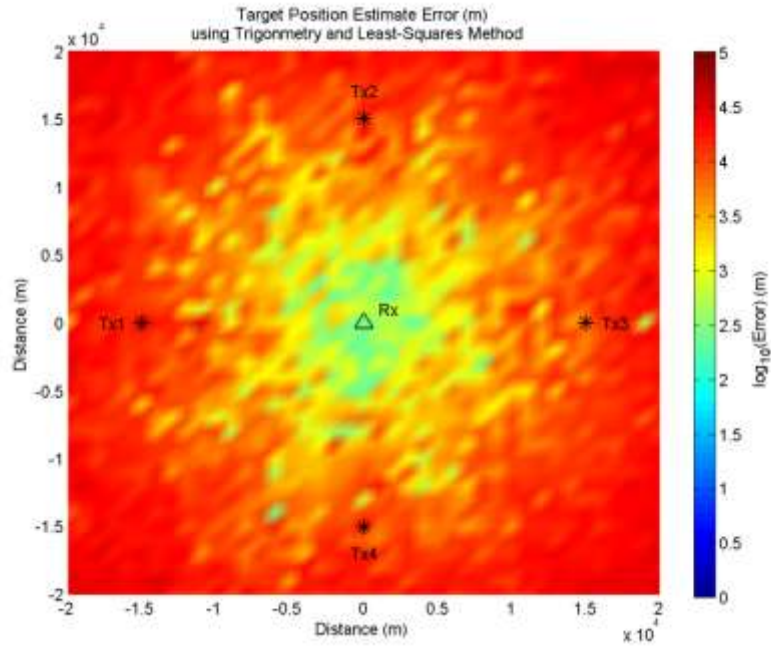


Figure 135. Target location errors using elliptical method (S-Band, 4 Tx at 15 km range) and SNR-dependent measurement errors.

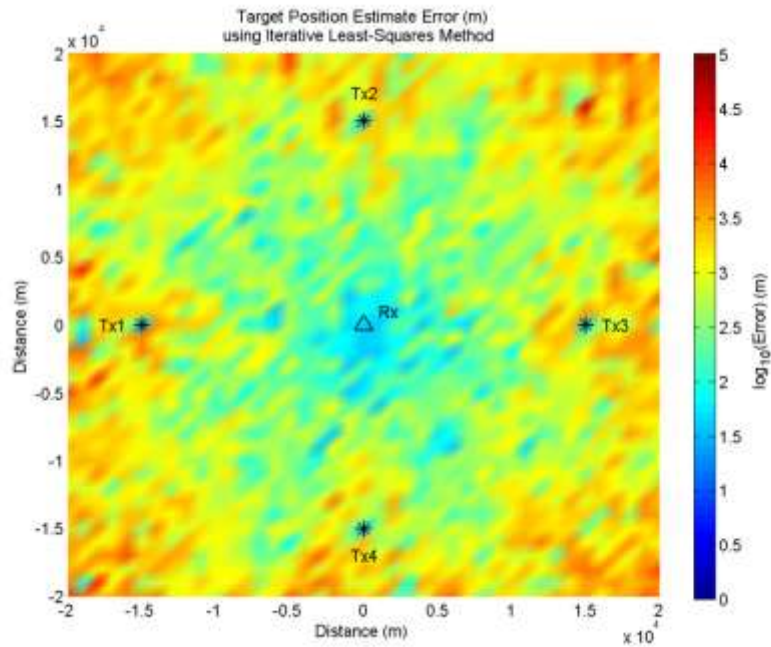


Figure 136. Target location errors using hyperbolic method (S-Band, 4 Tx at 15 km range) and SNR-dependent measurement errors.



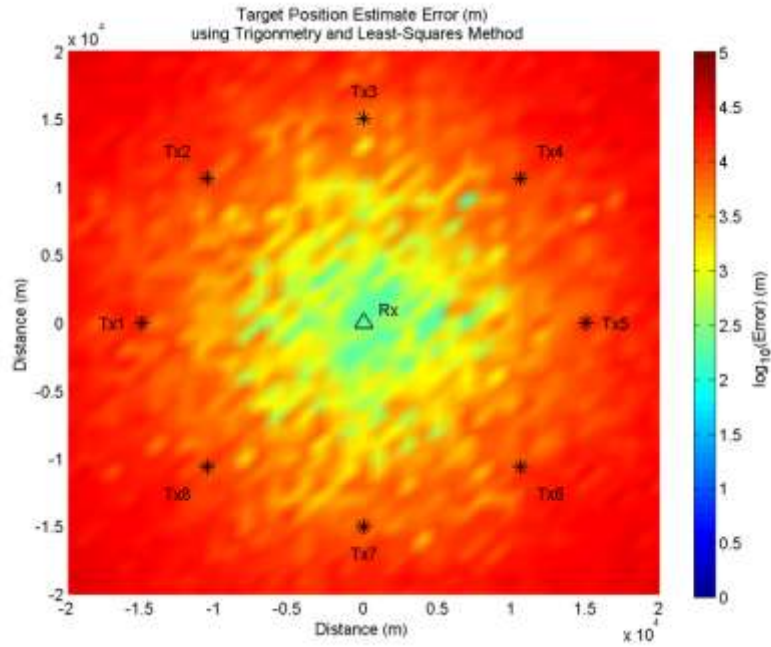


Figure 137. Target location errors using elliptical method (S-Band, 8 Tx at 15 km range) and SNR-dependent measurement errors.

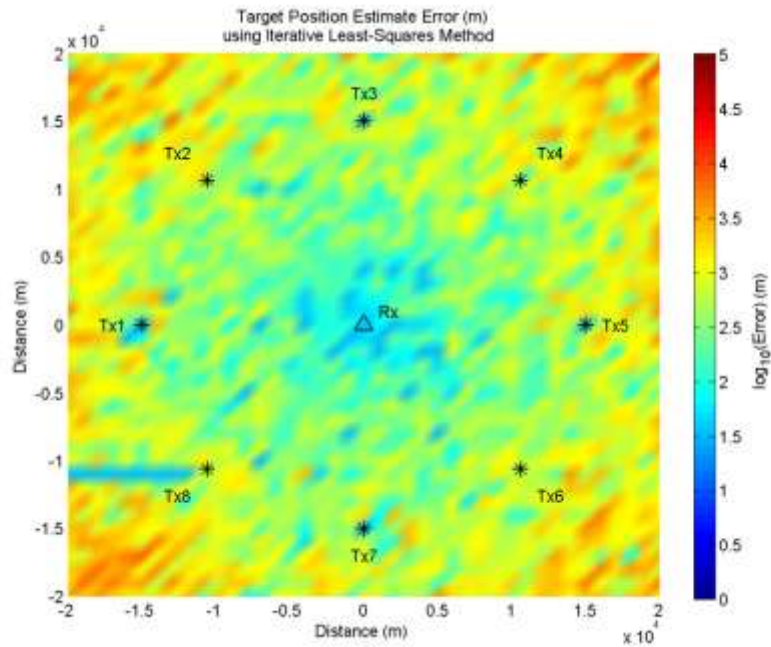


Figure 138. Target location errors using hyperbolic method (S-Band, 8 Tx at 15 km range) and SNR-dependent measurement errors.



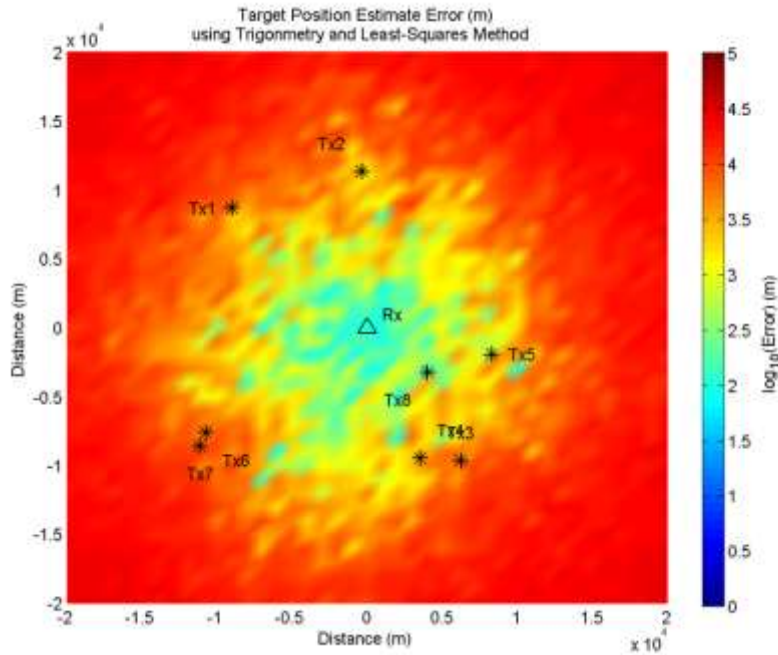


Figure 139. Target location errors using elliptical method (S-Band, 8 Tx at random positions) and SNR-dependent measurement errors.

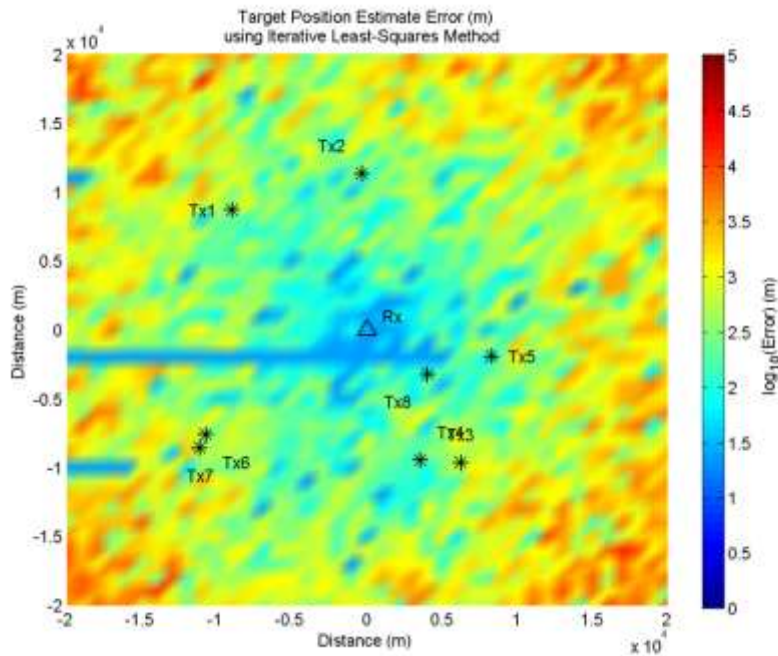


Figure 140. Target location errors using hyperbolic method (S-Band, 8 Tx at random positions) and SNR-dependent measurement errors.

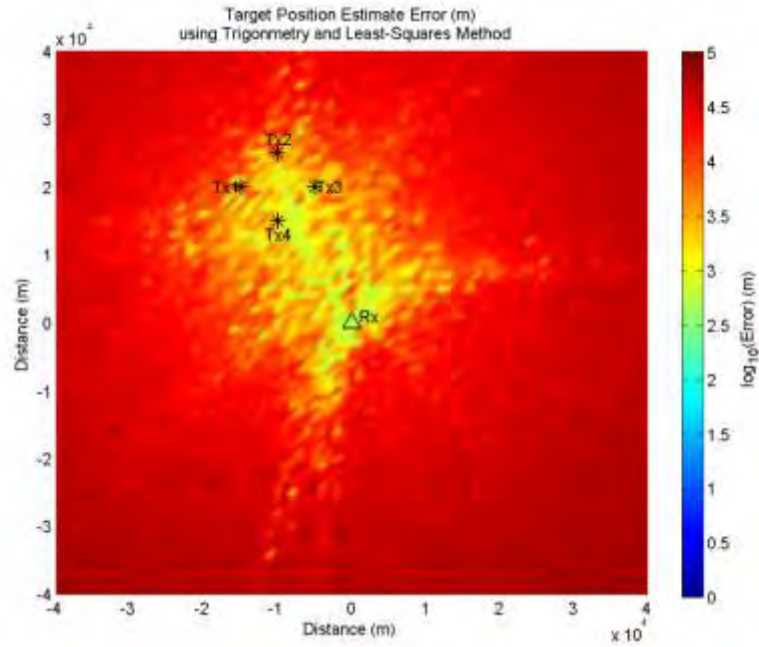


Figure 141. Target location errors using elliptical method (S-Band, 4 Tx clustered) and SNR-dependent measurement errors.

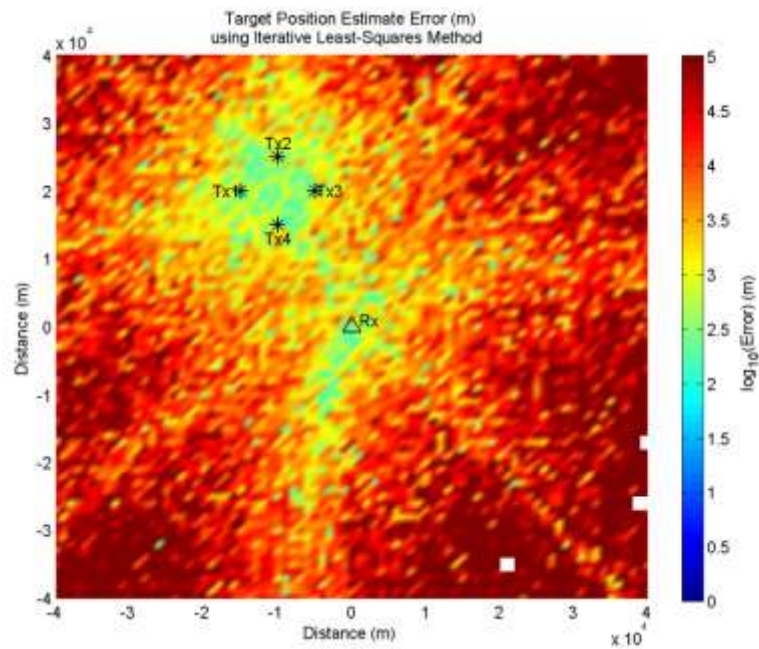


Figure 142. Target location errors using hyperbolic method (S-Band, 4 Tx clustered) and SNR-dependent measurement errors.

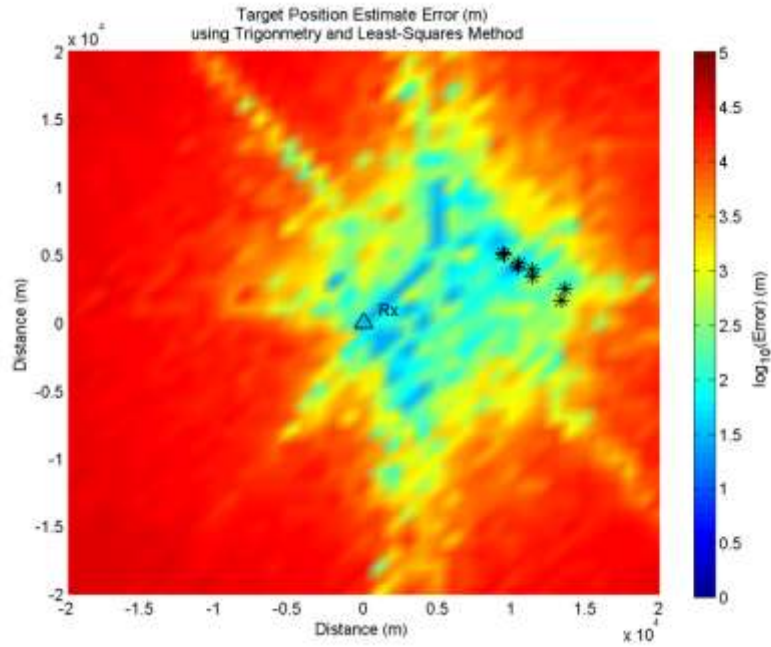


Figure 143. Target location errors using elliptical method (S-Band, 8 Tx clustered) and SNR-dependent measurement errors.

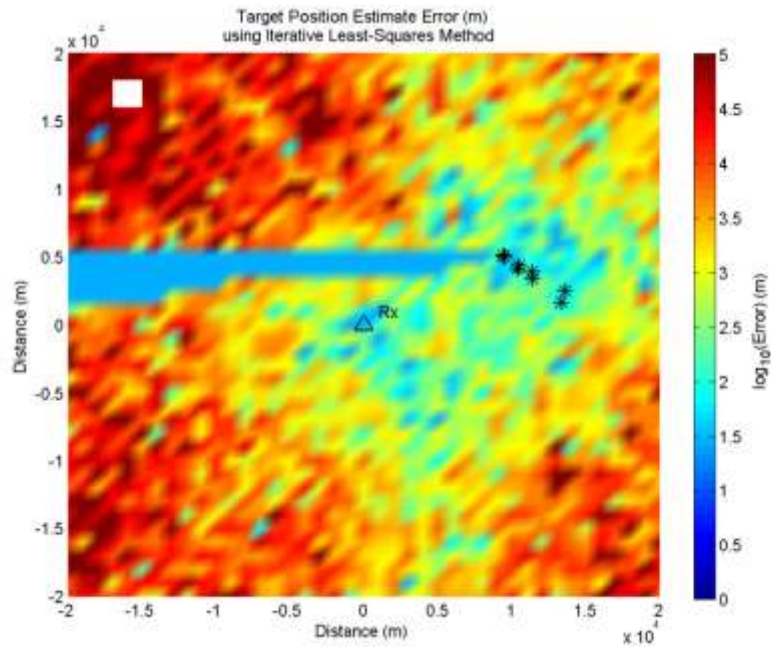


Figure 144. Target location errors using hyperbolic method (S-Band, 8 Tx clustered) and SNR-dependent measurement errors.

THIS PAGE INTENTIONALLY LEFT BLANK

## LIST OF REFERENCES

- [1] V. S. Chernyak, *Fundamentals of Multisite Radar Systems: Multistatic Radars and Multiradar Systems*. Amsterdam, The Netherlands: Gordon and Breach Science, 2015.
- [2] N. J. Willis, *Bistatic Radar*. Raleigh, NC: SciTech Publishing, 2005.
- [3] A. D. Lazarov and T. P. Kostadinov, *Bistatic SAR/ISAR/FSR: Theory Algorithms and Program Implementation*. Hoboken, NJ: John Wiley & Sons, 2014.
- [4] C. S. Sing, "Passive multistatic detection of maritime targets using opportunistic radars," M.S. thesis, Naval Postgraduate School, Monterey, CA, 2014.
- [5] N. J. Willis and H. D. Griffiths, *Advances in Bistatic Radar*. Raleigh, NC: SciTech Publishing, 2007.
- [6] J. I. Glaser, "Fifty years of bistatic and multistatic radar," *Commun., Radar and Signal Process., IEE Proc. F*, vol. 133, pp. 596–603, 1986.
- [7] M. I. Skolnik, "Fifty years of radar," *Proc. of the IEEE*, vol. 73, pp. 182–197, 1985.
- [8] P. M. Woodward, *Probability and Information Theory: With Applications to Radar*. New York: McGraw-Hill, 1953.
- [9] J. Marcum, "A statistical theory of target detection by pulsed radar," *IRE Trans. on Inform. Theory*, vol. 6, pp. 59–267, 1960.
- [10] K. M. Siegel, "Bistatic radars and forward scattering," in *Proc. Nat. Conf. Aeronautical Electron.*, 1958, pp. 286–290.
- [11] H. D. Griffiths and N. R. W. Long, "Television-based bistatic radar," *Commun., Radar and Signal Process., IEE Proc. F*, vol. 133, pp. 649–57, 1986.
- [12] P. E. Howland et al., "FM radio based bistatic radar," *Radar, Sonar and Navigation, IEE Proc.*, vol. 152, pp. 107–115, 2005.
- [13] F. Colone et al., "Multifrequency integration in FM radio-based passive bistatic radar. Part I: Target detection," *Aerospace and Electron. Syst. Mag., IEEE*, vol. 28, pp. 28–39, 2013.
- [14] F. Colone et al., "Multifrequency integration in FM radio-based passive bistatic radar. Part II: Direction of arrival estimation," *Aerospace and Electron. Syst. Mag., IEEE*, vol. 28, pp. 40–47, 2013.

- [15] D. Poullin and M. Flecheux, "Recent progress in passive coherent location (PCL) concepts and technique in France using DAB or FM broadcasters," in *Proc. of the IEEE Radar Conf. 2008 (RADAR '08)*, 2008, pp. 1–5.
- [16] A. Capria et al., "DVB-T passive radar for vehicles detection in urban environment," in *Proc. of the 2010 IEEE Int. Geosci. and Remote Sensing Symp. (IGARSS)*, 2010, pp. 3917–3920.
- [17] J. E. Palmer et al., "DVB-T passive radar signal processing," *IEEE Trans. on Signal Process.*, vol. 61, pp. 2116–2126, 2013.
- [18] C. Coleman and H. Yardley, "Passive bistatic radar based on target illuminations by digital audio broadcasting," *Radar, Sonar & Navigation, IET*, vol. 2, pp. 366–375, 2008.
- [19] Huaiying Tan et al., "PCL system with illuminator of opportunity," in *Int. Conf. on Radar 2006 (CIE '06)*, 2006, pp. 1–3.
- [20] Zhixin Zhao et al., "An experimental study of HF passive bistatic radar via hybrid sky-surface wave mode," *IEEE Trans. on Antennas and Propagation*, vol. 61, pp. 415–424, 2013.
- [21] J. M. Thomas et al., "Ambiguity function analysis of digital radio mondiale signals for hf passive bistatic radar," *Electron. Lett.*, vol. 42, pp. 1482–1483, 2006.
- [22] W. C. Barott and B. Butka, "A passive bistatic radar for detection of aircraft using spaceborne transmitters," in *Proc. of the 30th IEEE/AIAA Digital Avionics Syst. Conf. (DASC)*, 2011, pp. 1A2-1–1A2-11.
- [23] H. D. Griffiths and C. J. Baker, "Passive coherent location radar systems. Part 1: Performance prediction," *Radar, Sonar and Navigation, IEE Proc.*, vol. 152, pp. 153–159, 2005.
- [24] C. Kabakchiev et al., "Forward scatter radar detection and estimation of marine targets," in *Proc. of the 13th Int. Radar Symposium (IRS)*, 2012, pp. 533–538.
- [25] O. Overrein et al., "ISAR processing results from forward scatter radar measurements of ships," in *Proc. of the IEEE Conf. on Radar*, 2006, pp. 560–564.
- [26] M. Cherniakov et al., "Ultra wideband forward scattering radar: Concept and prospective," in *Proc. of the IET Int. Conf. on Radar Syst.*, 2007, pp. 1–5.
- [27] L. Daniel et al., "Maritime UWB forward scattering radar network: Initial study," in *Proc. of the Int. Conf. on Radar*, 2008, pp. 658–663.

- [28] H. Godrich et al., "Target localization techniques and tools for MIMO radar," in *Proc. of the IEEE Radar Conf. 2008 (RADAR '08)*. 2008, pp. 1–6.
- [29] F. C. Robey et al., "MIMO radar theory and experimental results," in *38th Asilomar Conf. on Signals, Syst. and Comput.*, 2004, vol. 1, pp. 300–304.
- [30] AIS transponders. (2015). International Maritime Organization (IMO). [Online]. Available: <http://www.imo.org/OurWork/Safety/Navigation/Pages/AIS.aspx>
- [31] "IEEE standard definitions of terms for antennas," *IEEE Std 145–1993*, pp. 1–32, 1993.
- [32] J. Traa. (2013). *Least-squares intersection of lines*. [Online]. Available: [http://cal.cs.illinois.edu/~johannes/research/LS\\_line\\_intersect.pdf](http://cal.cs.illinois.edu/~johannes/research/LS_line_intersect.pdf)
- [33] M. I. Skolnik, *Introduction to Radar Systems*. Boston: McGraw Hill, 2001.
- [34] M. I. Skolnik, "Theoretical accuracy of radar measurements," *IRE Trans. on Aeronautical and Navigational Electron.*, vol. ANE-7, pp. 123–129, 1960.
- [35] *USCG Differential GPS Navigation Service*. (2014, March). Navigation Center, U.S. Dept. of Homeland Security. [Online]. Available: <http://www.navcen.uscg.gov/pdf/dgps/dgpsdoc.pdf>
- [36] E. D. Kaplan and C. Hegarty, Eds. *Understanding GPS: Principles and Applications*. Boston: Artech House, c2006.
- [37] R. G. Wiley, *ELINT: The Interception and Analysis of Radar Signals*. Boston: Artech House, 2006.
- [38] Q. J. O. Tan, "Efficient GPS positioning algorithms to mitigate inaccuracy arising from residual errors," B.Eng. thesis, National University of Singapore, 2010.
- [39] *Formidable Class Frigate, Singapore*. (n.d.). naval-technology.com. [Online]. Available: <http://www.naval-technology.com/projects/formidable/formidable1.html>
- [40] Y. Teng. "Fundamental aspects of netted radar performance," M.S. thesis, Dept. Electron. and Elect. Eng., Univ. Coll. London, 2010.
- [41] F. C. Robey et al., "MIMO radar theory and experimental results," in *Proc. of the 38th Asilomar Conf. on Signals, Syst. and Comput.*, 2004, vol. 1, pp. 300–304.
- [42] B. K. Habtemariam et al., "Multitarget track before detect with MIMO radars," in *Proc. of the 2010 IEEE Aerospace Conf.*, 2010, pp. 1–9.

- [43] MantaDigital™ radar systems datasheet. (2014). Kelvin Hughes Marine Systems. [Online]. Available: <http://www.kelvinhughes.com/upload/pdf/brochures/radars.pdf>
- [44] Teledyne Defence QR026 EW Receiver specifications. (2011, Apr.). Teledyne Defence. [Online]. Available: <http://www.teledynemicrowave.com/images/tmsdefensepdf/QR026.pdf>
- [45] Poynting Defence DF-A0062 DF Receiver specifications. Poynting Antennas. [Online]. Available: [http://www.poyntingdefence.com/upload/brochure\\_files/20130910123219\\_DF-A0062-version-2.0.pdf](http://www.poyntingdefence.com/upload/brochure_files/20130910123219_DF-A0062-version-2.0.pdf)



## **INITIAL DISTRIBUTION LIST**

1. Defense Technical Information Center  
Ft. Belvoir, Virginia
2. Dudley Knox Library  
Naval Postgraduate School  
Monterey, California